Structural study of symmetric diblock copolymer thin films

Gadegaard, Nikolaj Hølledig

Publication date:
2000

Document Version
Publisher's PDF, also known as Version of record

Risø–R–1087(EN)

Structural Study of Symmetric Diblock Copolymer Thin Films

Nikolaj Gadegaard

Risø National Laboratory, Roskilde, Denmark
August 2000

Abstract Thin diblock copolymer film have been investigated by x-ray and neutron reflectivity as well as small angle x-ray and neutron scattering. Two model systems have been investigated. PS-PDMS (25 kg/mol-25 kg/mol), which has a glass transition temperature of ca. 100°Cfor the PS-block. This means that the structure can be frozen below that temperature, thus the development of the lamella structure may be follow by reflectivity. It was, however, not possible to reach the expected equilibrium structure. Hence the second model system, deuterateted PEP-PDMS (4.4 kg/mol-4.4 kg/mol) was chosen for its low glass transition temperature -56°C. This means that the system spontaneously should form lammela ordered structures at room temperature. This ordering was studied by neutron reflectivity and small angle neutron scattering in the temperature range from -140°C(below PDMS' glass transition temperature, -127°C) and up to 250°C(above the order-disorder temperature, 165°C). Results were found to be in perfect agreement with theory. Surface morphology as function of temperature was also measured, and holes in the surface resembled the periodicity measured by reflectivity.

This Report was submitted for the acceptance of the Master's degree at University of Copenhagen.

ISBN 87–550–2478–5
ISBN 87–550–2479–3 (internet)
ISSN 0106–2840

Information Service Department · Risø · 2000

Contents

Chapter 1

Introduction

In this project, an attempt was made to measure the structural dynamics in a symmetric diblock copolymer thin film using complementary x-ray and neutron reflectivity. The reflectivity technique allows for a compositional profiling of the thin film. In a range of experiments, it was intended to observe the development from a disordered to an ordered structure in the confined geometry. As a model system, PS-PDMS (*poly*styrene-*poly*dimethylsiloxane) was chosen for several reasons:

- Researchers at Risø had already done a substantial work on this model system, which meant that a lot of local knowledge was available.
- A number of different molecular weights were at hand, allowing for a molecular weight dependency investigation of the dynamics in the system.
- At room temperature the PS-block is in the glass state, hence it should be possible to "freeze" the structure at ambient conditions. This is important because a single reflectivity measurement may take up to 8 hours and the dynamics in the system could be faster than that.

The polymer was dissolved in chloroform in concentrations of 10 and 100 mg/ml. The thin films were spin casted on cleaned silicon substrates. The spin casting method provides highly uniform films. A number of x-ray reflectivity measurements were performed on the samples with different thicknesses. Unfortunately the system simply had insufficient x-ray contrast between the two blocks to resolve the expected layered lamellar structure. Small angle neutron scattering (SANS) experiments revealed a three dimensional structure, which was not in thermodynamical equilibrium despite annealing for several days at 150°C.

To continue the project, another model system was introduced; PEP-PDMS (*poly*ethylenepropylene-*poly*dimethylsiloxane) with a molecular weight of 4.4 kg/mol of each block [1]. This model system had in a previous study [1] shown suitable x-ray contrast. The neutron contrast was enhanced by deuterating the PEP-block. X-ray reflectivity measurements were performed on the films to ascertain their orientational ordering. Unfortunately, the contrast between the blocks was much lower than that between the blocks and the substrate, making it difficult to measure the expected lamellar ordering in thin films (700-800Å). Thicker films (ca. 4000Å) showed the expected ordering but the many layers in the film (ca. 28) made it virtually impossible to model the compositional profile in the film. Exploiting the high neutron contrast, a number of neutron reflectivity experiments were performed on the thinner films. The results revealed the expected perfect ordering of the lamella and showed a good consistency with bulk measurements.

To perform the structural dynamics experiments, the sample was brought into the disordered state above $T_{ODT} = 165$°C (order-disorder transition temperature) and then back into the ordered state. The compositional profile was measured by neutron reflectivity. It quickly became apparent that the system had ordered much faster than the acquisition time for the neutron experiment.

In the hope of "trapping" the system in the intermediate state between the completely ordered and disordered state, the system was again brought into the disordered state and then quenched to -100°C within 5 min. The first and third order Bragg peaks were measured without background (reducing the

acquisition time) to determine the degree of ordering in the film at increasing temperatures as the sample heated up from −100°C. Unfortunately, the system was ordered even immediately after quenching.

The temperature dependency of the lamellar period and the degree of ordering was measured (from -100°C to 200°C) in a combination of neutron reflectivity and small angle neutron scattering and compared to the corresponding bulk values. The data fitted the scaling theory as well as the analytical expressions given for symmetric diblock copolymer melts.

The surface topography was investigated by AFM (atomic force microscopy) and a large difference in ordering and smoothness was found between the PS-PDMS and the PEP-PDMS model systems. The PS-PDMS model system showed a partially disordered surface with a high surface corrugation. In contrast, the PEP-PDMS model system revealed a smooth surface but with partially penetrating holes. In the holes discrete steps were observed with a periodicity comparable to what was measured by neutron reflectivity and SANS.

A heat stage for the AFM was designed with the aim of measuring the repeat distance by a scanning probe method and compare this to the neutron scattering data. As the temperature limit for the microscope was 120°C, another polymer was chosen with a lower order-disorder transition temperature. The choice fell on PS-PB (*poly*styrene-*poly*butadiene), with a measured order-disorder transition temperature of T_{ODT} =71°C [2].

1.1 Common Properties of the Model Systems

The chemical structures of the investigated model systems are shown in figure 1.1.

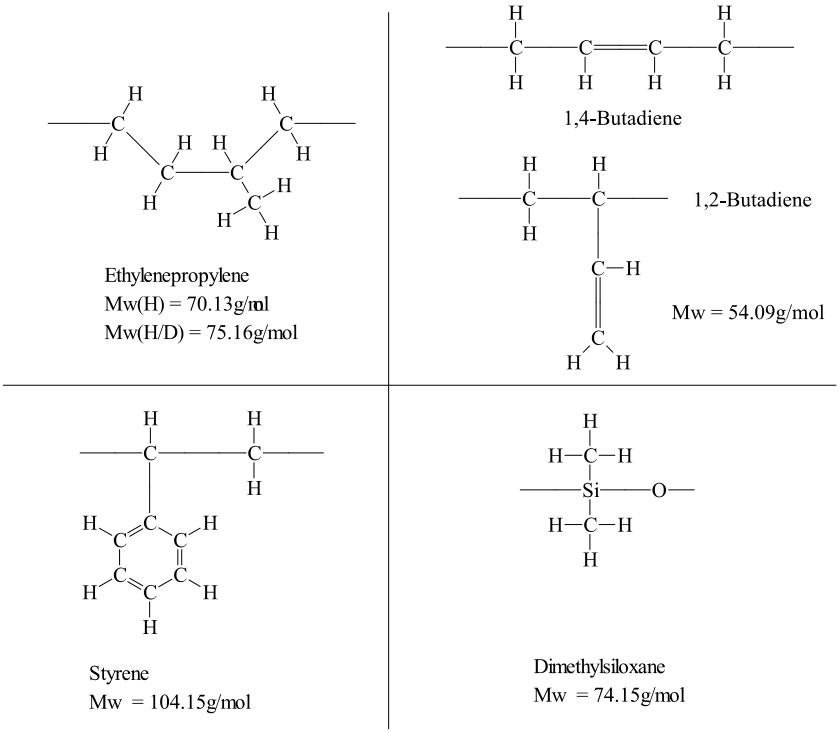

Figure 1.1: The chemical structure of the repeat units of the investigated block copolymers.

In the synthesis of PS-PB, two isomers are produced. The amount of 1,2-reacted polybutadiene is approx. 9% [2]. As was mentioned, the PEP-block in the PEP-PDMS model system is deuterated. The ratio between the amount of deuterium and hydrogen can be measured by NMR and has been found to be approx. 50% of each isotope [3].

The model systems are symmetric with respect to the molecular weight of each block and not by the number of monomeric units in each block. As can be seen in figure 1.1 the molecular weight of

the monomeric units vary between the systems. Furthermore, the number of monomeric units in the polymer is not the same as the degree of polymerization, which is considered to be the total number of *statistical segments*. The **effective** *degree of polymerization* N is defined as [1]

$$N = \frac{V}{v_0} \tag{1.1}$$

where V is the contour volume of the polymer molecule and v_0 is the volume of a standard segment unit. The definition is based on the picture of an unperturbed Gaussian conformation of the polymer chains and will be used to compare data with theory. For block copolymers the ratio between the two monomers (A and B) is calles the *volume fraction* f_A. For a symmetric block copolymer $f_A = 0.5$.

Chapter 2

Polymer Theory

Polymers are manufactured from low-molecular-weight compounds called monomers by polymerization reactions, in which large numbers of monomer molecules are linked together. Depending on the structure of the monomer or monomers and on the polymerization method employed, polymer molecules may exhibit a variety of architectures. Most common are the linear, branched, and network structures.

Polymers are often blended to modify their properties in much the same way that metals are alloyed. The blended polymers may or may not dissolve in one another; in most cases they do not. Where they are miscible, the properties of the homogeneous blend are often a weighted average of those of the individual polymers. In the case of immiscible polymer blends, a varaiety of strategies have been developed to keep the separated phase together when blends are subjected to stress. One strategy is to add block or graft copolymers formed from the monomers of the immiscible homopolymers in order to improve the adhesion at the boundaries between the polymers phases.

2.1 Characterization of Polymers

Polymers can be classified by the number of different monomer species in the molecule. Polymers consisting of only one monomer type are called *homopolymers*, whereas polymers comprised of more monomer types are called *copolymers*. The different configurations are shown in figure 2.1.

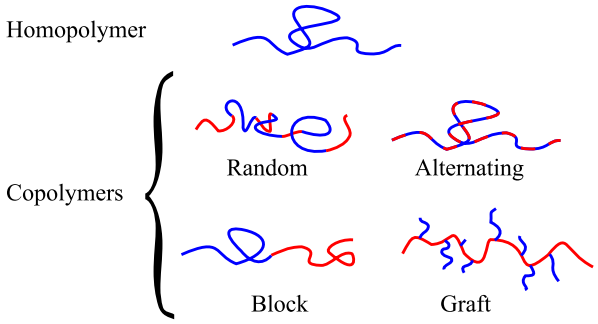

Figure 2.1: Schematic figure of a homopolymer and different (di)copolymer types.

For homopolymers, the number of monomer units forming the chain is sufficient to describe the composition. For copolymers the ratio between the number of different monomeric units and the type of sequence is also necessary to describe the structure.

Random. The sequence of monomeric units corresponds to the sequence obtained in a series of tosses of a coin. The corresponding configurations is called *random* or *statistical*.

Alternating. The preferential attachment of one monomeric unit to another influences the probability in a series of tosses of a coin. In the case of an equal number of both units the copolymer becomes

alternating.

Block. The opposite case is also possible, where attachment is preferred to the same type. In that limit the monomers will be fully separated and the result is a *block* copolymer. Block copolymers are mainly prepared by living polymerization [1, 2, 4, 5]. However, block copolymers are usually synthesized differently. Initially a homo polymer is synthesized by living anionic polymerization from one type of monomers. Growth only occurs in one direction, thus when the solution is exchanged with a second monomer a diblock copolymer is formed.

Graft. Polymers based on a homopolymer backbone with short side chains of another polymer are called *graft* copolymers. The chains are often attached more or less randomly to the backbone.

2.2 Phase Behavior

The phase behavior of homopolymers and blends was described by Flory and Huggins and is summarized in [6]. They modeled the system as a three dimensional lattice and were in this simple theory able to account for the phase behavior.

For block copolymers the phase behavior can be characterized by three parameters: the total degree of polymerization N, the overall volume fraction of the A component f_A, and the A-B segment-segment interaction (Flory-Huggins) parameter χ. During synthesis, all parameters can be controlled: the degree of polymerization and composition are controlled by the amount of initiator and monomer added, whereas the interaction parameter depends on the choice of monomeric units. The phase diagram is described by the combined parameter χN and the volume fraction of one of the components.

Block copolymers exhibit a rich phase behavior. In the ordered state, i.e. where the blocks are immiscible, they phase segregate. The major difference in phase behavior between homopolymers and

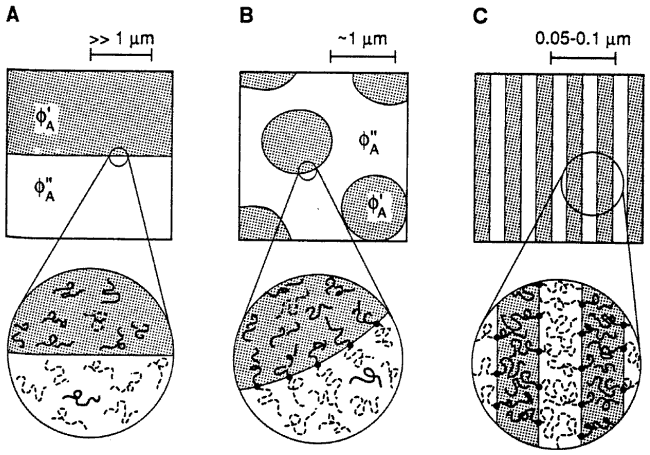

Figure 2.2: a) In a mixture of immiscible homopolymers, macrophase separation occurs. b)+c) The covalent bond in block copolymers leads to microphase separation. b) In a mixture of two homopolymers and a diblock copolymer, a surfactant stabilized phase separation can be produced [7].

block copolymers is the scale of the phase separation. The covalent bond in block copolymers restricts *macroscopic* phase separation of dissimilar blocks. This is illustrated in figure 2.2. A wide range of *microstructures* in the ordered phase has been observed. In figure 2.3 the observed structures in PS-PI (*poly*styrene-*poly*isoprene) are illustrated as a function of the volume fraction of PS.

The phase diagram for the PEP-PDMS model system used in the present study has previously been investigated [1] and is shown in figure 2.4. As can be seen from the symmetric sample ($f_{\mathrm{PEP}} = 0.5$) used in this work, the ordered phase is lamellar in the accessible temperature range. The abbreviations in the figure are:

BCC Body centered cubic arrangement of the spheres (micelles).

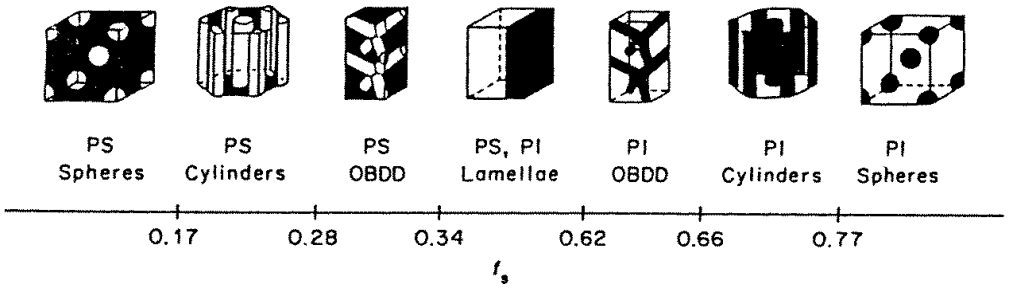

Figure 2.3: Different microstructures as a function of the volume fraction of PS. When the reference was published, it was thought that the structure between the lamella phase and the cylindrical phase was ordered bicontinous double diamond (OBDD), however the structure is now known as the *gyroid* phase. Adapted from [8].

HEX Hexagonally ordered cylinders.

G Gyroid phase (see caption in Figure 2.3).

LAM Lamella ordering.

HPL A presently unidentified structure [1].

DIS The disordered state.

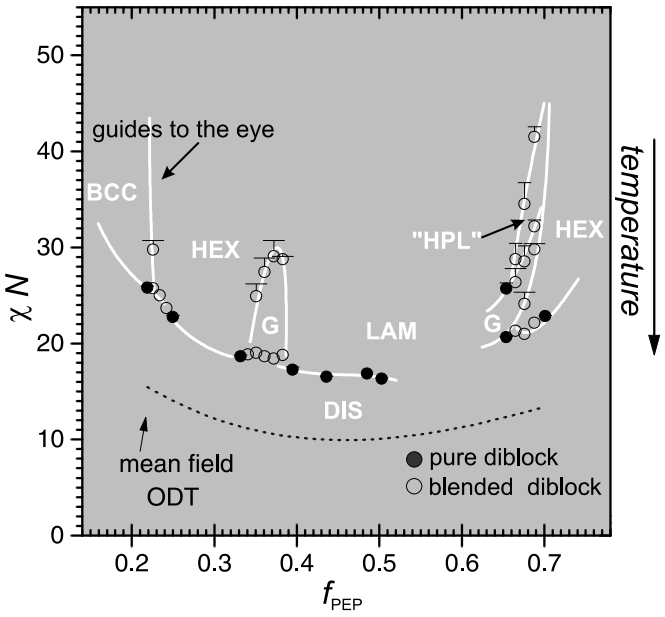

Figure 2.4: Experimentally determined phase diagram for PEP-PDMS. Adapted from [1].

2.3 Physical Properties

2.3.1 Glass Transition Temperature

Polymers exhibit two types of morphology in the solid state: amorphous and semicrystalline. In an amorphous polymer the molecules are oriented randomly and are intertwined, much like cooked spaghetti,

and the polymer has a glasslike, transparent appearance. In semicrystalline polymers, the molecules pack together in ordered regions called crystallites, as shown in figure 2.5. As might be expected, linear polymers, having a very regular structure, are more likely to be semicrystalline. Semicrystalline polymers tend to form very tough plastics because of the strong intermolecular forces associated with close chain packing in the crystallites.

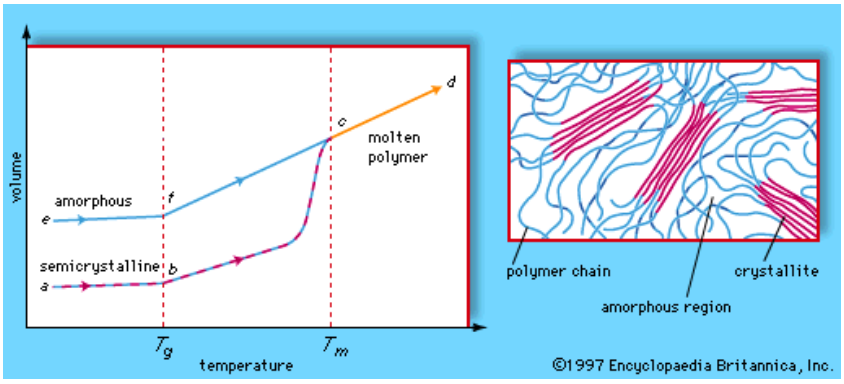

Figure 2.5: (Left) Volume-temperature diagram for amorphous and semicrystalline polymers, showing volume increasing with temperature; (right) schematic diagram of the semicrystalline morphology, showing amorphous regions and crystallites [9].

The crystallinity in polymer materials (up to 98% [10]) is not as high as for metals (disorders less than a part per million [10]). Amorphous materials do not have a specific melting point, since this is defined as the melting of the last crystal in the material. To describe their behavior another transition is introduced; the glass transition temperature T_g. It is defined as the point at which the material goes from an elastic to a viscoelastic response [11]. The glass transition temperature can be measured in a rheometer, where oscillatory shear forces can be applied and the response from the material is measured as a function of temperature.

In microphase separated diblock copolymers, two glass transitions are expected; both are close to the transition temperatures for the homopolymers. For PS an empirical equation relates T_g to the molecular weight [2]

$$T_g = 100°\mathrm{C} - \frac{10^5 \mathrm{g/mol}}{M}\ °\mathrm{C} \tag{2.1}$$

The transition temperatures for the polymers used are tabulated below.

Polymer	PDMS	PEP	PS
T_g/°C	-127	-56	96

Table 2.1: Measured glass transition temperatures for the polymers used in this thesis. The T_g of PS was calculated from the equation above with the corresponding molecular weight.

2.3.2 Solubility

Two cases of solubility of polymers will be discussed in this section: in solvents and in other polymers. The former has to be considered when preparing solutions for the spin casting procedure, and the latter dictates the phase behavior in the resulting thin film and bulk.

The thermodynamic description of the dissolution process is given, as in any chemical reaction, by the change in Gibbs free energy, ΔG

$$\Delta G = \Delta H - T\Delta S \tag{2.2}$$

and the change must be negative to dissolve the polymer spontaneously. Inspecting the right hand side, ΔS is almost always positive (going from the ordered to the disordered phase) due to the increased degree

of freedom, whereas ΔH can be positive or negative. The sign depends on the interaction between the polymer and the solvent compared to the interactions of the polymer with itself. If the self interaction is less favorable, ΔH will be negative.

The polymer-solvent interaction can be parameterized by the Flory-Huggins interaction parameter χ. The parameter consists of e nthalpic (energetic) and entropic (conformational) terms

$$\chi = \chi_H + \chi_S \tag{2.3}$$

According to [12], the entropic contribution can be taken to be constant, $\chi_S = 0.34$. The enthalpic term is related to the Hildebrand parameter δ, which describes the attractive strength between the molecules of the material.

$$\chi_H = \frac{v_0}{RT}(\delta_1 - \delta_2)^2 \tag{2.4}$$

where v_0 is the reference volume and δ_1 and δ_2 are the Hildebrand parameters for the two interacting molecules. The reference volume has been chosen to be 118.3Å^3 at 150°C [1]. The Flory-Huggins theory criterion for a polymer and solvent to be miscible is

$$\chi < 0.5 \tag{2.5}$$

In practice a solvent is chosen to have a Hildebrand parameter close to the ones for the two blocks.

Polymer	δ / (MPa)$^{1/2}$	Solvent	δ / (MPa)$^{1/2}$
PEP	15.8	Cyclohexane	16.8
PDMS	14.9-15.6	Chloroform	19.0
PS	17.4-21.1	Toluene	18.2
		Water	47.9

Table 2.2: Hildebrand parameters for different polymers and solvents. The values are taken from [12, 13].

Tables are available for the solubility of polymers in various solvents depending on concentration [12] (see table 2.2). In figure 2.6 the solubility is plotted for PS-PDMS in chloroform and cyclohexane. The

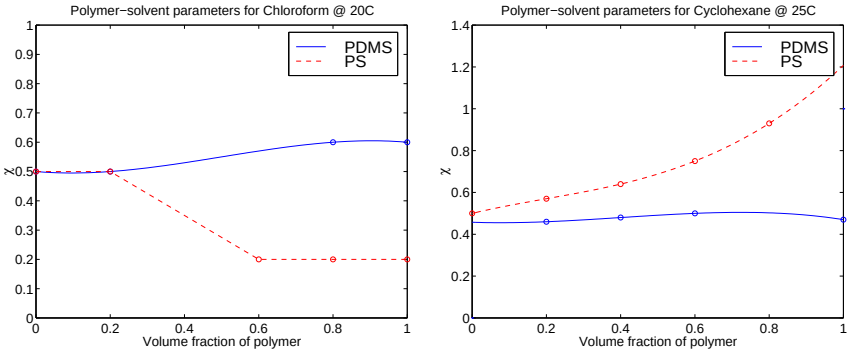

(a) F-H parameter for chloroform.

(b) F-H parameter for cyclohexane.

Figure 2.6: Flory-Huggins parameter for PS-PDMS in different solvents [12].

interaction parameter for PDMS is almost constant for both solvents, so PDMS is not favoured by either of them. PS, on the other hand, becomes better and better dissolved in chloroform as the concentration increases, whereas in cyclohexane it becomes less soluble. This might have an effect on the resulting film produced by spin casting.

Often the Flory-Huggins interaction parameter is parameterized as [1]

$$\chi = \frac{A}{T} + B \tag{2.6}$$

where A and B are empirical constants and can be found in appendix C.7.

2.3.3 Surface Energy

The sequence of the layers in lamella ordered block copolymer systems is determined by the surface and interfacial energies and by the flexibility of the polymer chains. A large difference in surface energies between the two components will cause an enrichment of the surface with the low-surface-energy component. Sikka et al. [14] showed that if the difference in surface energies is small, the more flexible component can be driven to the surface due to entropical differences between the two blocks.

2.4 Scaling Behavior of the Microdomains

Much theoretical work has been done on the ordered state, in which micro segregation in block copolymers occurs. There are two limits in the system, an ordered and a disordered state, as can be seen in figure 2.7.

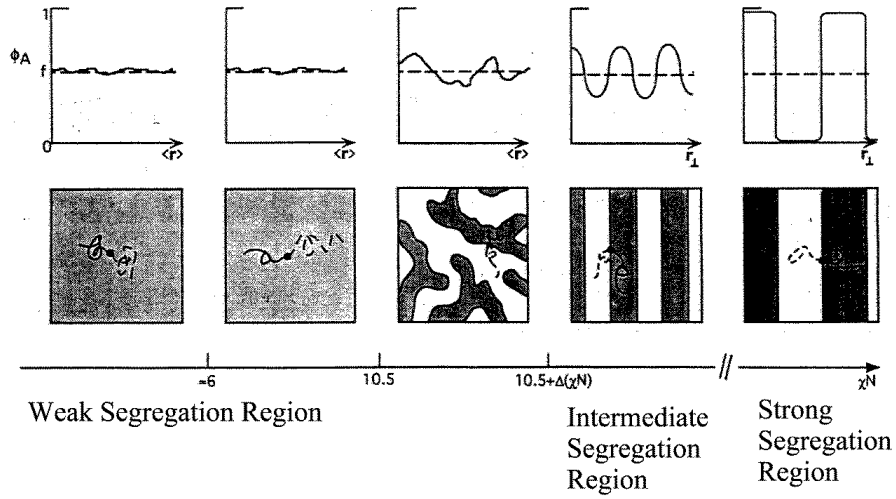

Figure 2.7: Illustration of the regimes between the weak segregation regime and the strong segregation regime limits for diblock copolymer melts. ϕ_A is the molar fraction of block A in the melt.

In the region from the order-disorder transition into the disordered (homogeneous) state, the segment-segment interactions are weak and the polymers have a Gaussian coil conformation, hence the region is called the *weak segregation region* (WSR). The ordered state is divided into two regions with different scaling exponets in the powerlaw describing the lamellar period. The region between the *strong segregation regime* (SSR) and the WSR is called the *intermediate segregation regime* (ISR). The coil conformation becomes more and more stretched in the ordered state due to repulsion between dissimilar monomers.

2.4.1 Disordered State

Leibler [15] wrote a seminal paper describing the disordered state. He was able to predict the phase diagram and that the order-dosorder phase transition for a symmetric diblock copolymer should occur at $\chi N|_{ODT} = 10.5$. Furthermore, he was able to describe the structure factor in the disordered state.

Fredrickson and Helfand [16] extended Leibler's theory to take into account the effect of a free surface, which has a preferential affinity for either the A or B block. This type of interaction was shown to induce oscillations in the composition near the surface. It has experimentally been shown [17, 18] that fluctuation concentration effects are important near the order-disorder transition. The fluctuations stabilize the disordered phase, and the order-disorder transition temperature is affected by the concentration fluctuations

$$\chi N|_{ODT} = 10.5 + 41.0\bar{N}^{-1/3} \tag{2.7}$$

where $\bar{N}$ is the Ginzburg fluctuation parameter defined as

$$\bar{N} = N\frac{a_{\mathrm{AB}}^6}{v_0^2} \tag{2.8}$$

where N is the total degree of polymerization, v_0^2 is the *standard* segment volume which at room temperature is defined as 108.4Å^3 [1], and a_{AB} is the weighted segment length of the diblock given by

$$a_{\mathrm{AB}}^2 = f_{\mathrm{A}}a_{\mathrm{A}}^2 + (1 - f_{\mathrm{A}})b_{\mathrm{B}}^2 \tag{2.9}$$

a_A and a_B are the segment lengths of the blocks A and B, respectively.

Both the segment lengths and the standard segment volume are temperature dependent, and the dependency can be found in appendix C.3. The concentration fluctuation corrected $\chi N|_{\mathrm{ODT}}$ can be calculated for the PEP-PDMS model system used in this project to be 15.57, which differs from the value predicted by Leibler. The measured transition temperature (165°C) can be compared to the transition temperature estimated from Leibler's mean field theory $\chi N|_{\mathrm{ODT}} = 10.5$ and eqn. 2.6. From that, the transition temperature can be calculated to $T|_{\mathrm{ODT}} = 558$ K = 280°C. Hence the fluctuation concentration correction in the description of the order-disorder transition is very important for low molecular weight species.

2.4.2 Ordered State

Helfand and Wasserman [19] described the strong segregation region under the assumption, that deep in the ordered state the interphases between A- and B-blocks of the lamella are assumed to be narrow compared to the repeat period of the lamella. The free energy was written as a function of lamella size and minimized to obtain predictions of the lamellar distance.

They minimized the change in Gibbs free energy with respect to the lamellar thickness D and obtained the following scaling relation

$$D \propto \chi^{1/7} \sim \chi^{0.17} \tag{2.10}$$

Semenov [20] was able to derive an analytical expression for the different structures in the strong segregation region. The lamellar thickness was predicted to be[1]

$$D = 4\left(\frac{3}{\pi^2}\right)^{1/3} \frac{a}{\sqrt{6}} N^{2/3} \chi^{1/6} \tag{2.11}$$

where a is the weighted segment length a_{AB}. Semenov [20] also derived an expression for the interphasial width λ between the two blocks [22]

$$\lambda = \frac{2a}{\sqrt{6\chi}} \tag{2.12}$$

Melenkevitz and Muthukumar [23] used a density functional theory to describe the lamellar ordering in diblock copolymers. The power laws for the two regions were found to be; $D \propto \chi^{0.22}$ and $D \propto \chi^{0.17}$ for the intermediate region $12.5 \leq \chi N \leq 95$ and the strong segregation region $95 < \chi N$, respectively. Their result in the SSR limit reduces to the result by Helfand and Wasserman [19].

Shull [24] used a mean field theory to describe the scaling behavior of bulk melts, surfaces and thin films. Introduction of two boundary conditions in the system leads to composition fluctuations. They propagate from each surface towards the center of the film. Again the overall free energy of the film dictates its structure. The free energy depends on the interaction of the composition oscillations, whether they interact constructively or destructively. As the films get thinner, the order imposed by the film surfaces becomes more dominating than the concentration fluctuations. This results in a less stable disordered phase and the transition temperature increases.

[1] In the original refence [20], Semenov defined the segment length a' from the radius of gyration $R_g = a'\sqrt{N}$. In this text, the segment length a is defined from the end-to-end distance $R_{ee} = a\sqrt{N}$, because table values [21] are listed with respect to R_{ee}. Both R_g and R_{ee} can be derived statistically [2, 11] and are related as $R_{ee}^2 = 6R_g^2$.

Chapter 3

Experimental Equipment

The neutron experiments were performed at the 10 MW heavy water moderated research reactor DR3 at Risø National Laboratory. The neutrons are moderated, ie. their kinetic energy is reduced, by D_2O to the reactor temperature, $T = 50°C$, and their energy distribution is nearly Maxwellian. There are four neutron outlets from the core: two with *thermal neutrons* and two with *cold neutrons*. Thermal neutrons have a wavelength of 1-4 Å, while the cold neutrons have reduced kinetic energy and thereby longer wavelengths of 5-20 Å. To increase the flux of cold neutrons, the thermal neutrons are cooled when passing through a chamber filled with supercritical H_2 at a pressure of 16 atmospheres and a temperature of 38 K. The low energy neutrons are essential when probing lattice vibrations (phonons[1]) and macromolecular structures. A fraction of the neutrons are guided from the reactor hall to the Neutron House where the instruments used in the present study are situated. The Neutron House provides a low background since undesirable, high energy neutrons have been removed by a curved neutron guide and the large distance from the reactor to the instruments.

X-ray measurements were performed using a Rigaku rotating anode located at the Physics Department at Risø. The anode was operated at 50 kV and 300 mA with copper as anode target material. For the experiments, the most intense characteristic line from the target with a wavelength of 1.54 Å was used.

3.1 Reflectivity

3.1.1 Neutrons

The neutron reflectometer, TAS8, was used for the experiments. A schematic drawing is shown in figure 3.1

Monochromator

As mentioned, the wavelength distribution from the reactor is Maxwellian,which is not the case for the rotating anode setup used. Figure 3.1.1 shows the difference in wavelength distribution from a neutron source and a conventional x-ray source.

The desired wavelength from the white beam is chosen by a monochromator crystal. At a given angle of incidence θ the neutrons are scattered from the monochromator in accordance with Bragg's law

$$n\lambda = 2d\sin\theta, \quad \text{where } n \text{ is the order of the reflection,} \quad n = 1, 2, 3, \ldots \tag{3.1}$$

d is the spacing between the reflecting planes in the crystal. The wavelength spread, described by the Darwin width [26, 27] (see appendix B), is very narrow for a perfect crystal. To increase the flux, the wavelength band is broadened. This can be obtained from a mosaic crystal, where the reflecting planes

[1] The excitation energy for phonons is od the order 1meV. The energy for 1Å and 10Å neutrons are 82meV and 0.82 meV respectively.

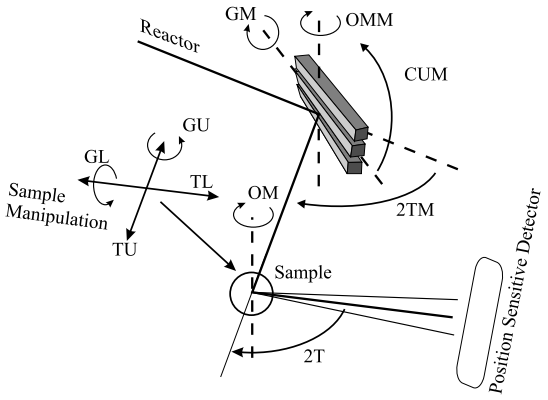

(a) A schematic drawing of the neutron reflectometer motor names.

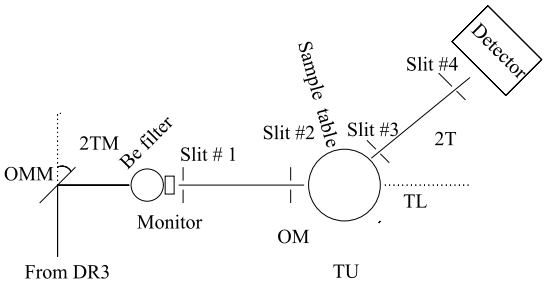

(b) A schematic drawing of active elements in TAS8.

Figure 3.1: The neutron reflectometer, TAS8.

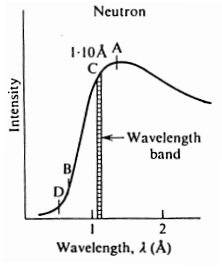

(a) The wavelength distribution from a neutron source.

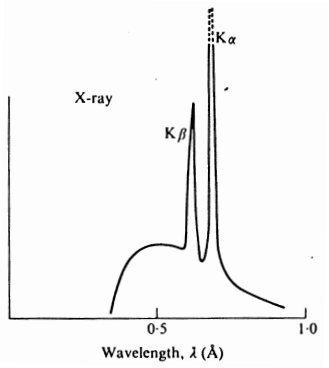

(b) Shows the characteristic lines from an ordinary x-ray setup.

Figure 3.2: Wavelength distributions from different sources. Adapted from [25].

are slightly misaligned. The monochromator used in TAS8 is a pyrolytic graphite (PG) crystal with a mosaicity of 0.5° and a momentum transfer $2\pi/d = q_{002} = 1.87325\text{Å}^{-1}$, which results in a wavelength of 4.75 Å.

The monocromator consists of several horizontal slabs of PG is illustrated in figure 3.1. The slabs can be turned around a horizontal axis to imitate a bent crystal. This makes it possible to focus the beam at the center of the sample table at the expense of vertical resolution, which is not important for our measurements.

Beryllium Filter

When the beam is reflected at a given angle, Bragg's law is satisfied not only for λ but also for higher order reflections, $\frac{\lambda}{2}, \frac{\lambda}{3}, \frac{\lambda}{3}, \ldots$. Consequently the beam from the monochromator will not only the desired wavelength, but also what is known as higher order contamination. This can be eliminated by inserting a beryllium filter after the monochromator. The function of the filter is to scatter the higher order neutrons

but transmitting the primary wavelength. The absorption cross section for a 2200 m/s neutron[2] is 0.0076 barns [28] hence Be is "transparent" to non-scattered neutrons. The crystal structure of beryllium is hexagonal close packed with lattice parameters $a = 2.286$ Å, $c = 3.584$ Å. Bragg's law tells that scattering occurs when

$$n\lambda = 2d\sin\theta \leq 2d \tag{3.2}$$

i.e. in the reciprocal space $k \geq \frac{nq}{2}$. The minimum scattering vector $q_{\min}$ with a non-zero structure factor $|F|^2$ determines the limit for **scattered** neutrons. The corresponding wavevector is $q_{\min} = 3.17$ Å^{-1} giving a cut-off wavelength of 4.0 Å. The cut-off wavelength was measured for the used filter and the result is shown in figure 3.3.

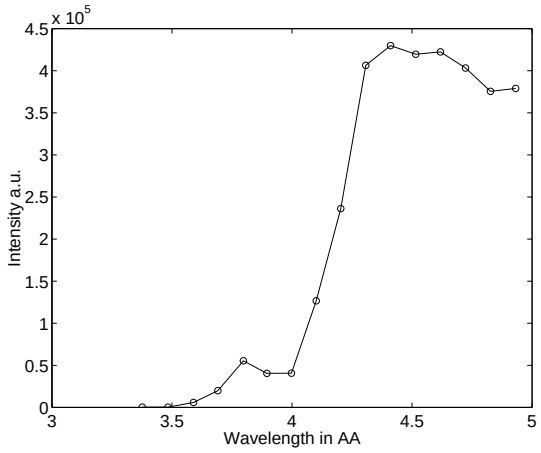

Figure 3.3: The cut-off wavelength was measured to be $\lambda_{\text{cut}-\text{off}} \sim 4.2$ Å.

Since the incoming neutron have energies comparable to those of phonons in the Be lattice, the filter has to be cooled with liquid nitrogen. The effect of phonon suppression is quite clear: The detected neutron transmission rate for a warm filter is approx. 4000 counts/s, whereas for a cold the monitor rate is approx. 9000 counts/s. The higher order scattered neutrons are absorbed by cadmium surrounding the sides of the beryllium to reduce the background.

[2]The wavelength of the neutron is given by $\lambda = h/p = 1.8$ Å.

Detector and Monitor

The scattered neutrons are detected in a gas detector containing a mixture of ^{3}He, which has a large absorption cross-section, 5333 barns [28] and a moderator gas of 80% argon and 20% methane. The detector gas is kept at a few atmospheres pressure. Neutrons interact with the helium gas to form

$$ {}^3_2\mathrm{He} + {}^1_0\mathrm{n} \rightarrow {}^1_1\mathrm{H} + {}^3_1\mathrm{H} + 0.76MeV. \tag{3.3} $$

The new particles creates a charged trace in the argon/methane gas. The charged particles formed accelerate towards an electrode. In the position sensitive detector the charge is measured as a function of arrival time at each side of the electrode. The difference in arrival time is a measure of the position between the electrodes. For this reason there is a maximum rate for which the detector will be linear. To measure this, a number of collimator sheets were inserted. A collimator sheet is a thin foil painted with ordinary paint mixed with Gd_2O_3, which is a strong neutron absorber (49000 barns [28])[3]. The resulting curve is shown in figure 3.4. Remembering that $I = I_0\ e^{-\mu x}$, where μ is the linear absorption coefficient and x the thickness (or number of absorbers), it is clearly seen that the detector is linear up to ca. 10000 cps.

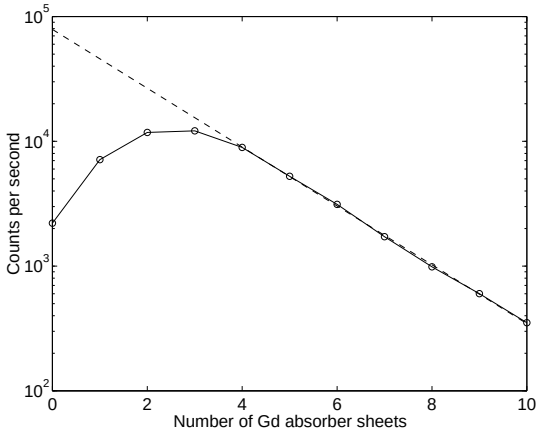

Figure 3.4: Detector tested for linearity and saturation limit. The beam was collimated with 2 mm slits to have a suitable attenuation of the beam. The maximum detection rate is ca. 10000 count/sec.

The monitor is working in a similar manner except that the pressure is much lower to allow for high transmission. A beam monitor is used, beacuse of temporal fluctuations of the flux from the reactor. The monitor detects approx. $1/10^6$ of the incoming neutrons.

Slits

To reduce the divergence of the beam from the monochromator, slits or collimators are inserted. The resolution of the instrument is determined by the collimation of the beam. The collimation can be obtained in two ways: Soller collimation[4] with a angular divergence of 0.2-1.0° or slits with a collimation from 0.003° and up. For a Soller collimator, the beam will be a collimated bundle whereas the slits will give a narrow beam. The slits are made of cadmium (which has an absorption cross-section of 2520 barns [28]) and a backside of boron plastic to reduce the remaining neutrons and the gamma radiation. The slits are motorized and can be adjusted in horizontal width and position.

The instrumental and experimental alignment is described in detail elsewhere [29], hence the alignment will only be briefly outlined.

- Select a suitable wavelength above $\lambda_{\mathrm{cut-off}}$ for the beryllium filter.

[3] The thickness of the foils is only 0.08 mm!

[4] Soller collimators are very thin parallel sheets of neutron absorbing material with small spacing between the sheets. The divergence is determined by the ratio between the spacing between the sheets and their lengths.

- Focus the beam on an Al_2O_3 powder sample placed at the center of the sample table, with a momentum transfer $q_{110} = 1.8049$ Å^{-1}.
- Inserting a pinhole at the center of the sample table to ensure focusing at the center of the sample table, when aligning the slits.
- Determination of the exact wavelength with 0.15° collimated beam using the Al_2O_3 (110) reflection.

The sample alignment will be described in greater detail. The alignment procedure using neutrons or x-rays is identical. The principle of the process can be described in only two points.

- Half of the beam must be intersected.
- The Incident beam should be parallel to the surface.

The only difference between neutrons and x-rays relates to the higher penetration power of neutrons. As can be seen in figure 3.5(a), the intensity does not go to zero when the sample and sample holder intersects the beam.

To demonstrate the relative minute absorption of neutrons in matter, a silicon wafer, 4 mm thick and 10 cm in diameter, was used. Half the beam is intersected when the intensity is halfway between the level of the direct beam and the level of the beam through the silicon wafer. The optimal position is indicated by the line separating silicon from air in figure 3.5(a). Next step in the alignment procedure is to have the incident beam parallel to the surface by scanning the sample rotation controlled by the motor OM. Again the higher penetration power of neutrons is demonstrated. As OM is changed from the center position the intensity decreases until the critical angle for silicon is reached (indicated by arrows in figure 3.5(b)). Up to the critical angle, neutrons are reflected, hence very low transmission is observed. The gradual increase after the critical angle shows the reduction in path length for the absorption. To optimize the sample position and check for perfect alignment, translation, OM and tilt are varied at an angle below the critical angle to gain maximum intensity ($I \propto q^{-4}$ for $q > q_c$, see section 3.2). At a given angle the scans change to Gaussian shapes. The three parameters are optimized recursively until convergence. The alignment can be checked (normally just OM-scans) at $q > q_c$ still near q_c to have reasonable counting time during alignment. Included in the macro controlling the entire scan a few OM-scans are included to test the alignment of the sample (figure 3.6).

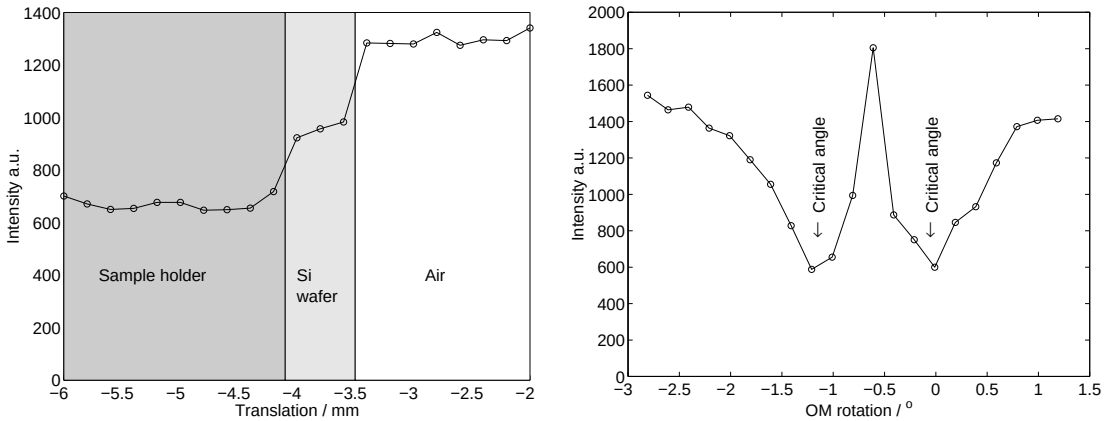

(a) Sample translation scan.

(b) Sample rotation scan.

Figure 3.5: Sample alignment scans for neutrons.

The absorption cross-sections σ tabulated [28] is given for neutrons with a wavelength of 1.8 Å. According to Bacon [25] the absorption cross section scales as $1/v$. Using $\lambda = h/mv$ we find that 1.8 Å

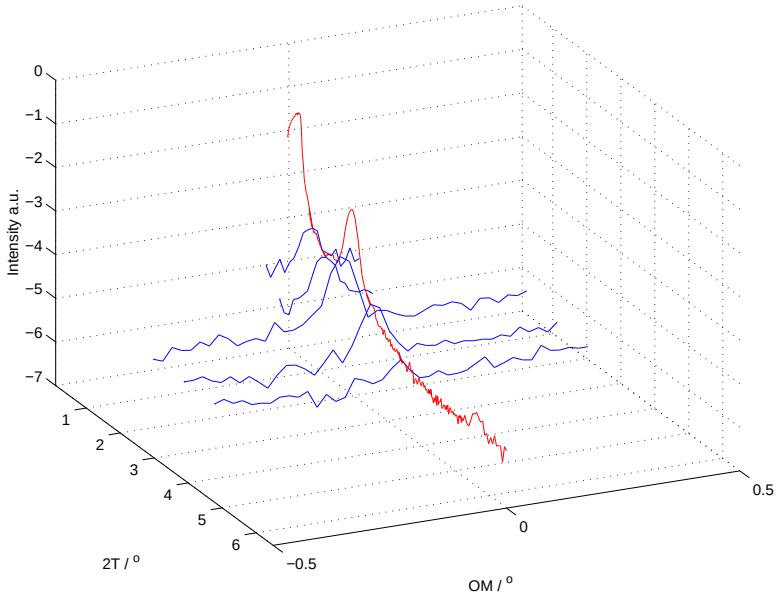

Figure 3.6: Neutron reflectivity curve (red) with OM-scans (blue) to check that the measured reflectivity curve corresponds to a specular configuration (incoming and outgoing angles are equal).

and 4.75 Å corresponds to 2200 m/s and 833 m/s respectively. The linear absorption coefficient can be calculated from the corrected absorption cross-sections.

$$\mu_{\mathrm{Al}} = \frac{\sigma N_A \rho}{M} = 0.037 \text{ cm}^{-1}$$

$$\mu_{\mathrm{Si}} = \frac{\sigma N_A \rho}{M} = 0.023 \text{ cm}^{-1}$$

where ρ is the density and M is the molar mass. The transmissions are then

$$\left.\frac{I}{I_0}\right|_{\mathrm{Al}} = \exp^{-\mu_{\mathrm{Al}} 10 \text{ cm}} = 69\%$$

$$\left.\frac{I}{I_0}\right|_{\mathrm{Si}} = \exp^{-\mu_{\mathrm{Si}} 10 \text{ cm}} = 80\%$$

From figure 3.5(a), we can see that the transmission is lower for both Al and Si (52% and 73% respectively). The reduced transmission might be explained by scattering from the silicon wafer and powder scattering from the sample holder. Both effects will give a reduced transmission.

3.1.2 X-rays

A schematic drawing of the x-ray setup used for reflectivity is shown in figure 3.7.

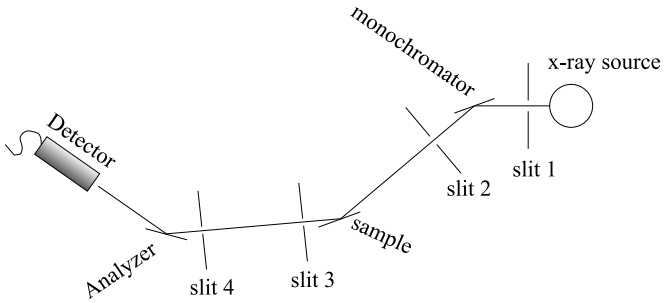

Figure 3.7: Rotating anode setup for x-ray reflectivity.

Monochromator and Analyzer

The spectrum (figure 3.2(a)) from an x-ray source is characterized by the characteristic lines from the anode material, which in this case is copper. The characteristic line is 1-2 orders of magnitude more intense than the Bremsstrahlung. To reduce other wavelengths from the continuous Bremsstrahlung spectrum, a monochromator crystal is mounted just after the beam. Since the intensity from an x-ray source is much more intense than a neutron source, a perfect crystal is used resulting in a better resolution. To remove the $Cu_{K\alpha 2}$ contamination and enhance the resolution an analyzer crystal may be inserted just before the detector, selecting the $Cu_{K\alpha 1}$ wavelength. Both the monochromator and analyzer crystals are perfect Ge(111) crystals.

Slits

The slit are made of tungsten. Tungsten is a heavy and tough material, which means that it is a good absorber material and can be processed to have very sharp edges resulting in well defined collimation of the beam. Slits 1 and 3 just act as guard slits with a width of 0.5-1.0 mm. Their function is simply to reduce background from the source and sample respectively. Slit 2 has two functions: removing $CuK_{\alpha 2}$ from the monochromator, and, together with slit 4, determine the resolution in the experiment. The resolution will be discussed in a later section 3.3.

Detector

The detector used in the x-ray setup is a scintillation detector (Bicron). The incoming x-ray photon is absorbed in a NaI crystal. The crystal subsequently emits a light with an intensity proportional to the x-ray photon energy. The light is converted to electrons at a photo catode. The electrons are multiplied in a cascade through a photomultiplier. Such detectors have low energy resolution compared to e.g. Ge detectors but the scintillation detector is robust and the high energy resolution is not required in this kind of experiments.

3.2 Theory of Reflectivity

In the last decades neutron and x-ray reflectivity have attracted an increased interest for studying structures of surfaces and thin films. The examples are numerous: liquid surfaces, Langmuir-Blodgett films, polymer surfaces, biological membranes, and magnetic films.

When rays (neutron or x-ray) impinge on a stratified medium, the *specularly* reflected beam (incident angle equals exit angle) will carry information about of the spatial composition perpendicular to the surface.

How do x-rays differ from neutrons? X-rays are electro magnetic radiation interacting with the electrons in the material, whereas the neutrons are particles interacting with the nuclei in the material. The modern synchrotron x-ray facilities offer very high flux resulting in short counting times and hence a better signal-to-noise ratio. A direct consequence is an improved spatial resolution. Since neutrons interact with the nuclei in the material they are sensitive to isotopic effects such as deuterium labeling. The absorption cross-section for neutrons is **very** low compared with x-rays, hence the penetration power for neutrons is high. Finally the neutron posses a spin, which makes it ideal for studying magnetic structures [30]. A combination of both neutron and x-ray reflectivity is a powerful tool for investigating multilayers and thin films.

3.2.1 Interaction with Matter

In this section x-ray and neutron interaction with matter will briefly be discussed. Consider scattering from a simple object, an electron or a proton. The *differential scattering cross section* $d\sigma/d\Omega$ is defined as [26]

$$I_s \equiv I_0 \Delta\Omega \frac{d\sigma}{d\Omega} \tag{3.4}$$

where I_0 is the incident particles per area per second being scattered into I_s particles per sec. per solid angle $\Delta\Omega$. It is assumed that the medium of point scatterers has a homogeneous density ρ and each point gives rise to a wavefunction, that in the limit of large distances, can be written as a spherical wave

$$\Psi_s = -b \frac{e^{ikR}}{R} \tag{3.5}$$

where b is the scattering length, k is the wavevector, and R is the distance. The sign is a result of the phase shift of the wave [26, 31].

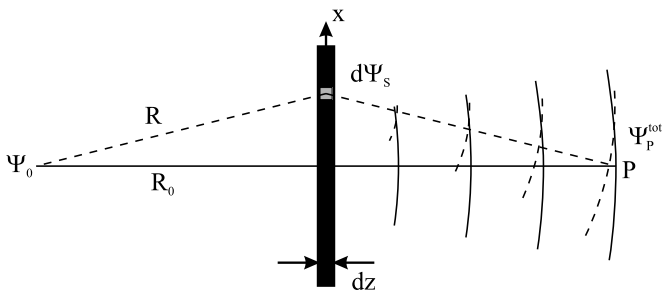

Figure 3.8: Scattering from an infinitesimally thin slab (only the x-dimension can be seen).

Considering the situation in figure 3.8, the scattering from a thin slab is the superposition of the scattering $d\Psi_s$ from the volume element $dx\ dy\ dz$. The scattered wave can be written as [26]

$$d\Psi_S = -b\ dx\ dy\ dz \rho \frac{e^{ikR}}{R} \sim -b\ dz\ \rho \frac{e^{ikR_0}}{R_0} \frac{e^{ikx^2}}{2R_0} dx \frac{e^{ikR_0}}{R_0} \frac{e^{iky^2}}{2R_0} dy \tag{3.6}$$

where ρ is the density of the scatterers and the denominator (for the spherical wave) has been approximated by $R \sim R_0$. However, this cannot be done for the phase factor, hence a Taylor expansion is introduced: $R = \sqrt{R_0^2 + x^2} \sim R_0 + \frac{x^2}{2R_0}$.

The total wavefunction at the observation point P, is a superposition of the incident wave $\Psi_0 = \frac{e^{ik2R_0}}{2R_0}$ and the scattered wave integrated over the slab area A

$$\Psi_{tot}^P = \Psi_0 + \int_A d\Psi_S$$

$$d\Psi_S = -b\rho dz \frac{e^{i2kR}}{R^2} \int \frac{e^{ik(x^2+y^2)}}{R_0} dxdy \tag{3.7}$$

where the integral is equal to $i\pi R_0/k$. Inserting this result leads to

$$\Psi_{tot}^P = \Psi_0 + \int_A d\Psi_S = \frac{e^{ik2R_0}}{2R_0} \underbrace{\left(1 - \left(i\frac{2\pi}{k} dzb\rho\right)\right)}_{1-i(n-1)dzk)} \tag{3.8}$$

where $n = 1 - (\frac{2\pi}{k^2}\rho b)$ is the refractive index equivalent to what is known from ordinary optics. As a final remark, ρb in the refractive index differs slightly for x-ray and neutrons:

X-rays: ρb is the electron density times the Thomson scattering length $r_0 = 2.82$ fm.

Neutrons: ρb is the density of the material times the scattering length, which can be found in tables [28].

3.2.2 Reflectivity Equations

For both neutrons and x-rays, unlike for visible light, the refractive index n for a medium is slightly less than unity and given by

$$n = 1 - \delta + i\beta \tag{3.9}$$

where the imaginary part arises from absorption in the medium.

For x-rays the real term is given by the sum of elements in a unit of the material [32]

$$\delta_x = \frac{\lambda^2}{2\pi} r_0 N_A \sum_i \frac{\rho_i}{A_i}(Z_i + f') \tag{3.10}$$

where r_0 is the Thomson scattering length, λ is the wavelength, A is the atomic weight, Z is the atomic number, f' is the real anomalous dispersion factor, and N_A is Avogadro's constant. The absorption term is given by [32]

$$\beta_x = \frac{\lambda^2}{2\pi} r_0 N_A \sum_i \frac{\rho_i}{A_i} f'' \tag{3.11}$$

where f'' is the imaginary anomalous dispersion factor.

The equation can be simplified when considering polymers as they consists of carbon and oxygen with small f' and similar f''. In the real part, the sum can be approximated as the electron density ρ_{el} and the imaginary term as the mass absorption coefficient μ

$$\delta_x = \frac{\lambda^2}{2\pi} r_0 \rho_{el} \tag{3.12}$$

$$\beta_x = \frac{\lambda}{4\pi} \mu \tag{3.13}$$

In the case of neutrons, the magnetic aspect has to be considered. Since polymers in general are non-magnetic substances the spin interactions can be neglected. Furthermore, the absorption of neutrons in matter (except for B, Gd, Sm and Cd) is negligible.

$$\delta_N = \frac{\lambda^2}{2\pi} N_A \sum_i \frac{\rho_i}{A_i} b_i \tag{3.14}$$

where b_i is the scattering length of element i. As mentioned earlier, δ might not always be positive, for which hydrogen ^{1}H is an example. The equation can be simplified to a more suitable equation for polymers

$$\delta_N = \frac{\lambda^2}{2\pi} N_A \frac{b_{mon}}{M_{mon}} \rho_{mon} \tag{3.15}$$

where b_{mon}, M_{mon} and ρ_{mon} is the scattering length, molecular mass and density of a monomeric unit. Reflectivity curves can be described by the *dynamical* or *kinematical* theory. The latter is based on an approximation.

3.2.3 Dynamical Theory

In this section we derive the dynamical theory starting with the simplest case involving scattering from a semi-infinite layer. Then considering multiple scattering in a single layer, and finally deriving the Parratt formalism [33] for an arbitrary multilayer, which can be used to describe most materials, where the film can be described by several stratified layers.

Semi-infinite layer

Considering an interface separating two media with refractive indices n_0 and n_1, an incident wave $a_I \mathbf{k}_I = e^{i\overline{k}\cdot\overline{r}}$ will be reflected as $a_R \mathbf{k}_R$ and refracted as $a_T \mathbf{k}_T$ [26].

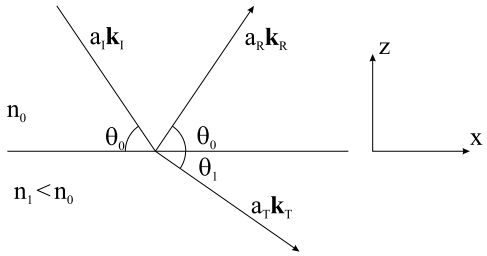

Figure 3.9: Incident wave at an interface.

Taking the boundary conditions at $z = 0$

$$a_I + a_R = a_T \tag{3.16}$$

$$a_I \mathbf{k}_I + a_R \mathbf{k}_R = a_T \mathbf{k}_T \tag{3.17}$$

and splitting up in x-and z-component we get respectively

$$a_I n_0 k \cos\theta_0 + a_R n_0 k \cos\theta_0 = a_I n_1 k \cos\theta_1 \tag{3.18}$$

$$-a_I n_0 k \sin\theta_0 + a_R n_0 k \sin\theta_0 = -a_I n_1 k \sin\theta_1 \tag{3.19}$$

where $k = |\mathbf{k}_I| = 2\pi/\lambda$ and since the energy is conserved; $|\mathbf{k}_I| = |\mathbf{k}_R| = |\mathbf{k}_T|$. Combining the boundary conditions with eqn. (3.18) we obtain Snell's law

$$n_0 \cos\theta_0 = n_1 \cos\theta_1 \tag{3.20}$$

Considering the case in figure 3.9 where $n_0 > n_1$ we see that the angle of the refracted beam is smaller than the incident. At a sufficiently small incident angle (the *critical angle* θ_c), the refracted angle will be zero. This phenomena is called *total reflection*. By expansion of Snell's law it can be shown that the critical angle at an interface between vacuum and matter with scattering density δ is

$$\theta_c = \sqrt{2\delta} \tag{3.21}$$

keeping in mind that the refractive index for vacuum is unity. The reflected intensity from a surface or interface depends on the differences in momentum transfer in the media. Since we are interested only in specular reflection only the component normal to the surface of the wavevector is to be considered i.e. equation 3.19. In combination with the boundary condition we get Fresnel's law

$$\frac{a_I - a_R}{a_I + a_R} = n_1 \frac{\sin\theta_1}{\sin\theta_0} \tag{3.22}$$

The definition of reflectivity amplitude or reflectance is given as the ratio between the incident and reflected amplitudes

$$r \equiv \frac{a_R}{a_I} = \frac{\sin\theta_0 - \sin\theta_1}{\sin\theta_0 + \sin\theta_1} \tag{3.23}$$

Introducing the reciprocal lattice vectors $q = 2k\sin\theta_0$ and $q' = 2k\sin\theta_1$ the reflectivity amplitude can be written more conveniently as

$$r = \frac{q - q'}{q + q'} \tag{3.24}$$

where q' can be expressed as

$$q' = \sqrt{q^2 - q_c^2} = \sqrt{q^2 - 8k^2\delta} = \sqrt{q^2 - 16\pi\rho'} \tag{3.25}$$

In the figure below there are two examples of the Fresnel reflectivity with a positive and a negative δ. As can be seen, the negative scattering density does not exhibit total reflection.

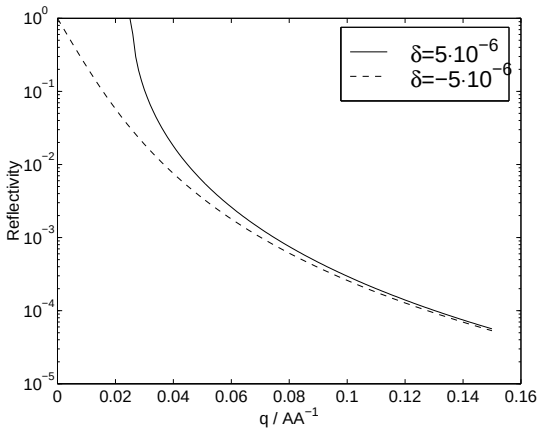

Figure 3.10: Fresnel reflectivities. The difference between positive and negative scattering length densities.

Multiple Scattering from a Single Layer

Considering a single layer, we investigate the different possibilities for scattering at the interfaces. The incident beam will be reflected at the first interface with the reflectance $r_{0,1}$ but also be transmitted with the transmittance $t_{0,1}P$ including the phase factor $P = \exp(-iQ'd)$, where $Q' = 2k\sin\theta'$. The transmitted beam will then be reflected at the second interface now having the reflectance $r_{1,2}t_{0,1}P^2$. Naturally a part will also be transmitted but it is without interest for the measured intensity. At the first interface, the beam reflected from the second interface is split in a transmitted part that contributes to the total reflectance and a reflected part that travers the layer again to be split at the second interface and so the scattering process continues.

This scheme continues throughout the layer [26].

This kind of scattering at the interfaces is called *multiple scattering*. Hence the total reflectance is a sum of all the contributions

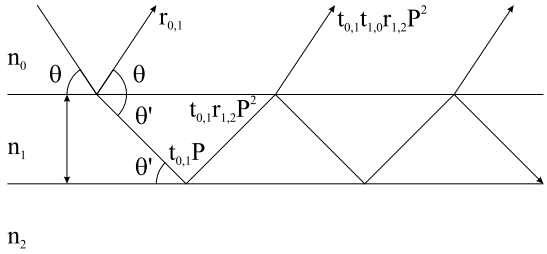

Figure 3.11: Multiple scattering in a single layer.

$$\begin{aligned} r &= r_{0,1} + t_{0,1}t_{1,0}r_{1,2}P^2 \\ &+ t_{0,1}t_{1,0}r_{1,2}^2 r_{1,0}P^4 \\ &+ t_{0,1}t_{1,0}r_{1,2}^3 r_{1,0}^2 P^6 \\ &+ \cdots \end{aligned} \tag{3.26}$$

which can be written as a series

$$r = r_{0,1} + t_{0,1}t_{1,0}\sum_{j=1}^{\infty} r_{1,2}^j r_{1,0}^{j-1} P^{2j} \tag{3.27}$$

Summation to infinity of the series gives

$$r = r_{0,1} + t_{0,1}t_{1,0}\frac{r_{1,2}P}{1 - r_{1,0}r_{1,2}P} \tag{3.28}$$

Introducing the relationships [26]

$$\begin{aligned} r_{0,1} &= -r_{1,0} \\ t_{0,1}t_{1,0} &= 1 - r_{0,1}^2 \end{aligned} \tag{3.29}$$

It can be simplified to

$$r = \frac{r_{0,1} + r_{1,2}P}{1 + r_{0,1}r_{1,2}P} \tag{3.30}$$

Parratt formalism

Parratt [33] generalized the multiple scattering for a single layer to an arbitrary profile. This is also known as the *full dynamical theory*. Considering a profile divided into n layers, each layer labeled j, where $j = 0$ is defined as the vacuum and $j = n + 1$ as the substrate.

Starting with layer $j = n$ the reflectance is given by the Fresnel reflectance (eqn. 3.24)

$$r'_{j,j+1} = \frac{q_{j+1} - q_j}{q_{j+1} + q_j} \tag{3.31}$$

with $q_j = 2k\sin\theta_j$.

In the next layers ($j \leq n - 1$) the reflectance is given by eqn. (3.30)

$$r_{j-1,j} = \frac{r'_{j-1,j} + r'_{j,j+1}P}{1 + r'_{j-1,j}r'_{j,j+1}P} \tag{3.32}$$

The prime denotes the non-phase corrected Fresnel reflectance (eqn. 3.31). Calculation of the reflectances continues recursively until $r_{0,1}$ is reached. The total reflectivity from the multi layers is then given by

$$R = r_{0,1}r_{0,1}^* \tag{3.33}$$

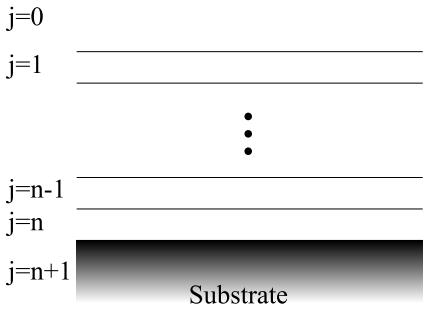

Figure 3.12: Parratt generalization of a stratified medium.

Roughness

So far all interfaces (and the free surface) have been assumed infinitely sharp, which under most normal conditions is far from reality. Roughness of an interface is not to be confused with a macroscopical curvature of the interface (see figure 3.13) [32]. For a curved surface, the radius of curvature is much larger

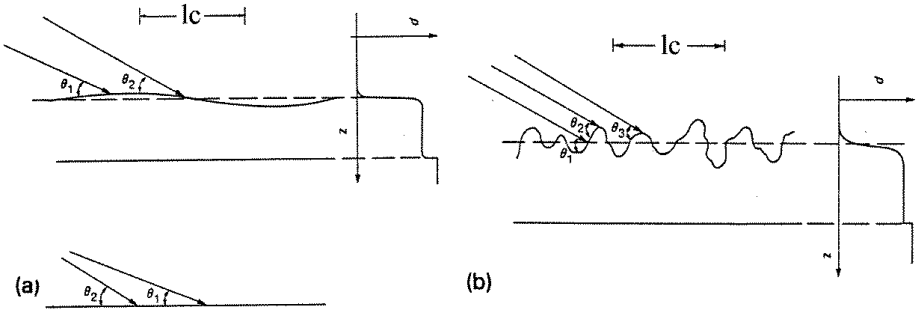

Figure 3.13: Waviness (a) and roughness (b) of an interface.

than the coherence length of the incident radiation l_c, whereas for a rough surface the curvature changes occur on a scale smaller than the coherence length. For the situation in 3.13(b) the deviation from the average height of the interface can be described by Gaussian statistics [32] with the corresponding smearing function

$$g(z) = \frac{1}{\sqrt{2\pi}\sigma} \exp(-z^2/2\sigma^2) \tag{3.34}$$

where z is the depth and σ is the standard deviation from the average height of the interface. The roughness for each layer is incorporated in the Parratt formalism in equation 3.31 as

$$r'_{j,j+1} = \frac{q_j - q_{j-1}}{q_j + q_{j-1}} \exp\left(-\frac{1}{2}\left(\frac{q_j q_{j+1}}{\sigma_j}\right)^2\right) \tag{3.35}$$

3.2.4 Kinematical Approximation

The kinematic approximation is based on two approximations and one correction. If a scattering length profile can be describe by an analytical expression, the kinematical approximation is useful. If there is an exponential decay of the scattering in the film, the dynamical theory is inadequate because there will be a gradual change across the box in the Parratt model. However, the kinematical approximation uses the derivative of the scattering length profile to calculate the reflectivity curve [34].

We earlier derived the Fresnel reflectivity eqn. (3.31) for an arbitrary layer $j, j+1$. Generalizing eqn. (3.25)

$$q_j = \sqrt{q^2 - (q_j^c)^2} \tag{3.36}$$

and combining these equation with the Taylor expansion of

$$\sqrt{1-x} \sim 1 - \frac{1}{2}x^2 \ , \text{ for small } x \tag{3.37}$$

we get the **first approximation**

$$r_{j,j+1} = \frac{\sqrt{1-\left(\frac{q_j^c}{q}\right)^2} - \sqrt{1-\left(\frac{q_j^c}{q}\right)^2}}{\sqrt{1-\left(\frac{q_j^c}{q}\right)^2} + \sqrt{1-\left(\frac{q_j^c}{q}\right)^2}} \tag{3.38}$$

In the limit where $q \gg q_j^c$ for all j we get

$$r_{j,j+1} = \frac{1}{4}\left(\frac{q_{j+1}^{c2}}{q^2} - \frac{q_j^{c2}}{q^2}\right) = 4\pi\frac{\rho_{j+1}-\rho_j}{q^2} \tag{3.39}$$

The **second approximation** is introduced in the correction of the phase factor for the reflectance

$$r = \sum_{j=0}^{n} r_j r_{j+1} \exp(-iqd_j) \tag{3.40}$$

where $d_{j=0} = 0$ for vacuum. Hence

$$r = 4\pi \sum_{j=0}^{n} \frac{\rho_{j+1}-\rho_j}{q^2} \exp(-iqd_j) \tag{3.41}$$

in the limit of an infinite number of infinitesimally thin layers, it can be written as an integral

$$r = \frac{4\pi}{q^2}\int_{-\infty}^{\infty} \frac{d\rho(z)}{dz} \exp(-iqz)dz \tag{3.42}$$

The reflectivity is now given as

$$R = rr^\star = \left(\frac{4\pi}{q^2}\right)^2 \left|\int_{-\infty}^{\infty} \frac{d\rho(z)}{dz} \exp(-iqz)dz\right|^2 \propto q^{-4} \tag{3.43}$$

and is known as the *weak-scattering approximation*, termed by Lekner [35]. It is called weak scattering, because it is assumed that each slab scatters weakly, hence multiple scattering can be neglected.

The **correction** used in the kinematical approximation corrects for refraction by substituting q in the phase factor with $q' = \sqrt{q^2 - (q_{\text{sub}}^c)^2}$ where q_{sub}^c is the critical angle for the substrate. This step, introduced by Als-Nielsen and Kjaer [36] leads to the well know *master formula* for reflectivity within the kinematic approximation.

$$R = R_F(q)\left|\frac{1}{\rho_{\text{sub}}}\int_{-\infty}^{\infty} \frac{d\rho(z)}{dz} \exp(-iq'z)dz\right|^2 \tag{3.44}$$

where $R_F(q) \sim (4\pi\rho_{\text{sub}})^2/q^4$ is the Fresnel reflectance and ρ_{sub} is the scattering density of the substrate [34].

As a concluding remark it should be noted that the roughness is incorporated in the scattering length density profile $\rho(z)$. This means that the kinematic model is more suitable for experiments with different interface profiles. The interface can be described by an error function or hyperbolic tan. The interface might even be asymmetric, if that can be assigned a physical property. Finally if the scattering length profile has a large roughness compared to the box size in the dynamical theory, errors in the reflectivity curve might occur. This problem can be solved by using the kinematical theory.

3.3 Resolution

It is important to consider the resolution of the reflectometer, because the resolution determines the minimum size of features that can be measured, and features in the reflectivity curve might disappear due to resolution smearing. For that purpose a *resolution function* is introduced. The resolution function of the instrument is defined as the probability of detecting photons or neutrons as a function of Δq. The two different setups discussed in the previous section will be discussed here; the two-axis used with neutrons and the standard setup for x-rays, and the three-axis setup used for high resolution x-ray measurements.

3.3.1 Resolution for a Two-Axis Reflectometer

To calculate the resolution function we use the scattering vector Q related to the scattering angle θ by

$$Q = \frac{4\pi}{\lambda}\sin\theta \tag{3.45}$$

where both λ and θ contribute to the instrumental smearing. Considering the angular divergence, we take the derivative of eq. 3.45 with respect to the angle θ

$$\Delta Q_{\text{ang}} = \frac{4\pi}{\lambda}\cos\theta\Delta\theta \sim \frac{4\pi}{\lambda}\Delta\theta \tag{3.46}$$

where we have used that $\theta \ll 1$.

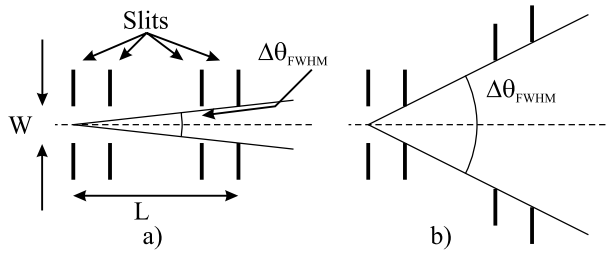

Figure 3.14: Two different slit geometries. a) Symmetric. b) Asymmetric.

In specular reflectivity the angular divergence is the same for both the direct beam and the reflected beam. Hence the collimation is determined by the slit geometry. In the symmetric case (see figure 3.14), where all the slits have the same width the, FWHM (full width at half maximum) of the collimation is determined by

$$\Delta\theta_{\text{FWHM}} = \frac{W}{L} \tag{3.47}$$

where W is the width of the slits and L is the longest distance between the first and last slit[5]. In the asymmetric case, where the widths of the slits are different, the largest width determines the collimation [37]. The resolution cannot be determined directly just by measuring the beamprofile for a two-axis reflectometer [37], but it might give an idea of the magnitude. The wavelength spread can be found by taking the derivative of eqn. 3.45 with respect to the wavelength λ

$$\Delta Q_\lambda = -\frac{4\pi\Delta\lambda}{\lambda^2}\sin\theta = -\frac{\Delta\lambda}{\lambda}Q \tag{3.48}$$

where the wavelength spread can be related to the mosaic spread of the monochromator η [37]

$$\frac{\Delta\lambda}{\lambda} = \frac{\eta}{\tan\theta_{\text{mon}}} \tag{3.49}$$

[5] $\tan\theta_{\text{HWHM}} = \frac{W/2}{L} \sim \theta_{\text{HWHM}}$ (half width at half maximum).

θ_{mon} is the diffraction angle for the monochromator crystal.

Since the resolution contributions are Gaussian-like the resolution is given as the squared sum.

$$\Delta Q = \sqrt{\Delta Q_{\lambda}^2 + \Delta Q_{\text{ang}}^2} \tag{3.50}$$

In figure 3.15, the resolution function has been plotted as a function of the scattering vector. The steps in the figure arise from the change in the width of the slits to increase the flux.

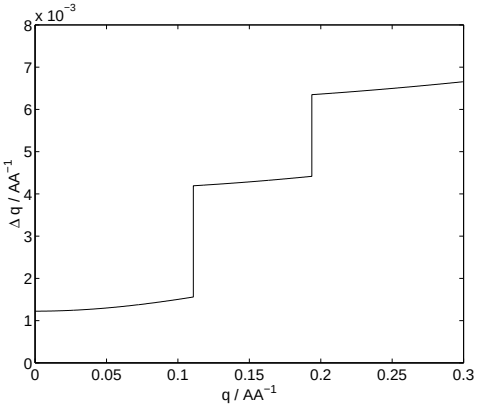

Figure 3.15: The resolution function for a typical neutron measurement in this thesis. The steps in the figure arise from the change in slit width to increase the flux.

3.3.2 Resolution Function for a Three-Axis Spectrometer

High resolution reflectometry can be performed on a three-axis spectrometer. The flux is not high enough at a neutron source to add a perfect analyzer crystal, however, even conventional x-ray sources are bright enough to add the analyzer crystal. For the very thick PS-PDMS films (discussed later) an analyzer was imperative to resolve the fringes.

This section is based on an article by Cowley [38]. The resolution function is based on two assumptions: the angular divergences are determined by the monochromator and analyzer crystal, and the Darwin widths can be approximated by Gaussians for non-absorbing crystals. The slits in the setup, only serves as guards to eliminate background and define the beam. Apart from increasing the resolution, an analyzer crystal eliminates contributions from the $\text{Cu}_{K\alpha 2}$ line in the source as seen in figure 3.16.

The in-plane resolution function for wavevector transfer $\mathbf{Q}_0$ is given as

$$R(\mathbf{Q}_0 + \Delta\mathbf{Q}) = R_0 \exp(\tfrac{1}{2}\mathsf{M} + \Delta\mathbf{Q}) = R_0 \exp\left[\tfrac{1}{2}\left(M_{11}\Delta Q_x^2 + 2M_{12}\Delta Q_x \Delta Q_y + M_{22}\Delta Q_y^2\right)\right] \tag{3.51}$$

For a conventional source, the matrix elements in the resolution function are given as

$$A' = \frac{(\tan\theta - \tan\theta_A)^2}{D_A^2} - \frac{(\tan\theta - \tan\theta_M)^2}{D_M^2} + \frac{1}{\sigma^2} \tag{3.52}$$

$$\begin{aligned} M_{11} &= \frac{M_{11}^x + M_{11}^c}{4A'k^2\cos^2\theta} \\ M_{12} &= \frac{M_{12}^x + M_{12}^c}{4A'k^2\cos\theta\sin\theta} \\ M_{22} &= \frac{M_{22}^x + M_{22}^c}{4A'k^2\sin^2\theta} \end{aligned} \tag{3.53}$$

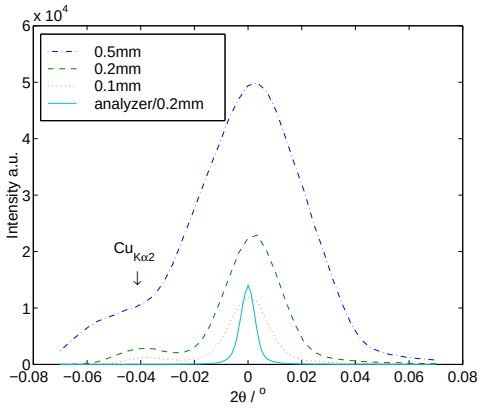

Figure 3.16: Beam profiles for different slit geometries and incorporation of an analyzer crystal. As can be seen, narrower slits give narrower beamprofiles. Introducing an analyzer crystal constricts the beamprofile and eliminates the $Cu_{K\alpha 2}$ contamination.

The M^x terms are

$$\begin{aligned} M^x_{11} &= \frac{(\tan\theta_M - \tan\theta_A)^2}{D_M^2 D_A^2} \\ M^x_{12} &= \frac{(\tan\theta_M - \tan\theta_A)(2\tan\theta - \tan\theta_M - \tan\theta_A)}{D_M^2 D_A^2} \\ M^x_{22} &= \frac{(2\tan\theta - \tan\theta_M - \tan\theta_A)^2}{D_M^2 D_A^2} \end{aligned} \tag{3.54}$$

The line width of the source in incorporated in the M^c terms

$$\begin{aligned} M^c_{11} = M^c_{22} &= \frac{1/D_A^2 + 1/D_M^2}{\sigma^2} \\ M^c_{12} &= \frac{1/D_M^2 - 1/D_A^2}{\sigma^2} \end{aligned} \tag{3.55}$$

where the monochromator and analyzer reflects at θ_M and θ_A respectively. The width of the reflection is given by the Darwin widths D_M and D_A. $\sigma = 3.0 \cdot 10^{-4}$ is the line width of the $Cu_{K\alpha 1}$ line. Warren [27] gives the Darwin width for a perfect, non-absorbing crystals in an unpolarized beam

$$D = 2.12 \frac{r_e N \lambda^2 |F|}{\pi \sin(2\theta)} \frac{1 + |\cos(2\theta)|}{2} \tag{3.56}$$

where r_e is the Thomson scattering length, N is the number of atoms per volume, F is the structure factor and θ is the scattering angle.

The monochromator and analyzer in the experiment were both perfect Ge(111) crystals. The Darwin width for the crystal is calculated in appendix B to be $8.03{\cdot}10^{-5}$ rad. There are two possible ways the analyzer crystal can be incorporated. In the present setup the monochromator scatters counterclockwise and the sample clockwise. The analyzer can then be inserted to scatter clockwise or counterclockwise which will be abbreviated $+-+$ and $+--$ respectively. By inspection of Cowley's equations, it is clear that the resolution is different for the two configurations. Inserting the known parameters in Cowley's equations, it can be seen (figure 3.17(a)) that for reflectivity $+--$ provides the best resolution. However, at higher Q-values (figure 3.17(b)), around the scattering vector of the crystals, $+-+$ gives the best resolution.

The resolution functions are incorporated in fitting routines by folding the scattering function with the resolution function giving the corrected scattering intensity $I_C(Q)$

$$I_C(Q) = \int I_T(Q') g(Q, Q - Q') dQ' \tag{3.57}$$

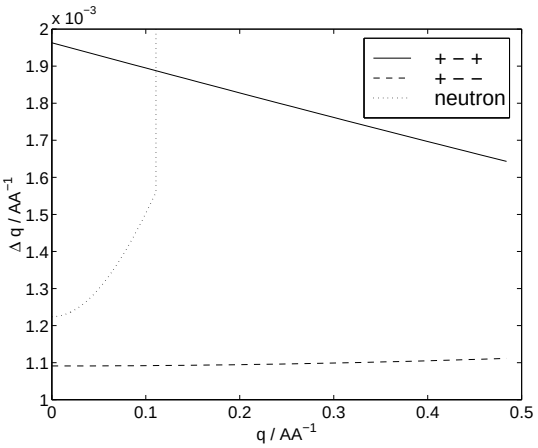

(a) The resolution functions for low q-values. The resolution function for neutrons calculated in the previous section is inserted for comparison.

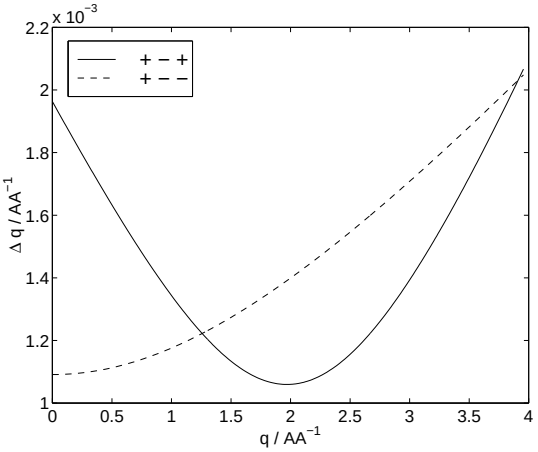

(b) The resolution functions for higher q-values.

Figure 3.17: Resolution functions based on Cowley's equations.

where $I_T(Q')$ is the theoretical scattering function and $g(Q, Q-Q')$ is the resolution function for the three-axis mode eq. 3.51 and the the two-axis eq. 3.50 in the Gaussian form $\exp(-\frac{1}{2}(Q-Q')^2/\Delta Q^2)$. For numerical purposes it is sufficient to calculate the integral from $3\Delta Q$ to $3\Delta Q$.

3.4 Small Angle Scattering

Small angle scattering is a very powerful tool for investigating mainly bulk polymer melts. Since the dimensions of the molecules are in the range from nanometers to micrometers the scattering angle becomes *very* small. Especially neutrons have proven extremely powerful for studying hydrocarbons, because different parts of the polymer can be labeled by deuterium instead of hydrogen. The scattering length is very different for the two isotopes, hence dramatic contrast variations can be made. Such contrast variations can not be introduced when using x-rays but the high intensity available at x-ray source allows for higher resolution and/or higher dynamical range.

3.4.1 X-rays

Small Angle X-ray Scattering (SAXS) was used to check for x-ray contrast in the system and to determine the lamellar period.

The configuration is simple as can be seen in figure 3.18. A monochromator selects a wavelength from the source, and the monochromatic beam is then collimated by slits. The scattered radiation is detected on an image plate, which has a high resolution and a good dynamical range for the intensities.

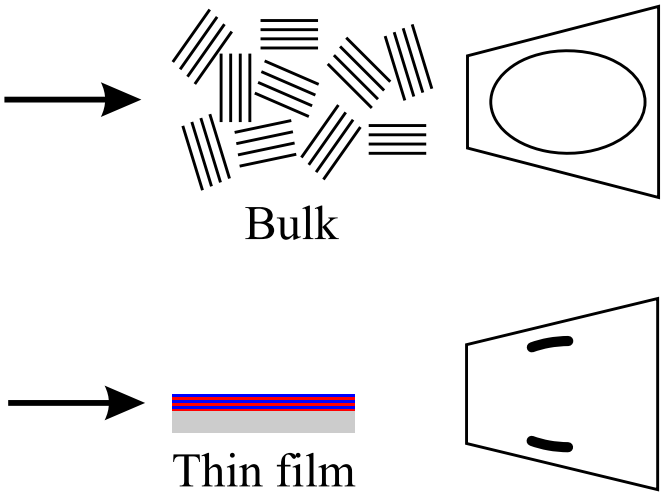

Figure 3.18: Small angle scattering setup. The upper image describes the scattering from a bulk sample, whereas the lower illustrates the setup used for investigating the thin film by SANS.

3.4.2 Neutrons

The Small Angle Neutron Scattering (SANS) was used to find characteristic lengths in thin films and for comparison with bulk polymer samples. The SANS was equipped with an oven with nitrogen flow to prevent oxidation of the polymer. This oven was used to test the scaling relations for the thin films and bulk samples.

The white neutron beam is monochromated by a velocity selector. The wavelength of the neutron scales with the velocity as $\lambda \propto 1/v$, so by selecting neutrons with a speed corresponding to the desired wavelength, a monochromatic beam can be obtained.

Chapter 4

Sample Preparation

In this chapter the sample preparation of the thin films for the reflectivity measurements and the bulk samples for the small angle measurements will be described. The polymers used were synthesized prior to the project and were used without further purification. For the thin films some of the problems in the preparation will be discussed.

4.1 Thin films

The thin film samples were spin casted on silicon wafers for two reasons: commercially available silicon wafers are relatively inexpensive and are very flat. For reflectivity measurements the roughness of the substrate has a large impact on the reflectivity curve. A number of reflectivity curves have been simulated to demonstrate the effect of roughness (see figure 4.1). A rough film ($\cdots$) will diminish the signal from the polymer thin film, leaving only the Fresnel curve of the substrate at higher q-values (> 0.12 Å^{-1}). A rough substrate ($- \; -$) will also suppress the signal from the thin film and attenuate the signal. If both polymer thin film and substrate are rough ($\bullet \; \bullet$), the reflectivity curve vanishes at $q \sim 0.12$ Å^{-1}.

Si(100) wafers were used with a thickness of ca. 500 μm and no preferential doping. For the neutron experiments whole wafers were used, whereas for the x-ray experiments the wafers were cut in 3×3 cm^2 pieces.

4.1.1 Piranha Cleaning

Before the substrates were used they were cleaned in a Piranha solution, which is a mixture of 2/3 concentrated (96%) sulfuric acid (H_2SO_4) and 1/3 concentrated (30%) hydrogenperoxide (H_2O_2). The mixing is a highly exothermic reaction where the temperature of the solution reaches approx. 90°C. The Piranha solution reacts with organic and metallic contamination and leaves the silicon surface oxidized (SiO_2) and hydrophilic. The solution was poured over the wafer and left to react for about 10 minutes. The wafers had to be handled with teflon tweezers due to the reactivity towards metals.

The wafers were rinsed with Millipore water and dried with a cloth at the edge of the wafer. The cloth tends to suck the water away from the surface. Minor droplets were blown away by compressed air. Until late in the project it was not realized that compressed air was used. Up to that point, it was assumed to be an inert gas. It is believed that it did not influence the spin casting results in an undesirable way. Problems in the spin casting procedure will be discussed in the next section. The quality of the Piranha reaction can easily seen by complete wetting of the surface by water when rinsing the wafers after reaction. The wafers were used immediately after the rinse.

4.1.2 Spin Casting

Spin casting is a widely used technique to prepare thin (0.2 μm-2 μm) uniform and homogeneous films. Particularly the electronics industry use this technique to coat surfaces of micro components.

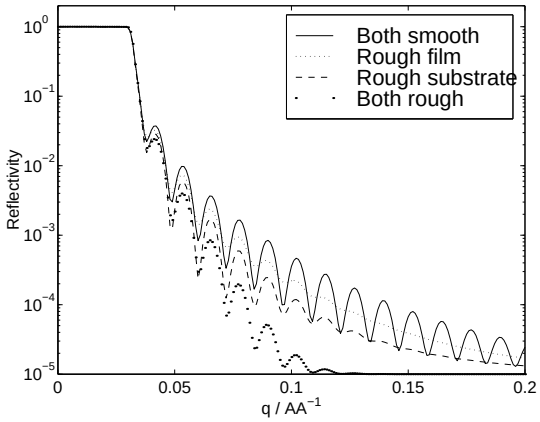

Figure 4.1: Simulated reflectivity curves for different roughnesses in the system. The roughness used for both materials was chosen to be 20 Å. The curves have been resolution smeared and an estimate of the background ($1 \cdot 10^{-5}$) has been added.

The substrate was completely flooded by solution and then spun with rotation speeds from 1000 rpm to 6000 rpm until the solvent had evaporated. Experiments showed that the acceleration is a crucial factor for the coverage of the substrate and uniformity. Maximum acceleration gave the best results.

The spin castings were carried out in a semi-clean room. It was not required that the surface was completely free of impurities in the form of dust, since the reflectivity measurements will average over a large area compared to the dust particles and the resulting inhomogenities. An example is shown in figure 4.2. As seen the dust particles impose rims of excess material.

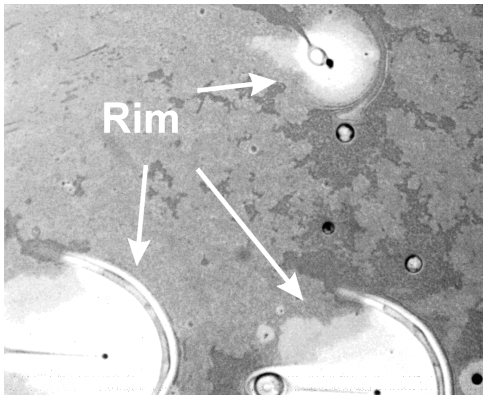

Figure 4.2: Surface impurities inducing rims of excess polymer on the surface.

4.1.3 Parameters Controlling the Film Thickness

The thickness of the film t is a function of the spinning speed ω

$$t \propto \omega^{-\alpha} \tag{4.1}$$

where α has been found to vary from 0.4 to 0.7 [39]. The theoretical value [39], 0.67, is based on the assumption that the fluid can be described as a Newtonian fluid, with a volumetric constant flow and no evaporation.

Weill and Dechenaux [39] proposed a possible mechanism for the formation of the thin film including evaporation from the surface during spin casting.

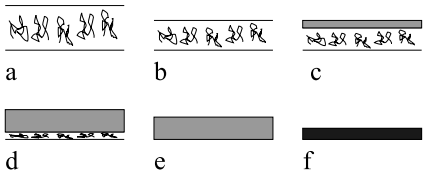

Figure 4.3: Schematical mechanism for spin casting.

Two transport phenomena are present simultaneous: a radial flow of solution, and an evaporation of solvent perpendicular to the surface. The schematical mechanism of the process is illustrated in figure 4.3 and can be described in the following steps:

a) The homogeneous film of solution covers the substrate uniformly.

b) The radial flow leads to a decrease in the thickness

c) Evaporation from the surface introduces a concentration gradient in the solution. As the concentration reaches the critical concentration, at which the solution starts to behave like an elastic solid, an elastic "crust" is formed.

d) The solution still flows viscously radially and the thickness decreases in time as the "crust" increases.

e)+f) When the "crust" takes up the entire film, the thickness reduction is caused by the evaporation of residual solvent.

4.1.4 Thickness Measurements

A number of parameters controlling the thickness of the film were varied. PS-PDMS (25k-25k) was used for this experiment, since the available amount of PEP-PDMS was rather limited and the general properties are not that sensitive to the type of polymer. The thicknesses were measured by AFM in a cross-section of the surface. A needle of welding wire was used to carve a narrow groove in the polymer film without scratching the substrate.

The spinning speed was the easiest parameter to control since it only required one solution. The second parameter changed was the concentration of polymer in the solvent keeping the same spinning speed for all samples. The last parameter changed in this experiment was the choice of solvent. The interaction parameter χ for PS-PDMS in chloroform and cyclohexane was plotted in figure 2.6. This shows that the interaction parameter for the PS-block is soluble in chloroform at higher volume fractions, which is not the case for cyclohexane. This could result in different resulting structures and since the structures are formed below T_g, they will be "frozen" into this conformation.

The exponent α was fitted for chloroform and cyclohexane and found to be 0.60[1] and 0.52 respectively, which is in agreement with expected values (0.4-0.7).

The thickness as a function of the concentration c was also expected to follow a power law

$$t \propto c^{\beta} \tag{4.2}$$

[1] There was only performed one measurement for each sample, hence the corresponding error in the fit has been omitted.

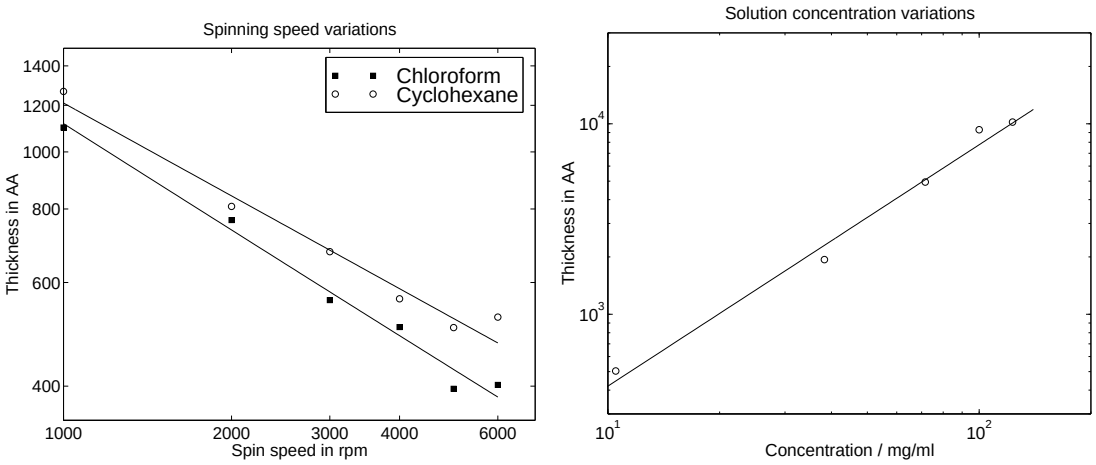

(a) Thickness vs spinning speed usingCCl_3H and C_6H_{12} as solvents.

(b) Thickness vs. polymer concentration.

Figure 4.4: Thickness measurement for spin casting.

where the exponent β was found to be 1.27, which is in agreement with other experiments [39]. The magnitude of the exponent can be justified with the following considerations. If the concentration is doubled, the amount of polymer is doubled, hence the thickness should double corresponding to $\beta = 1$. At higher concentrations the degree of entanglement is expected to increase, hence the viscosity is higher. Consequently less polymer will be "thrown off" during the spin casting, which would leave a thicker film corresponding to a larger exponent, $\beta > 1$.

Speed [rpm]	1000	2000	3000	4000	5000	6000
Thickness [Å]	1100	766	560	504	396	402

Table 4.1: Thickness measurements for different spin speeds. Polymer used: PS-PDMS 10 mg/ml in CCl_3H

Concentration [mg/ml]	10.5	38.3	71.6	100	123
Thickness [Å]	504	1936	4945	9300	10213

Table 4.2: Thickness measured as a function of the polymer concentration. Polymer used: PS-PDMS at 5000 rpm in CCl_3H

Speed [rpm]	1000	2000	3000	4000	5000	6000
Thickness [Å]	1267	808	677	563	503	528

Table 4.3: Thickness measured as a function of the spin speed for cyclohexane as solvent. Polymer used: PS-PDMS 10 mg/ml in C_6H_{12}.

Solvent	Boiling point / °C	Viscosity / centipoises
Chloroform	61.7	0.66
Cyclohexane	80.7	0.58

Table 4.4: Solvent characteristics. The viscosity is tabulated for T =20°C [40].

4.2 Bulk Samples

The bulk samples were made for the small angle x-ray and neutron scattering experiments. The difference in appearance of the two polymers can be seen in figure 4.5. The PS-PDMS block copolymer is a white powder at room temperature, whereas PEP-PDMS is a transparent melt. In the SAXS experiment,

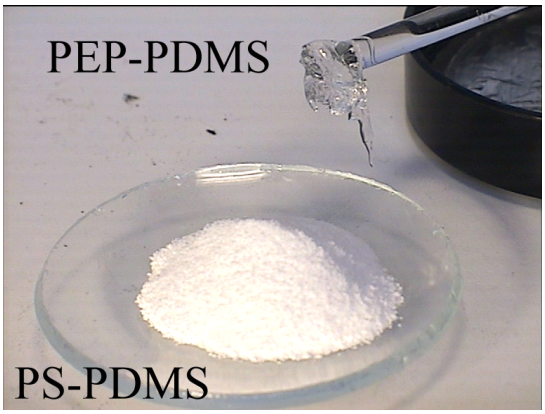

Figure 4.5: Difference in appearance for the two polymers.

the PS-PDMS powder was placed between two Kapton windows, whereas the PEP-PDMS was merely smeared on the Kapton in a sandwich. The thickness of the samples was approx. 0.5 mm, which gives a suitable signal without too much absorption. This has to be considered for x-ray, which has a limited penetration power In the SANS experiment the PEP-PDMS was again prepared in a sandwich but with aluminum as windows. Bulk samples of PS-PDMS were prepared in three different ways:

Pressed pill. The powder was pressed into a 1 mm thick pill.

Solvent cast. The polymer was dissolved in chloroform and left to evaporate on aluminum foil.

Melted. The powder was heated to 200°C and then squeezed between two pieces of aluminum.

The multiple PS-PDMS bulk samples were made because they showed different scattering images (see chapt. 5). The thickness of the samples varied from a few microns (solvent cast) to 1 mm for the pill.

Chapter 5

PS-PDMS

The experimental work on the two model systems has been split into two separate chapters, because they show distinctly different structural behaviors. This chapter covers PS-PDMS while chapter 6 deals with PEP-PDMS.

The idea at the beginning of the project was to study the structural development of the lamella structure in a diblock copolymer. PS-PDMS was chosen because it was already studied [10], and the high glass transition temperature for the PS-block would allow for freezing the structure. The previous study [10] characterized the surface and the outermost 100 Å. Using reflectivity, a detailed profile perpendicular to the surface of the entire film could be measured.

5.1 X-ray Reflectivity

The idea was to start with x-ray reflectometry to gain insight into reflectivity studies.

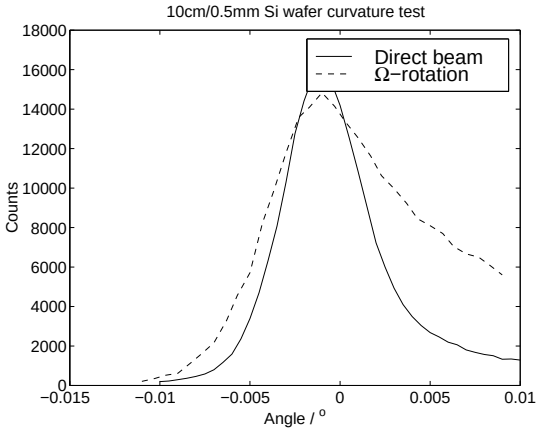

(a) Macroscopic curvature measurement of a large silicon wafer. The direct beam is compared to a Ω-scan performed around $\Omega = 0.1414^{o}$. The tail at positive angle is an alignment error.

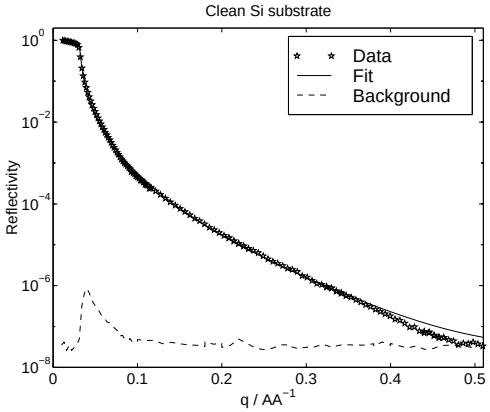

(b) X-ray reflectivity curve of a silicon substrate. The fitted curve has been resolution smeared and a background level of $3 \cdot 10^{-8}$ has been added. The background (– – –) is plotted to show that background subtraction is redundant. The background level is several orders of magnitude lower than the signal for most of the curve.

Figure 5.1: (a) The macroscopic curvature of the substrate was tested by rocking the sample and (b) the roughness measured by reflectivity.

A clean 10 cm in diameter silicon substrate (0.5 mm thick) was measured to test the quality of the substrate, i.e. roughness and macroscopic curvature. The substrate was not cleaned in Piranha solution prior to the measurements.

	Scattering density / Å^{-2}	Absorption length / Å^{-1}	Thickness / Å	Roughness / Å
Fit	$1.95 \pm 0.01 \cdot 10^{-5}$	$2.6 \pm 0.7 \cdot 10^{-6}$	∞	2.6±0.3
Calc.	$1.97 \cdot 10^{-5}$	$1.44 \cdot 10^{-6}$	∞	

Table 5.1: Fitted parameters for the silicon substrate compared with calculated values.

The macroscopic curvature measurement is shown in figure 5.1(a). The curvature can be estimated from the width of the Ω-scan compared to the direct beam [41]. As seen in the figure, the width of the Ω-scan is fully comparable to the width of the direct beam, hence the use of thicker substrates is not necessary. The tail at positive angles stems from an alignment error and does not influence the result. The fitted roughness of the substrate was found to be 2.8 Å.

The first film was spin casted from conditions similar to conditions used by Flarup [10]. The film was casted from a 10 mg/ml solution with a spin speed of 5000 rpm for 30 sec. The resulting reflectivity curve is shown in figure 5.2(a). The fitted curve corresponds to one layer with the average scattering length of the two polymers. Including two layers does not change the fitted reflectivity curve. Consequently only one layer with the averaged scattering density was used.

	Scattering density / Å^{-2}	Absorption length / Å^{-1}	Thickness / Å	Roughness / Å
Layer	$9.6 \pm 0.2 \cdot 10^{-6}$	$2.1 \pm 0.9 \cdot 10^{-7}$	477.9±0.6	12.0±0.5
Substrate	$1.90 \pm 0.01 \cdot 10^{-5}$	$1.2 \pm 0.5 \cdot 10^{-6}$	∞	2.1±0.1
Layer	$9.19 \cdot 10^{-6}$	$5.50 \cdot 10^{-8}$		
Substrate	$1.97 \cdot 10^{-5}$	$1.44 \cdot 10^{-6}$	∞	

Table 5.2: Fit parameters for the thin film.

In order to achieve a clearer signal from a stratified structure, i.e. distinct Bragg peaks, a thick film was made from a 100 mg/ml solution. Prior to the measurements the thickness was estimated from Flarup [10] to be approx. 1000 nm. At this time the thickness calibrations described in section 4.1.4 were not performed. The first reflectivity curve from the thicker film is shown in figure 5.2(b).

As can be seen from the figure, the Kiessig fringes arising from the thickness are suppressed by the resolution. In order to resolve the thickness, an analyzer crystal was inserted. The reflectivity curve is shown in figure 5.3(a). The curve could not be described completely by a single layer with an averaged scattering density and there are no distinct features in the curve except for the thickness oscillations. The data are noisy and determination of the fringes separation is difficult. However, a Fourier transform gives the characteristic period for the oscillations.

In figure 5.3(c) the reflectivity has been multiplied with the scattering vector to the fourth power. The vertical part of the curve (0.045 Å$< q <$0.055 Å) has been Fourier transformed and the result is shown to the right. The peak[1] is relatively weak due to noise in the experiment. The position of the peak was found to be $1.07 \cdot 10^4$ Å, which is in agreement with the thickness measured by Flarup [10].

The reflectivity profiles so far have not shown a distinct order in the films. The thick film was then annealed in a vacuum oven at 170°C for a week and measured by x-ray reflectivity again. The reflectivity curve from the annealed film was identical to the non-annealed film.

From those measurements it was not possible to proceed with the intended experiments, hence a new polymer system with better contrast and mobility was desirable.

[1] The other oscillations in the Fourier transform is a result of the boundary conditions.

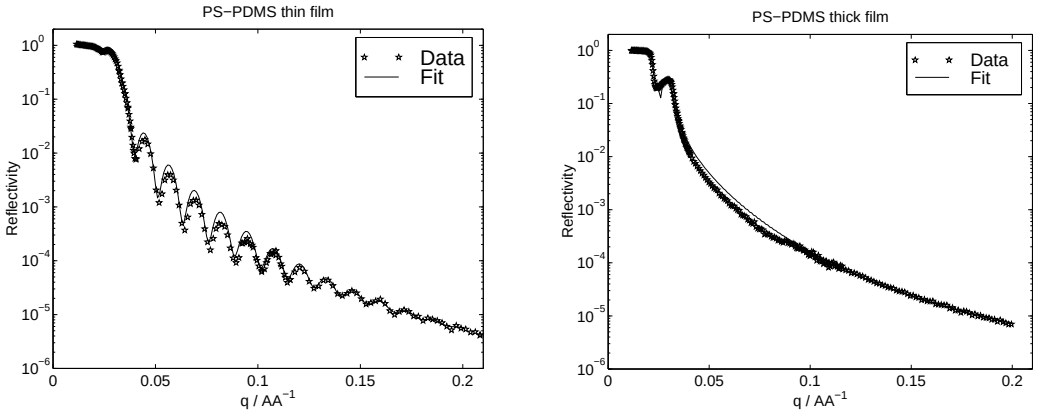

(a) X-ray reflectivity curve of a thin PS-PDMS film. The fitted curve has been resolution smeared and a background level of $1 \cdot 10^{-6}$ has been added.

(b) X-ray reflectivity curve of the thick PS-PDMS film. The fitted curve has been resolution smeared and a background level of $2 \cdot 10^{-6}$ has been added.

Figure 5.2: X-ray reflectivity of a thick (a) and a thin (b) PS-PDMS film.

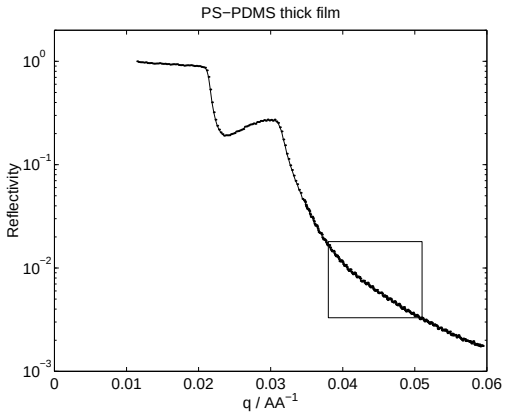

(a) Reflectivity curve of the thick PS-PDMS film measured with an analyzer crystal to increase the resolution.

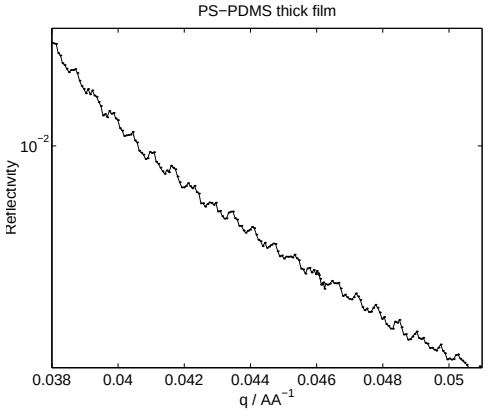

(b) A closer view of the section marked in the figure to the left.

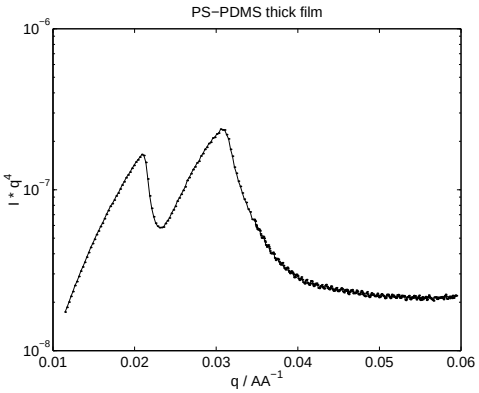

(c) The corrected reflectivity curve.

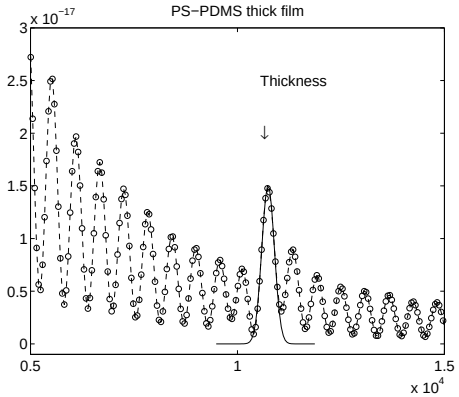

(d) The result of the Fourier transform. The position of the characteristic peak has been fitted with a Gaussian.

Figure 5.3: Thickness determination of a thick PS-PDMS film by Fourier transform.

5.2 Small Angle X-ray Scattering

From the measurement of the thick film it was believed that the x-ray contrast between the two polymer blocks was too weak. The quickest way to test this was a measurement of the bulk block copolymer. Using SAXS would give the lamella period in the polymer, provided sufficient contrast is present between the blocks. The period is essential in the construction of the film profile in the analysis of the reflectivity curve.

The powder was placed in a 1.0 mm brass spacer between two Kapton windows, and the sample was irradiated for several hours. The scattering image is shown in figure 5.4 with the corresponding azimuthal mean. The scattering image has not been background corrected. A background measurement did not show different characteristics from the sample, except from the grain scattering which can be seen at very low q, close to the beamstop.

The broad peak at $q \sim 0.4$ Å arise from Kapton. As can be seen, the scattering picture is only showing a very weak shoulder at approx. 0.05 $Å^{-1}$, hence the x-ray contrast was too weak for further x-ray experiments.

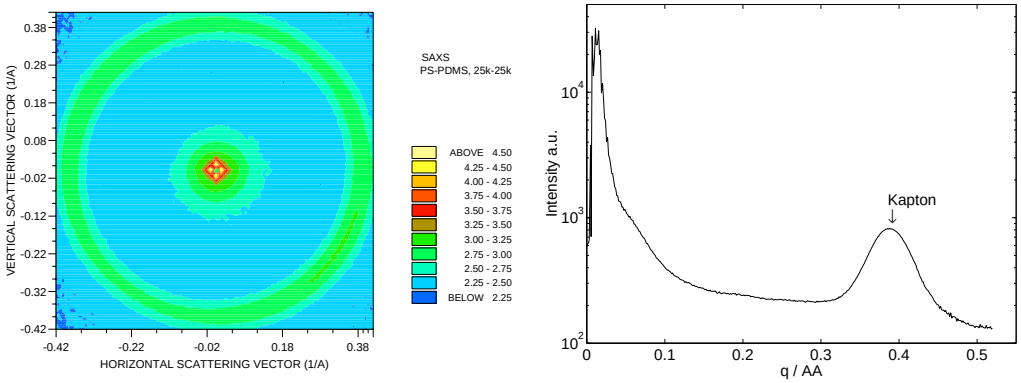

(a) SAXS scattering image of PS-PDMS.

(b) Azimuthally mean of the scattering image.

Figure 5.4: Small angle x-ray scattering image of bulk PS-PDMS.

5.3 Small Angle Neutron Scattering

Since the scattering density for neutrons depends on the nuclei rather than the electron density, it might be quite different from that observed using x-rays. For that reason, small angle neutron scattering was used to measure the lamella period in the bulk.

Three different samples were made: solvent casted film where the solvent was allowed to evaporate, a pressed pill, and melted sample where the powder was heated to 200°C and then squeezed between two aluminum plates. It was very difficult to melt the polymer. The material became softer but never flowed as expected.

The scattering images are shown in figure 5.5. The images and the peak positions vary from method to method. The peak positions for the melt, solvent and pill have been fitted by Gaussians: 0.01687 ± 0.0001 $Å^{-1}$, 0.01547 ± 0.00008 $Å^{-1}$, 0.01258 ± 0.00001 $Å^{-1}$ respectively, which corresponds to a period of 499±5 Å, 406±2 Åand 372±3 Å. For the melt the third order Bragg peak can also be seen at 0.03836 ± 0.0001 $Å^{-1}$ corresponding to a period of 491±2 Å.

The thin films measured by x-ray reflectivity were also measured by SANS. They were aligned with the surface parallel to the incident beam. This setup allows not only for measuring the out-of-plane

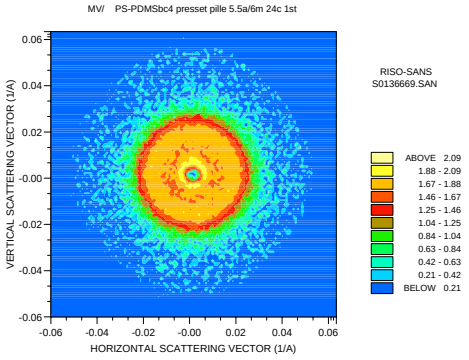

(a) Pressed pill of PS-PDMS.

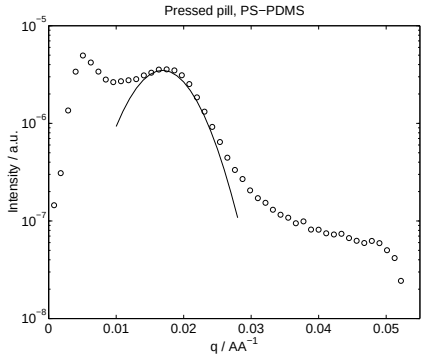

(b) Azimuthal mean.

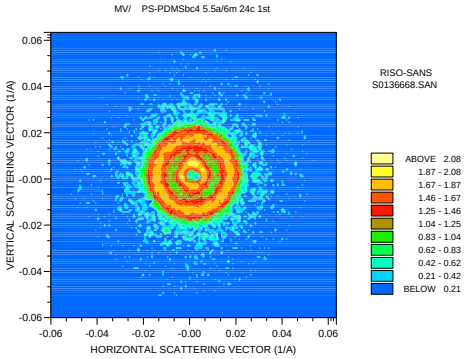

(c) Solvent cast sample of PS-PDMS.

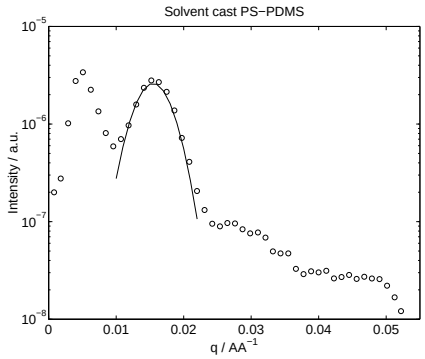

(d) Azimuthal mean.

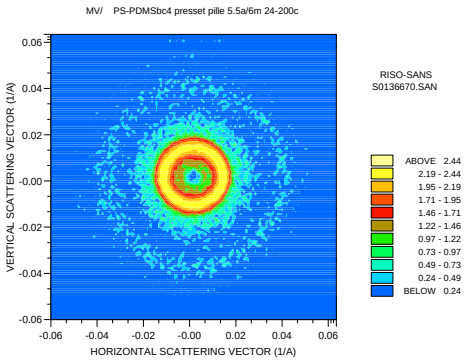

(e) PS-PDMS melt at 200°C.

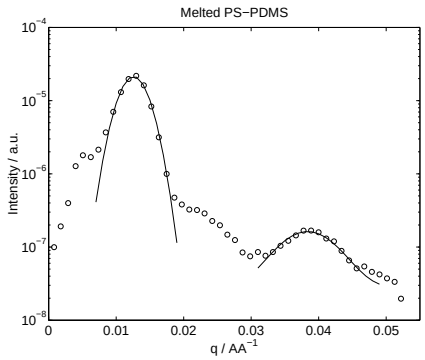

(f) Azimuthal mean.

Figure 5.5: SANS images of bulk PS-PDMS.

scattering as by reflectivity, but also the in-plane component.

In figure 5.6, the resulting scattering image of the thin film is shown, which differs from what was expected. A perfectly ordered lamella would only give rise to two Bragg peaks and not an ellipse. The question is: what is the structure in the film and how does its size compare to what was measured in the bulk? The transformed structure in real space is also an ellipse. Due to the rotational symmetry from the spin casting process the three dimensional structure must be a disc with the largest dimension along the substrate and the rotational symmetry along the surface normal. The mean has been taken in a horizontal and vertical band across the detector. The peak positions has been fitted by Gaussians to 0.02344 ± 0.0004 Å^{-1} and 0.01598 ± 0.0008 Å^{-1} corresponding to 268±4 Å and 393±18 Å for the horizontal and vertical component respectively.

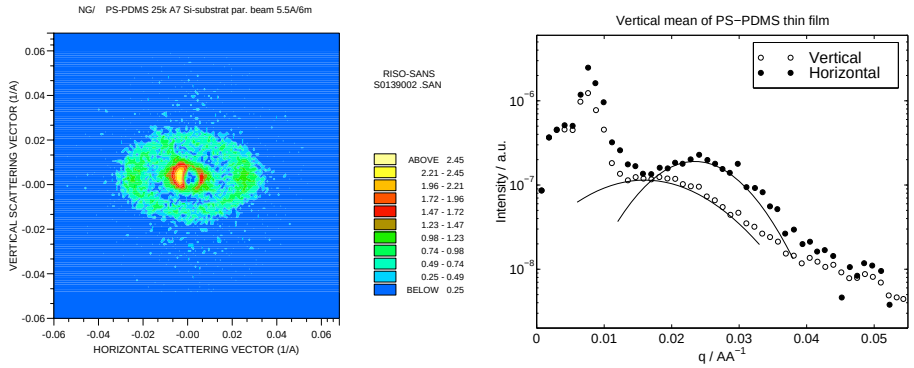

(a) SANS scattering image of PS-PDMS thin film.

(b) Azimuthal mean.

Figure 5.6: SANS of PS-PDMS thin film.

Comparing the thin film peak positions with the bulk, the horizontal period is comparable to the solvent cast and pill samples. Why do the bulk samples differ and which can be trusted? Both the pill and the solvent cast film were made at ambient conditions, whereas the melt was made at 200°C. The vertical mean in the thin film is comparable with the pill and the solvent cast bulk samples. *Assuming* the solvent cast sample is in thermodynamical equilibrium, the thin film measurement could indicate that the lamellae might be ordered out-of-plane as well as in-plane but with different periods.

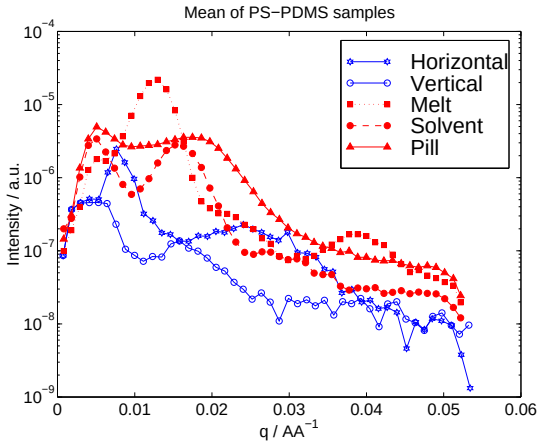

Figure 5.7: The azimuthal mean of the thin film compared to the bulk samples.

In figure 5.7, the azimuthal means are compared for different samples. The origin of the disc structure

is a combination of normal behavior of symmetric block copolymers, where they will order parallel to the substrate, and a preferential orientation induced by the radial flow during spin casting. The high χN value at room temperature (χN =201) "freezes" that orientation. The annealed sample was also measured by SANS but the scattering image did not differ from the non-annealed, similarly to the results from the x-ray measurement.

5.4 Neutron Reflectivity

Despite the non-equilibrium structure found in the SANS measurement, a neutron reflectivity measurement was performed. The neutron reflectivity, however, showed suitable contrast to see a faint Bragg peak. The resulting curve is shown in figure 5.8. There is a weak bump at 0.0252 ± 0.0003 Å^{-1} corresponding to 249 ± 2 Å. As expected this period is similar to the horizontal peak position in the SANS experiment. Unfortunately the in-plane component, seen by SANS, is impossible to measure by specular reflectivity.

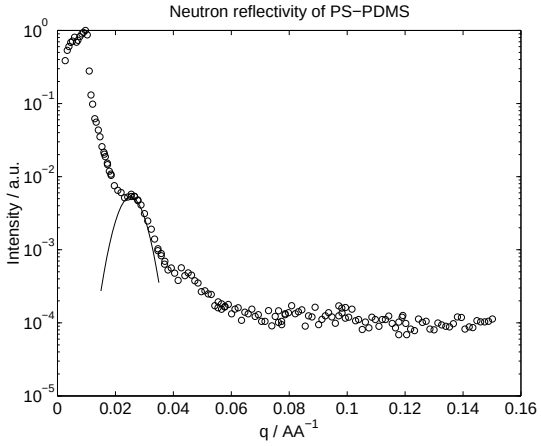

Figure 5.8: Neutron reflectivity of PS-PDMS thin film.

5.5 Atomic Force Microscopy

The topography of the surface of the PS-PDMS sample can be visualized and measured by AFM. The images in figure 5.9 clearly indicate that the film is not perfectly ordered as was seen in the SANS measurement. The phase image has been added for higher magnifications to illustrate the changes in the phase. The AFM was operated in tapping mode. Tapping mode is used, because the forces applied in this mode are much lower than in contact mode. In contact mode the tip is in contact with the surface throughout the experiment, whereas in tapping mode the cantilever is oscillating and only touching the surface once in each cycle. This mode eliminates shear forces which can damage soft samples and reduce image resolution. The phase shift from the induced oscillations in the cantilever is correlated to the sticking of the tip to the surface. The change in sticking might be interpreted as changes in the surface composition, since the blocks differ mechanically.

In the 1x1μm phase image it can clearly be seen that there are changes in the phase, which most likely are variations in the composition, since the change in phase occurs at areas of approx. the same height.

From the 1x1 μm phase image, the "coral" structure might explain the SANS scattering image. The thin film is evidently not in thermodynamical equilibrium with lamellar ordering along the surface normal, hence giving rise to an in-plane scattering component in the scattering image.

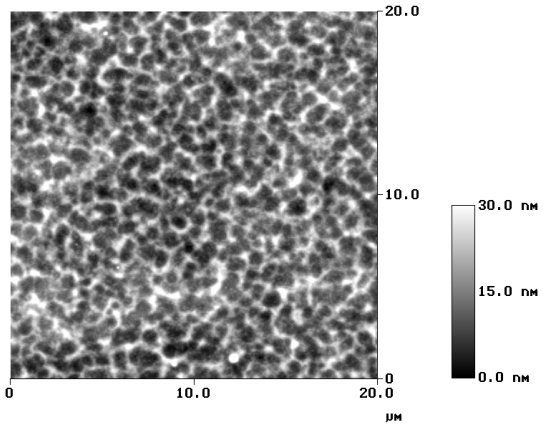

(a) PS-PDMS surface 20x20 μm.

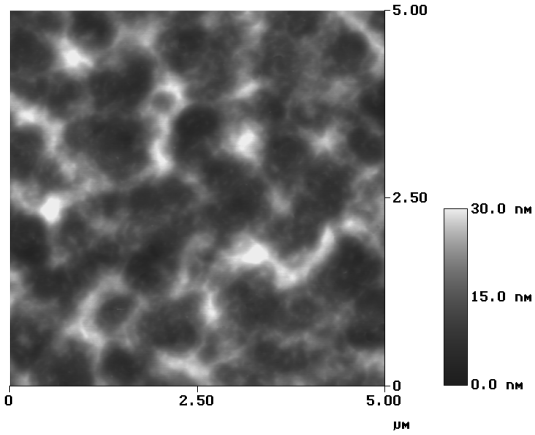

(b) Morphology of surface 5x5 μm.

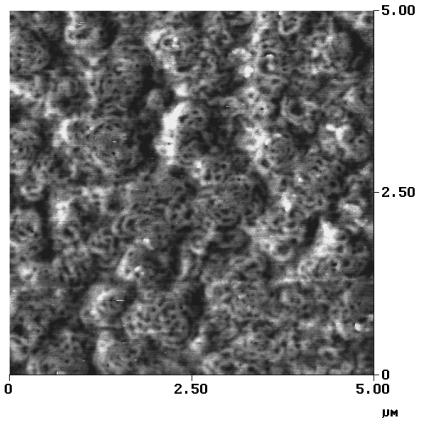

(c) Phase image 5x5 μm.

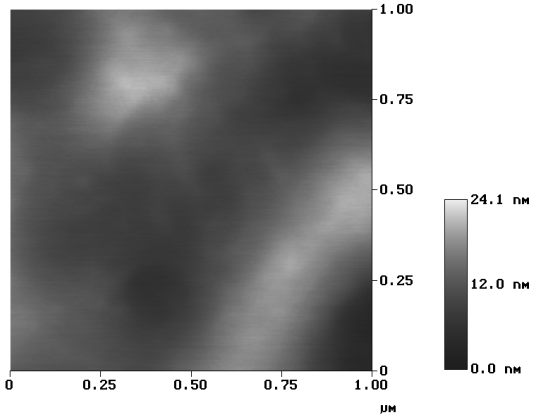

(d) Morphology of surface 1x1 μm.

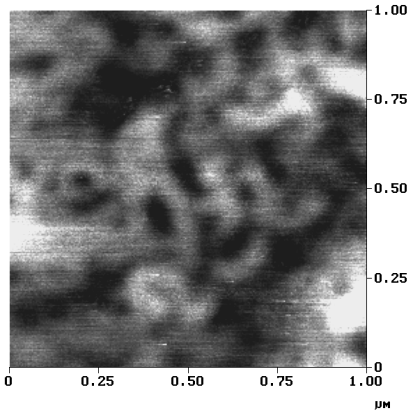

(e) Phase image 1x1 μm.

Figure 5.9: AFM images of the PS-PDMS surface.

Chapter 6

PEP-PDMS

In this second part of the results, the model system was changed to PEP-PDMS. This system has both good neutron and x-ray contrast [1]. The low glass transition temperatures ($T_g^{\mathrm{PEP}} = -56^{\mathrm{o}}\mathrm{C}$ and $T_g^{\mathrm{PEP}} = -127^{\mathrm{o}}\mathrm{C}$) together with the lower molecular weight (4.4k-4.4k) are expected to make the system mobile enough to reach thermodynamic stable structures. However, the structure will be difficult to "freeze" as was intended with the previous model system.

This chapter is divided into three parts. The first part is an investigation of the polymer system using x-rays, for small angle scattering and reflectivity, where the contrast, ordering and lamellar periodicity is investigated. The second part covers a more thorough investigation of the structure using neutron reflectivity and small angle scattering combined with XPS. The last part includes temperature measurements of the structure measured by SANS and neutron reflectivity. An attempt was also made in measuring the lamellar period by AFM as a function of temperature. A heatstage was designed and machined for that purpose.

6.1 Small Angle X-ray Scattering

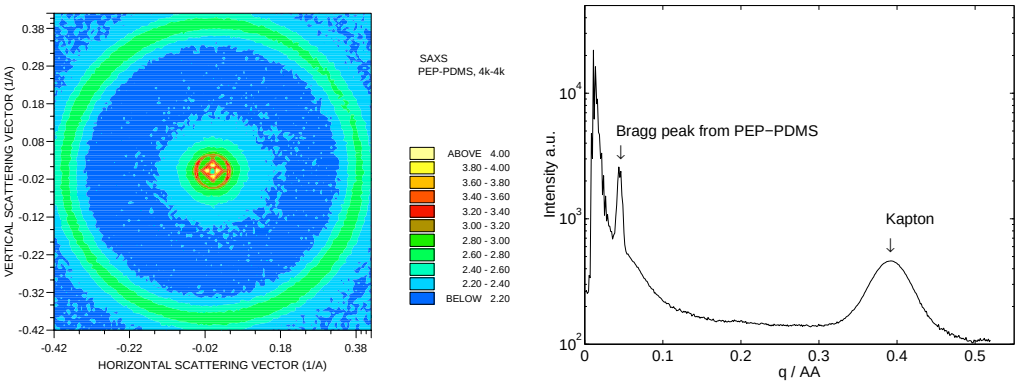

(a) Scattering image of PEP-PDMS.

(b) Corresponding azimuthal mean.

Figure 6.1: SAXS measurement of PEP-PDMS.

The improved x-ray contrast made it possible to measure the lamellar period by SAXS. The polymer melt was placed between two Kapton windows and the resulting scattering image is shown in figure

6.1. The Bragg peak from the lamella ordering is quite evident at 0.0444 ± 0.0002 Å corresponding to a lamellar period of 141 ± 1 Å. The scattering image was not background corrected.

6.2 X-ray Reflectivity

A thin film was spin casted using similar conditions (12 mg/ml solution on a Piranha cleaned substrate, spun at 4000 rpm for 30 sec.) as for the thin PS-PDMS under the assumption that change of polymer system would not alter the thickness significantly. The new film was measured both with and without an analyzer crystal. The resulting x-ray reflectivity curves are shown in figure 6.2.

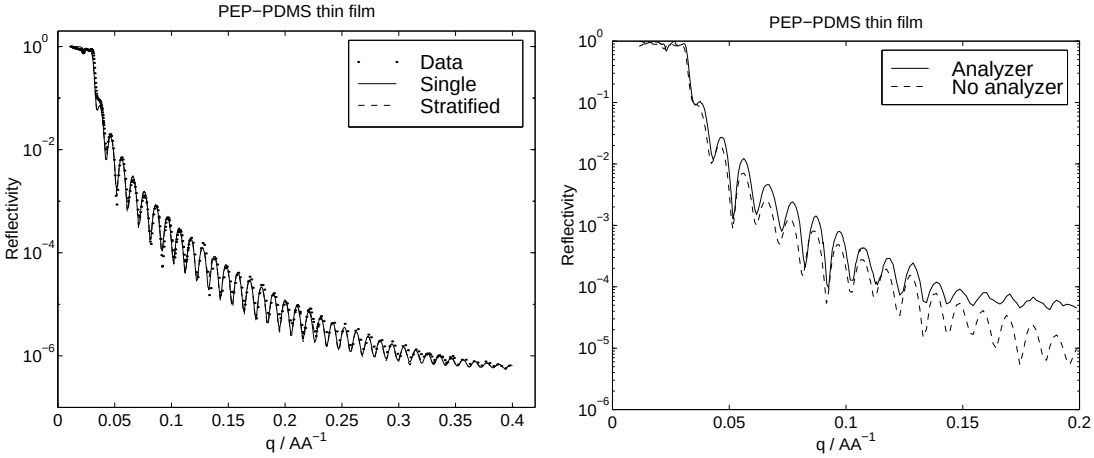

(a) Data (· · ·) measured without an analyzer crystal. Two models, one with a single layer and one with several layers, have been simulated to fit the data.

(b) Measured data with and without an analyzer crystal are compared. The background level increases as the flux is reduced by the analyzer crystal. However, the resolution is improved, which can be seen from the depth of the fringes.

Figure 6.2: X-ray reflectivity of thin PEP-PDMS film.

	Scattering density / Å^{-2}	Absorption length / Å^{-1}	Thickness / Å	Roughness / Å
Layer	$8.95 \cdot 10^{-6}$	$4.74 \cdot 10^{-8}$	600	2
Substrate	$1.97 \cdot 10^{-5}$	$1.44 \cdot 10^{-6}$	∞	2

Table 6.1: Model parameters for the thin film.

The reflectivity curves have been simulated both as a single layer with the average scattering length of the two blocks, and as the expected lamellar structure. The expected structure is reconstructed from the lamella period found in the SAXS experiment. The thickness of the film was easily found from the Kiessig fringes. The film thickness is then divided into a suitable number of periods, where the free interface has been set to be PDMS and the substrate interface to be PEP from an energetic point of view. As can be seen the two models are identical and no clear Bragg peaks can be identified.

To observe the Bragg peaks, a thicker film was prepared from a concentration of 70 mg/ml at a spin speed of 4000 rpm for 30 sec. A concentration below 100 mg/ml was chosen to avoid the use of the analyzer crystal to resolve the thickness fringes. The reflectivity curve from the new film is seen in figure 6.3. The reflectivity curve was measured without an analyzer crystal.

The Bragg peak now becomes visible but the curve is difficult to reconstruct due to the many layers. The thickness was found to be 3900 Å from the Fourier transform, which corresponds to 27.7 bilayers. The model has not been fitted to the data because of the large number of parameters: 55

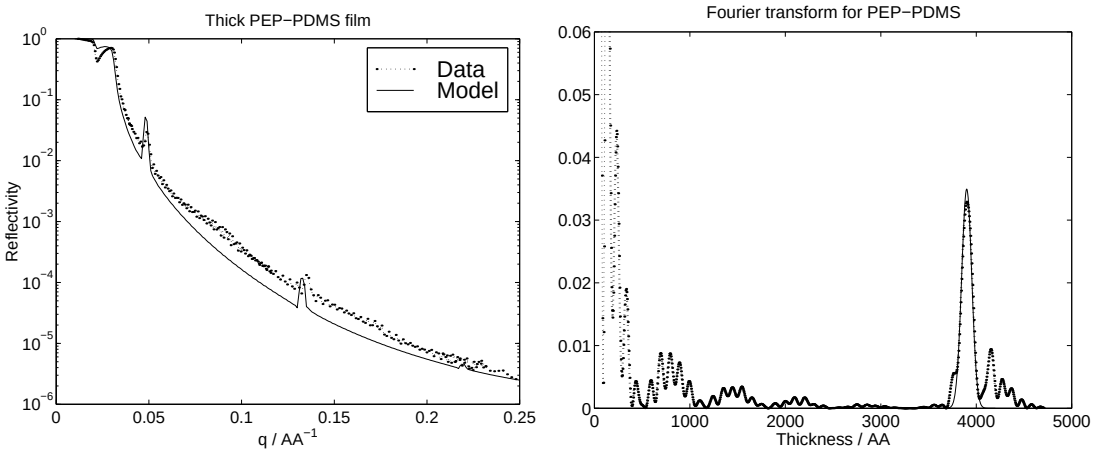

(a) Reflectivity curve of the thick PEP-PDMS film.

(b) Fourier transform of the reflectivity curve to determine the thickness of the film.

Figure 6.3: X-ray reflectivity of thick PEP-PDMS film.

scattering lengths, 55 absorption lengths, 54 thickness, 55 roughness and a background. Resulting in 220 parameters. This can, however, be dramatically reduced by fixing related parameters. This will be explained in more detail in the structure analysis section.

The thick PEP-PDMS films was analyzed at beamline BW2 at Hasylab, Hamburg by high intensity synchrotron x-ray reflectivity. Unfortunately, the sample was damaged by the very intense radiation. This can be seen in figure 6.4. The intention was to obtain a high resolution reflectivity curve over a larger dynamical range than accessible at the rotating anode. As the film was destroyed no usable data were obtained.

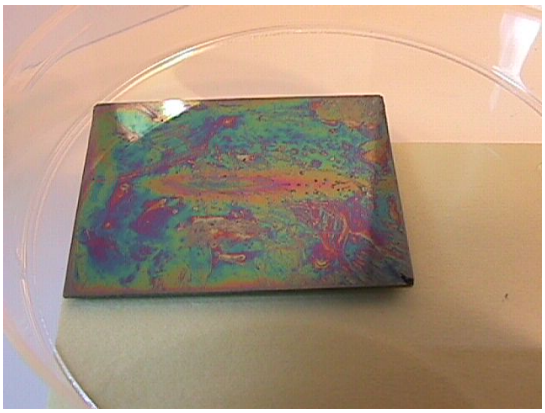

Figure 6.4: The high intensity from the synchrotron has clearly left a damaged trace in the film.

6.3 Thin Film Structure of PEP-PDMS

The first neutron reflectivity experiments examined the contrast and structure at ambient conditions for different thicknesses of the films. The x-ray experiments showed that the films were ordered at ambient conditions just after sample preparation.

Two samples were prepared for neutron reflectivity, one from a 7.6 mg/ml concentration and one from a 12 mg/ml concentration, both spin casted on cleaned substrates at 4000 rpm in 30 sec. The resulting curves are shown in figure 6.5.

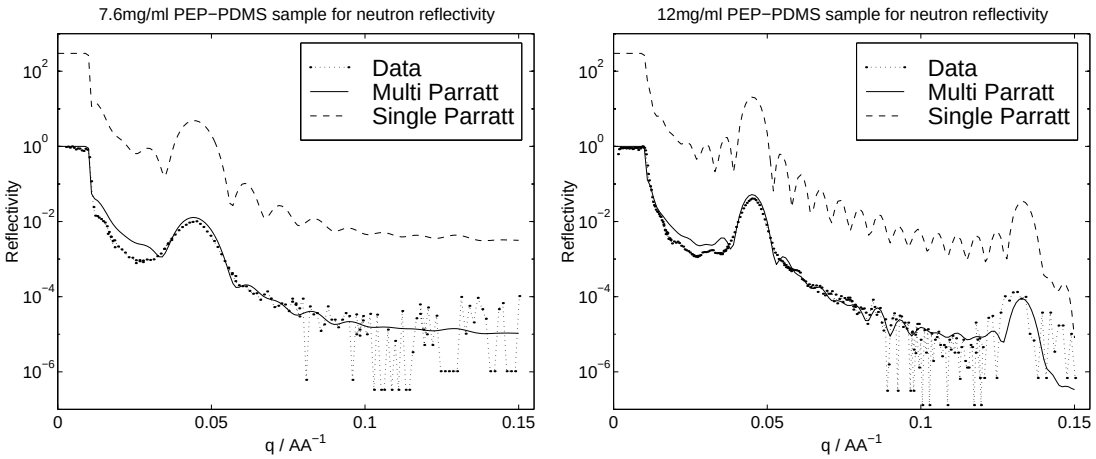

(a) Reflectivity curve for 7.6 mg/ml sample with simulated profile. A background level of $1 \cdot 10^{-5}$ has been added.

(b) Reflectivity curve for the 12 mg/ml sample and the simulated curve.

Figure 6.5: Neutron reflectivity curves for PEP-PDMS and the corresponding model curve. The model curves have been resolution smeared.

The thickness of the films can not be seen directly, since the Kiessig fringes are suppressed. The model reconstruction for the 7.6 mg/ml sample is the average of the sum of two Parratt functions with six and eight boxes. The difference in thickness from the different functions will suppress the Kiessig fringes. For comparison a single Parratt function is plotted where the fringes are clearly seen. The peak position matches exactly the lamella periodicity measured by SAXS (141 Å). The roughness for the polymer layers has been set to be 18 Å and 11 Å for the 7.6 mg/ml and 12 mg/ml samples, respectively. The substrate roughness was set to be 4 Å (as was measured in the previous chapter). The top layer was chosen to be PDMS due to ots lower surface energy and the layer closest to the substrate was set as PEP, which will be explained in section 6.3.2. The number of boxes has been adjusted to the width of the Bragg peak. This can be seen from the 12 mg/ml sample. This sample is the average of three Parratt functions with 10, 12 and 14 layers. The complexity of the reconstruction makes it virtually impossible to fit the data. The origin of several Parratt functions is the morphology of the film. Optical and AFM images of the surface reveal holes in surface. Such holes give rise to variation in thickness.

Optical images (see figure 6.6(b)) clearly indicate that the surface is divided into areas with different thickness. The change in color is a change in the thickness of the film. This effect can especially be seen in the color image, where the change in color is abrupt and not smooth. This is a beautiful indication of the layering of the block copolymer.

An AFM surface image (figure 6.6(d)) clearly illustrates that holes are not smooth but divided into plateaus with a spacing comparable to what is measured by SAXS and NR.

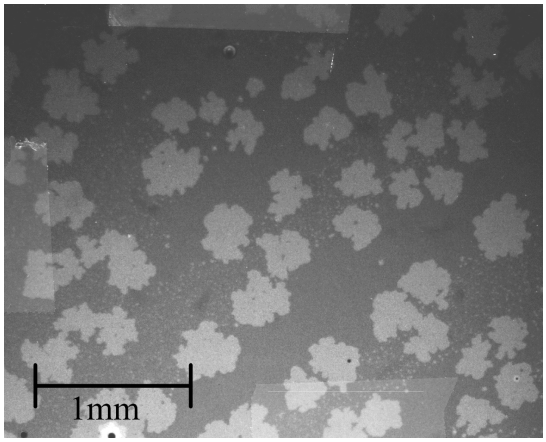

(a) Optical image of a newly prepared film.

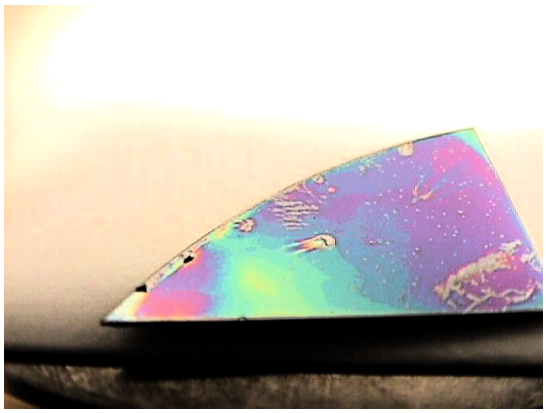

(b) Optical image of an older film.

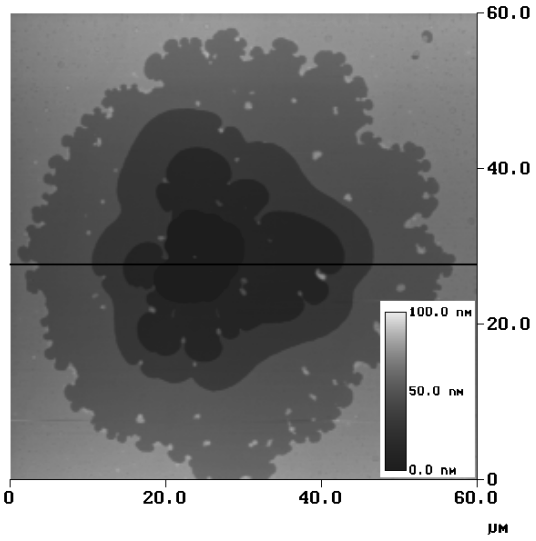

(c) AFM of a hole in the surface of the film.

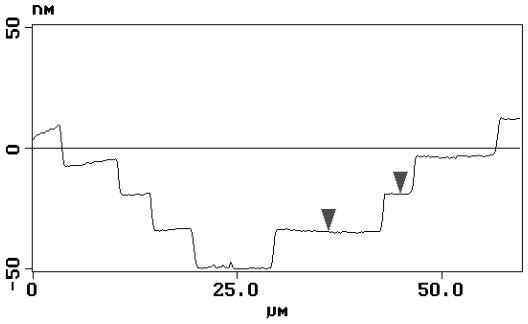

(d) Cross-section of the hole marked by the black line in the figure to the left.

Figure 6.6: Optical and AFM image of the surface.

6.3.1 XPS Measurements

Another sample was prepared with the hope that the film could be described by a single Parratt function. Neutron reflectivity cannot determine if the top layer is PEP or PDMS, because the scattering density of PDMS is virtually zero. The surface energy for PEP is higher than for PDMS (see appendix C.5), hence a measurement of the surface energy might give the composition of the atomic top layer.

It is expected that the outermost layer collapses to approx. half the thickness of the interior layers (see figure 6.7). The reason for this collapse can be explained by the void space left in the top and

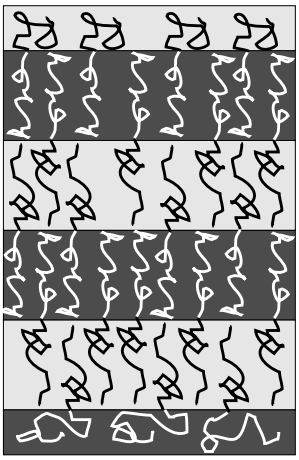

Figure 6.7: Collapse of top and bottom layers.

innermost layer. As can be seen in the figure the interior interfaces consist of polymers from both sides. This is not possible for the top and bottom layer, and space is left where the polymer chains collapse to fill out the extra space.

As was demonstrated earlier, the contrast in x-ray reflectivity does not allow for determination of the profile of the film. By using a surface specific method, XPS (X-ray Photoelectron Spectroscopy, see eg. [10]), which has a probe depth of 80-100 Å, the composition of the outermost part of the film can be investigated.

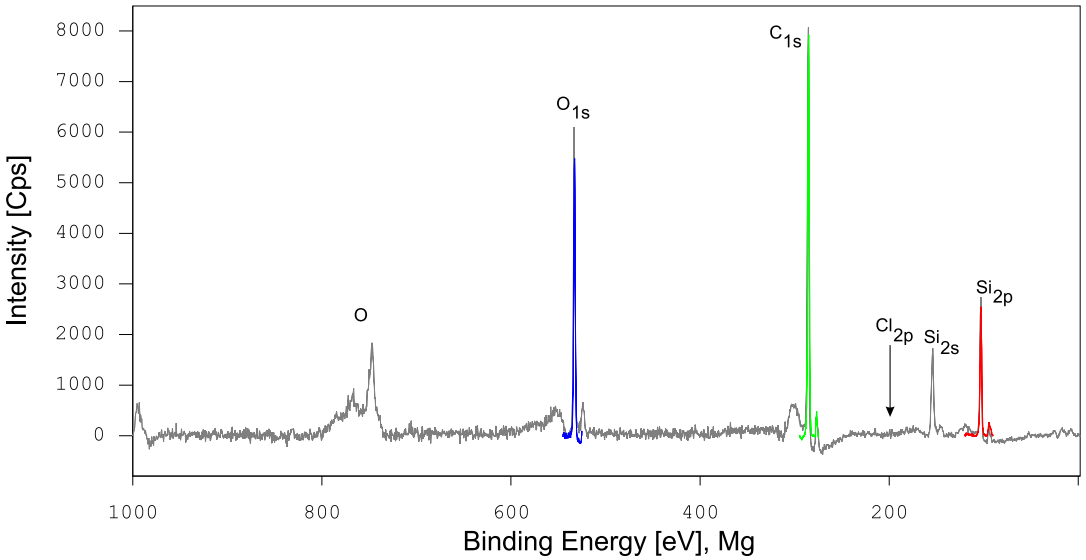

Figure 6.8: XPS overview measurement of a PEP-PDMS thin film.

The measurement of the new sample is shown in figure 6.8. At the same time, the sample was investigated for residual solvent in the film. The missing chlorine signal implies, as expected, that all

Element orbital	O_{1s}	C_{1s}	Cl_{2s}	Cl_{2p}	Si_{2p}
Binding energy / eV	531.69	284.70	270.00	200.00	102.3

Table 6.2: Binding energies for relevant elements in XPS analysis.

solvent had evaporated after spin casting.

Element	C	O	Si
Abundance %	63	18	19

Table 6.3: The relative abundances of the elements in the XPS measurement of the thin PEP-PDMS film.

The abundance of silicon and oxygen is equal, hence the signal must originate from PDMS rather than the siliconoxide on the substrate, where the element ratios are (Si:O) 1:2.

6.3.2 Detailed Structure Analysis

Fitting reflectivity data is far from a trivial task, which is related to the *inverse* problem [35, 42]. Calculating the reflectivity curve from given parameters is called the *direct* problem. The inverse or *inversion* problem consists in determining the profile characteristics from the reflectivity curve. The problem for a general scattering length profile is that the reflectivity data cannot be inverted, since they are merely the moduli of the reflectances. Several solutions are given in the literature [42, 43] to solve this problem.

If general features in the profile are partially known prior to the analysis, simple considerations can ease the reconstruction of the scattering profile. To my knowledge, a detailed description of the analysis of reflectivity data has not been described in the literature. This section will give a detailed description of the considerations for solving the present problem. The task can be outlined in the following points.

Determination of the lamellar thickness. The position of the Bragg peak $q^\star$ is related to the thickness of the lamella $d = 2\pi/q^\star$.

Determination of the phase. The sequence of the layers must be identified. Experimentally, this can be done in the reflectivity measurements provided a suitable contrast exists [14]. Other methods are XPS, contact angle measurements, ellipsometry or SIMS (Secondary Ion Mass Spectroscopy) (see references in [44]). Theoretical considerations involve energetic and conformational considerations of the free energy.

Total thickness determination. The thickness can be determined directly as 2π divided by the distance between two fringes. Alternatively, if the data are noisy, a Fourier transform will give the total film thickness.

Choice of model. The calculation of the reflectivity curve can be done using either dynamical or kinematical theory, bearing in mind that the kinematical model is an approximation as opposed to the exact dynamical theory. The dynamical theory is suitable for a profile that can be described by (few) boxes, whereas the strength for the kinematical theory is in the description of complex changes in the profile.

This analysis is based on the data shown in figure 6.9(a) and 6.9(b) and the dynamical theory is chosen to describe the data.

- The Bragg peak position is found to be 0.0415 $Å^{-1}$ corresponding to a bilayer thickness of 151 Å. One lamella is composed of one PEP and one PDMS layer, hence the thickness of the boxes is 152 Å/2=76 Å. The thickness is equally divided, since a difference between the two blocks would

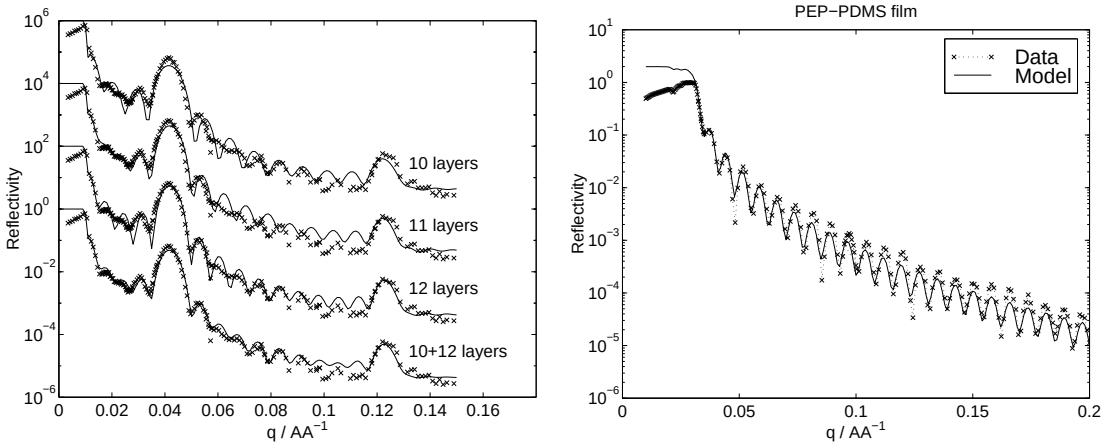

(a) Neutron reflectivity data fitted with different number of boxes.

(b) X-ray reflectivity data for sample modeled with one layer with the average scattering length.

Figure 6.9: Complementary reflectivity measurements of the last PEP-PDMS sample.

result in two first order Bragg peaks. This thickness is slightly higher than what was measured by SAXS. It might be explained by an excess of material, but not enough to complete another layer, hence the excess is distributed evenly between the layers.

- Next step in the analysis is the sequence determination of the layers. In the present case the neutron contrast between vacuum and PDMS is vanishing, hence another method must be applied to determine the surface composition. XPS was used because it allows for a determination of the top 80-100 Å of the film. The three main elements in the block copolymer were measured a higher energy resolution and improved statistics compared to the overview spectrum in figure 6.8. Each peak is integrated and the relative abundance in the material can be found. The film was measured at three different positions: at the center, at the edge and in between. The results were averaged.

  Pure PDMS would give (C%:O%:Si%) 50%:25%:25%, whereas PEP would give 100%:0%:0%. In hydrocarbons the signal decays exponentially with a characteristic length of 25 Å (the mean free path) [45]. From this decay length and the element ratios, it is possible to calculate the thickness of the PDMS layer under the assumption that the surface and layers are homogeneous.

  It was decided to use the carbon signal to calculate the thickness t of the PDMS layer. The signal from the carbon is given as the weighted sum of the carbon content of the two polymer blocks

$$0.63 = 0.5 \int_0^t \frac{e^{-x/25}}{25} dx + 1 \int_t^\infty \frac{e^{-x/25}}{25} dx$$

  This integral equation can be solved and the thickness found to be 34 Å. Assuming PEP was the toplayer and solving the corresponding integral equation a thickness of 8 Å is found, which gives no physical meaning for this system. Hence the surface must be covered with a 34 Å thick PDMS layer. The calculation might as well have been carried out for oxygen or silicon. The bottom layer can be determined from the total thickness.

- Next step will be a determination of the total thickness of the film, i.e. the number of boxes in the model and the bottom layer. X-ray reflectivity (figure 6.9(b)) gives the total thickness of the film from the Kiessig fringes. Fitting the curve with one box with the average scattering length of the two polymer blocks, the thickness is found to be 802 Å. The width of the Bragg peak in the neutron data is also related to the number of layers, or the thickness. Using a least square

fitting program including resolution smearing a number of boxes have been fitted to the data. In figure 6.9(a) three curves with 10,11 and 12 boxes have been fitted to the data with the box width fixed (Bragg peak position). As can be seen 10 boxes give a too broad Bragg peak, whereas 11 and 12 fit the peak width and the position of the nearest fringes equally well. However, at higher scattering angles 12 boxes fit the fringes better. The sum of the layer thickness gives a thickness of 834 Å which is fairly close to what was found in the x-ray reflectivity curve.

Combining the 10 and 12 box curves result in a better fit to the data as can be seen in figure 6.9(a). The amplitude of the fringes fits the data almost perfectly. The curves have been weighted 1/3 and 2/3 for the 10 and 12 box model respectively. The ratio has been estimated from the optical image in figure 6.6(b).

The combined curve has not been fitted, since it requires a special program, which was not at hand and the limited time did not allow for the development of this. Developing such a program is not a trivial task, since careful considerations of parameter reduction must be made.

- The analysis could be performed with less parameters using the kinematical model. Reconstructing the reflectivity curve using the kinematical model might be more illustrative than the dynamical model. To build a compositional profile of the film, a number of error functions are used as the analytical functions to describe the compositional interphase widths. The profile are based on the numbers in table 6.4. All the polymer layers have been set to have the same thickness and the interior bilayers have been fixed to have the same width and scattering densities. The remaining parameters are the thicknesses of the layers at the free surface and at the substrate, and the scattering density and the roughness of the substrate. Through this simplification of the profile, the number of parameters can be reduced from 38 to 9. In this context it should be mentioned that the interior layer thickness is locked from the fact that there is only one Bragg peak, hence the parameters were also reduced in the dynamical description. The reflectivity curve is calculated as the squared Fourier transform of the normalized gradient of the scattering density across the film (eq. 3.44). The result is shown in figure 6.10.

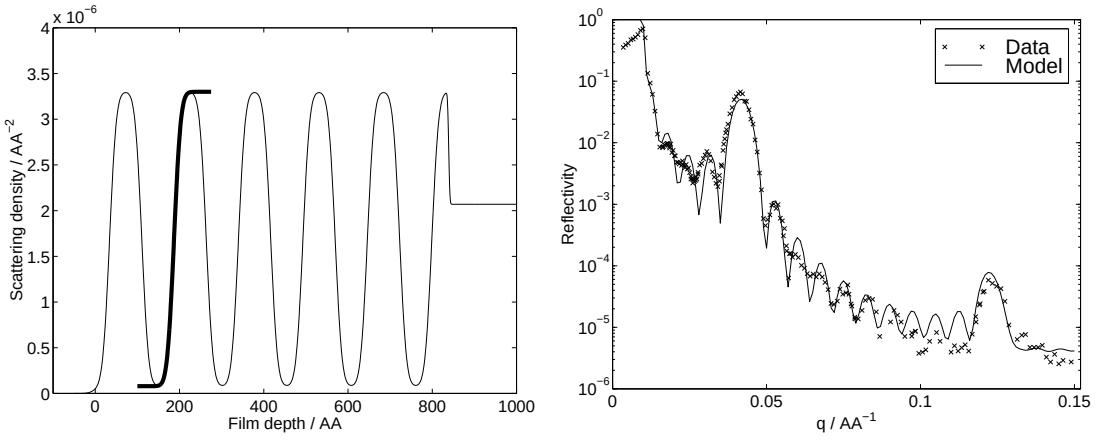

(a) The constructed scattering density profile.

(b) The corresponding resolution smeared reflectivity curve compared with the data.

Figure 6.10: The kinematical theory used to describe the data. The thick line shows the description of the interphasial width.

It should be kept in mind that the dynamical model is exact and the kinematical model is an approximation - though often good.

The resulting parameters for the profile reconstruction is summarized in the the following table.

	Material	Thickness Å	Roughness Å
Top layer	PDMS	34	12
Interior layers	PEP/PDMS	75/75	12/12
Substrate layer	PEP	40	12
Substrate	Silicon	∞	3

Table 6.4: Model parameters for the PEP-PDMS thin film at room temperature.

A thin film sample was mounted with the surface parallel to the incident neutron beam. The resulting image is shown in figure 6.11(a), which clearly indicates perfect ordering of the lamllae normal to the surface as expected [22, 46, 47]. Generally, symmetric block copolymers are ordered at the surface. The micrograph in figure 6.11(b) illustrates this phenomena.

The degree of mosaicity in the PEP-PDMS film can be estimated from the width of one of the Bragg peaks. Fitting a 2D Gaussian to the peak gives a width (FWHM) of ΔQ_y=0.0073 Å^{-1}. This has to be deconvoluted with the instrumental resolution ΔQ_y=0.0049 Å^{-1}. From this an upper limit for the mosaicity in the thin film can be estimated to be 6.6°. It has been assumed that the substrate is perfectly flat and does not contribute to the broadening of the peak.

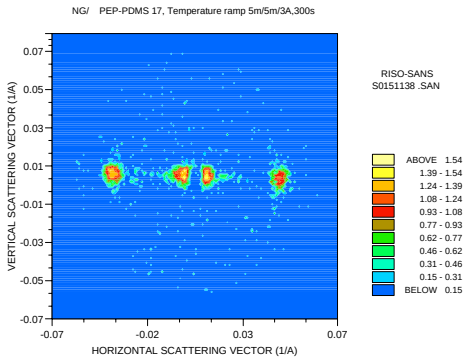

(a) A thin film sample was mounted vertically in the SANS with the surface parallel to in incoming beam. The scattering image clearly shows perfect ordering normal to the surface.

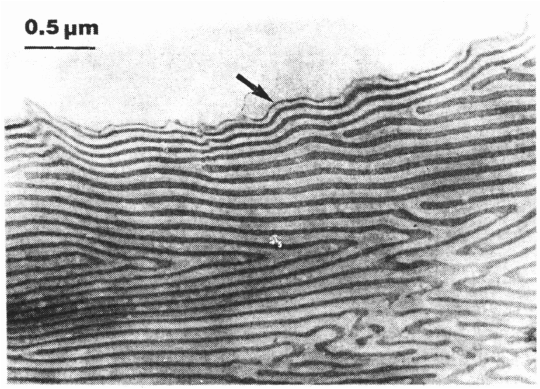

(b) Electron micrograph of PI-PS polymer. The free surface is indicated by the arrow. A closer look at the arrowhead suggests that the surface layer is approx. half the thickness of the interior layers. Adapted from [46].

Figure 6.11: (a) The orientational ordering in the PEP-PDMS thin films measured by SANS. (b) The surface affinity for one of the blocks is illustrated with PI-PS.

6.4 Temperature Dependency Measurements by Neutron Reflectivity

A study of the lamellar structure at different χN-values was the next step in the investigation of the thin film. N could not be varied, since only one polymer was at hand. However, the interaction parameter χ could be changed by the temperature. The intended experiment was to bring the system into the disordered state at $T > T_{ODT} = 165$°C and measure a reflectivity curve in the disordered state. Then bring it back to the ordered state and measure continuously to monitor the ordering of the structure. It quickly turned out that the system was too mobile, hence it reached thermodynamical equilibrium faster than the time for a measurement.

It was hoped that the system could be "trapped" or "frozen" in the disordered state, if the sample was quenched below the glass transition temperature for the PEP-block. The sample and sample holder was heated to 180°C, a reflectivity curve measured to ensure that the film was disordered, and then quenched in liquid nitrogen. The final temperature of approx. -100°C was reached within 5 min. The Bragg peak was measured continuously without background correction to minimize the acquisition time. As can be seen in figure 6.12 the background level is much lower than the signal, hence the background subtraction would not change the peak shape or position. Near the order-disorder transition, the profile is nearly sinusoidal, giving only a first order Bragg peak. As the system gets deeper into the ordered state (higher χN - lower temperature) the interfaces become narrow and almost step-like. A step profile will give rise to higher order Bragg peaks (evident from Fourier considerations).

The sample was mounted in a primitive sample holder, which was filled with nitrogen gas to avoid water vapor and oxygen around the sample as the holder could not be evacuated. Oxygen would oxidize the film when heated and the water would freeze during the quench and it might damage the surface of the sample, furthermore the incoherent scattering from water is significant. The holder was sealed with low temperature grease. Helium would have been first choice for an inert gas since it has high heat transfer, which would ensure low temperature gradients between the sample holder and the sample. However, helium is very volatile and leak proof holders for helium have to be designed carefully. Nitrogen was at hand and easier to handle.

The sample was heated to 176°C and the first order Bragg peak measured to guarantee that the sample was in the disordered state. The sample was then quenched below the glass transition temperature for PEP (-56°C) and the holder was isolated with glass wool to minimize the heating from the surroundings. The first order Bragg peak was measured at a range of temperaures up to room temperature where the sample was transfered to a newly designed computer controlled vacuum oven. The sample was heated to 178°C and the first order Bragg peak measured at a range of temperatures. This new oven was not used for the quenching experiment, since the forces on the aluminum, vacuum seal and electronics are enormous during the quench. To avoid damage of the aluminum, seal and electronics, the old modified sample holder was used.

The resulting temperature curve is shown in figure 6.14. As T_{ODT} is reached the errorbars grow significantly in size and the transition temperature can be estimated to be 155°C, which is lower than what is measured by rheology [1].

For one sample both the first and third order Bragg peaks were measured for a set of different temperatures. The two Bragg peaks were plotted and a stratified film was simulated with a suitable roughness. The roughness is a measure of the interphase width λ, which was compared with the analytical expression given by Semenov [22] $\lambda = \frac{2b}{\sqrt{6\chi}}$, where b is the weighted segment length. The experiment is in good agreement with the theory as can be seen from figure 6.13.

6.5 Temperature Dependency Measurements Performed by SANS

A bulk sample was mounted in an oven where the temperature could be controlled in a constant flow of nitrogen. Before each measurement the sample was allowed to equilibrate to the temperature for 5 min. In the quench experiment, it was shown that the structural arrangement was on a faster timescale than could be observed. The cooling rate in the neutron reflectivity experiment was approx. 60 deg/min whereas in the SANS experiment it was below 1 deg/min, hence a thermodynamically stable structure

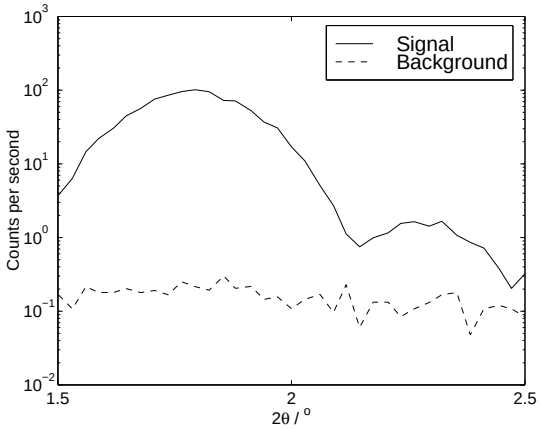

Figure 6.12: The specular signal compared to the background for the first order Bragg peak. The background is one to three orders of magnitude lower than the signal.

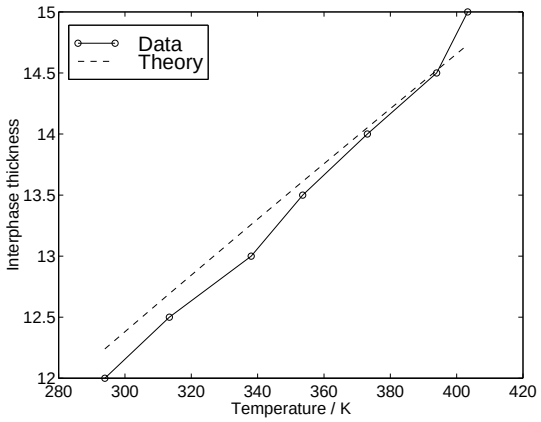

Figure 6.13: Width of the interphase as function of the temperature.

should be reached at this slow heating. The sample was heated into the disordered state, then measured at several temperatures down to -120°C and then back to the disordered state upon heating. As can be seen from figure 6.15(a), the curve completely reproduces. The slope between the disordered state and the crystallization temperature (~ -40°C [48]) was fitted to the scaling relation $D \propto \chi^{\alpha}$. α was found to be 0.221 ± 0.002, which is in perfect agreement with Melenkevitz and Muthukumar [23] scaling expression for a symmetric diblock copolymer in the intermediate segregation region. The temperature curve measured by reflectivity (fig. 6.14) was quenched to the low temperature limit. The shape of the curve could have been a result of the quench. However, the bulk measurement showed that the same shape was found for the bulk system during a low heating and cooling rate.

A thin film was prepared from a 70 mg/ml solution and spin casted with 4000 rpm for 30 sec. The film was aligned in the SANS to measure if the shape was completely independent of the quench for the thin film. The assumed trajectory during the quench is plotted in the figure as a dotted line. The temperature could also be kept constant throughout the experiment for the low temperatures, which was not the case in the reflectivity measurement. The resulting curve is shown in figure 6.15(b). Again the curve was fitted to the scaling expression and the scaling parameter was found to be $\alpha = 0.225 \pm 0.002$, which is in perfect agreement with both the previous reflectivity measurement, the bulk sample and the theory.

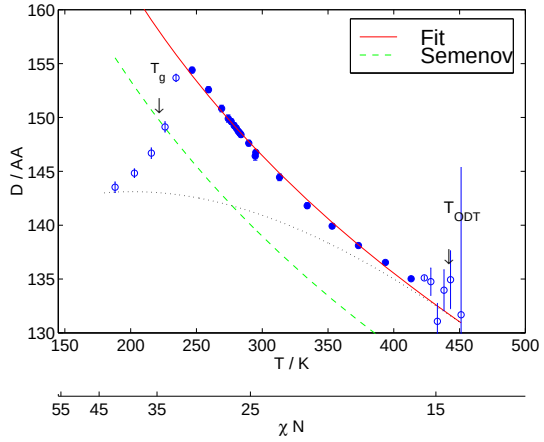

Figure 6.14: The lamella period measured by reflectivity as a function the temperature. The dotted line represents the assumed trajectory of the lamella period during the quench.

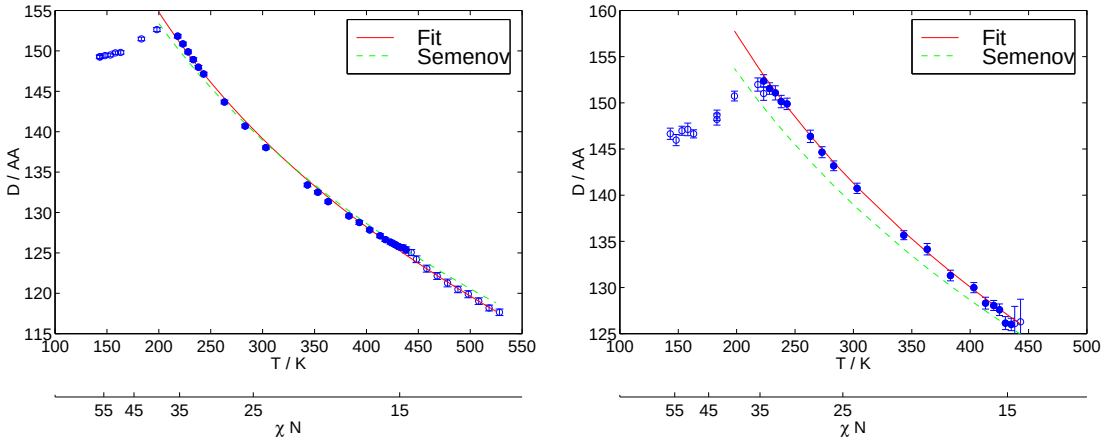

(a) Temperature measurement for the bulk sample.

(b) Temperature measurement for the thin film.

Figure 6.15: SANS temperature measurements.

6.6 AFM Temperature Measurements

A special heatstage for the AFM instrument was designed for the purpose of investigating the topography of the surface at elevated temperatures. Copper was chosen as material to ensure a uniform temperature of the heat stage. Normally the thermal expansion for most experiments can be neglected. However, the AFM is very sensitive to small changes in the the heigth. A qick calculation gives an idea of the size. The linear thermal expansion coefficient for copper is $16.6 \cdot 10^{-6}$ $^{o}C^{-1}$. The expansion for 1 cm copper (thickness of the stage) from room temperature to 100°C is 0.1% which normally would have been neglected. However, the expansion is 12450 nm, which is 30 times more than the thickness of the thickest PEP-PDMS films.

The stage was set at the designated temperature and allowed to equlibrate. When the temperature was stable, the AFM tip was lowered to approx. 2 μm above the surface and allowed to reach an equilibrium temperature. After a finished scan the tip was retracted and a new temperature chosen.

The model polymer system was changed to PS-PB (polystyrene-polybutadiene) with a total molecular weight of 13900 g/mol and an order-disorder transition temperature measured to be 71°C [2]. A new model had to be chosen, since the maximum obtainable temperature in the AFM is approx. 120°C. The low T_{ODT} would allow for investigating the changes near the order-disorder transition. A set of AFM images were measured for three different temperatures: 23°C, 64°C, and 97°C (figure 6.16). As the temperature is increased to 64°C the boundaries between the plateaus straighten and the black line expands to include the tip. When the temperature is increased to 97°C, above the order-disorder transition and the glass transition for PS, the levels unite to form fewer plateaus but does not become homogenous. One problem is the fact that the order-disorder transition occurs below the glass transition. A polymer system with more suitable transition temperature and glass transition temperature would be desirable.

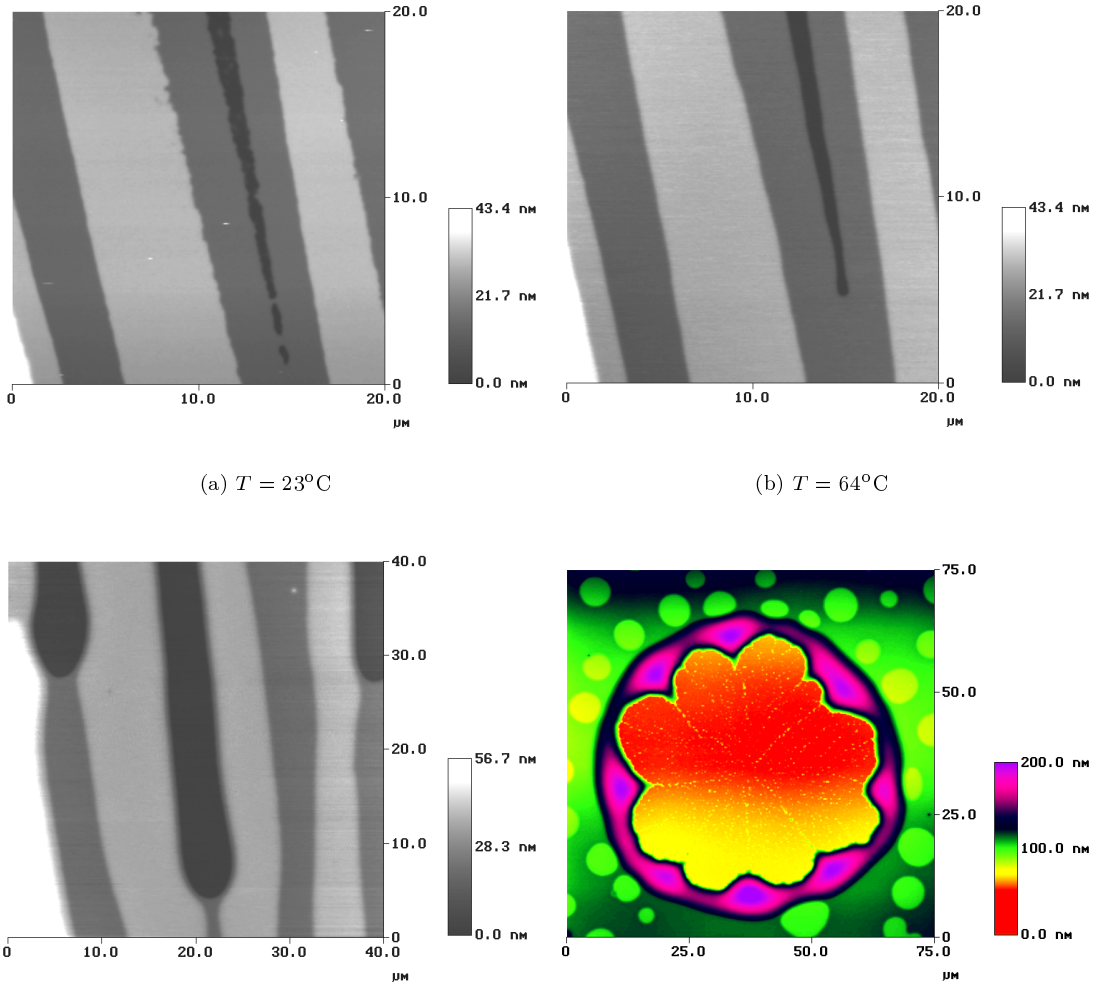

(a) $T = 23^{o}$C

(b) $T = 64^{o}$C

(c) $T = 97^{o}$C

(d) Dewetting after heating the sample.

Figure 6.16: Temperature measurements of PS-PB thin films.

6.7 Dewetting

As the polymers (PEP-PDMS and PS-PB) were heated dewetting occurred. The dewetting did not influence the lamella period measurements. Optical images of PEP-PDMS after heating are shown in figure 6.17. As can be seen from the images the beads of polymer sometimes forms strings. The direction

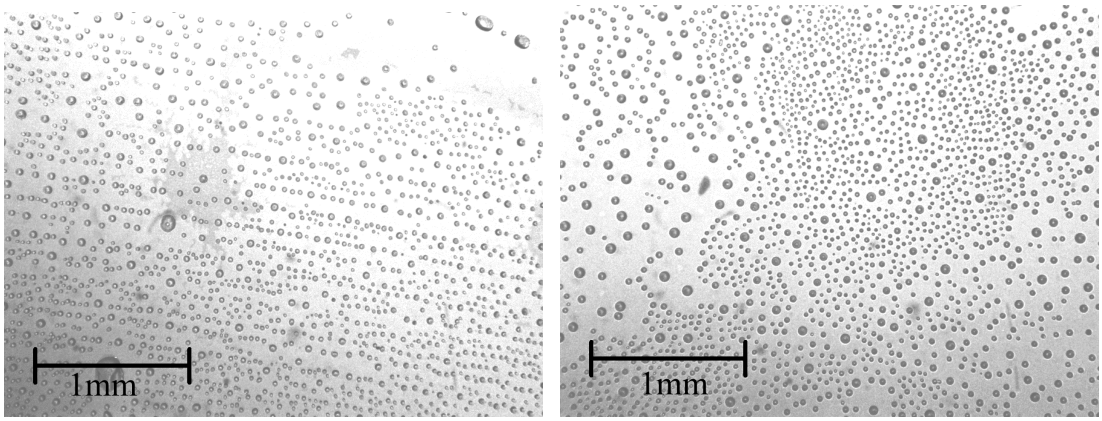

(a) (b)

Figure 6.17: Dewetting of PEP-PDMS after heating under vacuum.

of the strings is the same as the flow during the spin casting. Apparently the spin casting procedure leaves a preferential growth direction in the film.

Dewetting also occurred for the PS-PB polymer. The dewetting is a larger problem in the AFM measurements, because of large topographical changes in the film. The dewetting of PS-PB is shown in figure 6.16(d). As can be seen in the center of the structure the polymer leaves the same trace as was seen in the PEP-PDMS picture.

Chapter 7

Conclusion

7.1 PS-PDMS

It was shown, that the macroscopic curvature of 500 μm thick silicon substrates and the roughness made them suitable for reflectivity measurements.

The difference in x-ray scattering length between the two blocks proved to be insufficient to study the lamellar structure in thin films. The spin casted films could be modeled by just a single layer in the reflectivity model with an averaged scattering density. Even increasing the thickness of the films did not improve the results. However, a combination of an analyzer crystal and a Fourier analysis of the data demonstrated the ability to resolve the thickness of very thick films. The thickness measured by x-ray reflectivity was found to be comparable to the thickness measured by AFM in the thickness measurements.

The SANS measurements of the thin films showed an unexpected arrangement of the microstructure in the films. It is well documented in literature that symmetric block copolymer thin films order along the surface normal of the substrate. However, the SANS scattering images clearly showed a repeat period parallel to the substrate as well. Annealed samples did not change the scattering image, which can be explained by the very high χN-value for the system. The total degree of polymerization of the polymer is $N = 758$, and χ can be calculated from $\chi = \frac{68.4}{T} + 0.036$ [49]. This gives at room temperature a χN-value of 201 and at 200°C 137. Hence it is impossible to anneal the system to a thermodynamical equilibrium structure.

The lamella period in the system was measured for three differently prepared samples. The period differed dramatically from method to method, hence it was difficult to compare the periods measured for the thin film. The solvent cast sample was expected to have a lamellar period close to the thermodynamical equilibrium structure because of the long preparation time and temperature compared to the other methods. The period in the thin film parallel to the substrate is comparable to the period for the solvent cast sample, whereas the period parallel to the surface normal is much smaller and was verified by neutron reflectivity. The microstructure formed during the spin casting is influenced by several competing forces: radial flow of solvent, evaporation, and surface energies. It is difficult to estimate the size of the forces, but the period for the in-plane ordering coincides with the solvent cast sample, which might suggest that the flow induces a preferential direction.

The system is so deep into the ordered state that even surface effects (preferential affinity of one block for the free surface) cannot induce an ordered surface. The surface induced ordering is illustrated in figure 6.11(b), where the lamellae are ordered parallel to the surface but changes orientation deeper in the film. AFM phase images shows that the surface composition changes in areas of equivalent same height.

7.2 PEP-PDMS

The second model system investigated was PEP-PDMS, which in the SAXS and x-ray reflectivity experiments showed suitable x-ray contrast between the blocks but the difference in scattering density between that of the blocks and the substrate made it impossible to analyze the structure of the film in detail. However, deuteration of the PEP-block results in a very high neutron contrast between the blocks.

The neutron reflectivity curves clearly shows the lamellar structure as was expected. It was possible to obtain reflectivity curves spanning over nearly six orders of magnitude. The structure analysis could not be solved by means of neutron reflectivity alone due to an unfortunate scattering density of the PDMS-block. To overcome this problem, XPS was used to determine the surface composition of the film. XPS showed that the top layer was composed of PDMS, as expected, with a thickness of 34 Å, which is approximately half the thickness of the interior layers (75 Å). The lamellar period in the thin film was determined by the position of the Bragg peak. The period of the bilayer was compared to that of a bulk sample by SANS and was found to be 141 Å. This is in perfect agreement with Semenov's scaling prediction. The thin film used in the reflectivity experiments showed a larger thickness than the bulk value. Even the thicker films used in the SANS temperature experiments showed a larger thickness. This can be explained by insufficient material to form another layer, hence the material is distributed over the layers. All experiments showed a larger thickness in the thin films than in the bulk, hence the coils rather tends to be stretched than compressed in the film.

The interphase thickness was found from the reflectivity curves to be 12 Å, which is in perfect agreement with Semenov's prediction of the thickness of the interphase.

It was demonstrated that the reflectivity curve could not be described by just a single reflectivity curve but had to be composed of at least two models. This can be justified by the spotted surface of the film observed in a microscope.

The period of the lamellae was studied at a range of temperatures ($11 < \chi N < 55$), both with reflectivity and SANS, and the scaling behavior compared to theories. The scaling constant was found to be 0.22 for both the thin film and the bulk; also in perfect agreement with scaling theories in the intermediate segregation regime.

Theory [24] predicts that thin films have a higher transition temperature caused by fluctuation effects. Fluctuations tends to stabilize the system. As the thickness of the film increases the transition temperature approaches the value for bulk. The transition temperature can be estimated from the neutron measurements to be 155-160°C, which is lower than what is measured by a rheometer. However, the result from neutron experiments are not very accurate, because the intensity of the Bragg peak is very weak near the order-disorder transition. The predicted increase in T_{ODT} is not observed in these experiments.

It can be concluded that the parameters examined in this thesis for PEP-PDMS as a model system, can be fully explained by the theory for phase segregated block copolymer melts. No difference in the behavior of the thin films was found, except that the confined geometry leads to a stretching of the lamellar period to compensate for excess material in the film.

7.3 Future Experiments

There is still a lot of work to be done on block copolymer thin films. I will outline some possible future experiments to be performed.

Optimize Scattering Density of the Substrate.

PEP-PDMS has sufficient x-ray contrast between the blocks to perform structural measurements on the lamellar structure. However, the difference in scattering density between that of the blocks and the substrate requires a rather thick film in order to be able to see distinct Bragg peaks. Choosing a substrate with a scattering density closer to that of the blocks would be a clever way of solving the problem. It should be kept in mind that not only should the electron density in the material be suitable but the surface must also be smooth and have no macroscopic curvature.

A possible material could be the epoxy resin NOA81 [50]. A simulated reflectivity curve is shown in figure 7.1 for silicon and the epoxy resin as substrate. As can be seen from the figure, the "inverse" Bragg peaks are now much more visible. They are termed "inverse" due to the direction, which is caused be the lower scattering density of the polymer compared to the substrate. Thinner films also make the structural analysis easier. The fabrication method for the substrates are described in detail in [50].

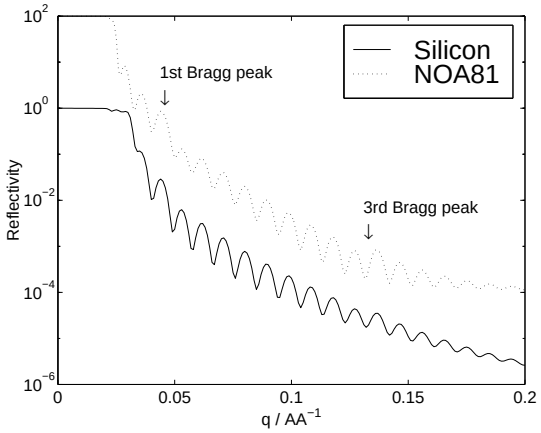

Figure 7.1: Simulated reflectivity curves for PEP-PDMS thin films on silicon and epoxy resin substrates. The curves have been simulated with instrumental resolution and a background level of 10^{-6} has been added.

Material	Scattering density / Å^{-2}	Absorption length / Å^{-1}	Roughness Å
Silicon	1.97e-5	1.44e-6	2.8
NOA81	1.19e-5	3e-7	5.3
Averaged PEP-PDMS	$8.95 \cdot 10^{-6}$	$4.74 \cdot 10^{-8}$	

Table 7.1: Roughness, scattering and absorption lengths compared for NOA81, silicon, and the average values of PEP-PDMS. The values for NOA81 have been taken from Lauridsen [50].

SANS Measurements of PS-PDMS with Lower Molecular Weight.

The SANS images clearly showed structures, which were not in thermodynamical equilibrium. This was caused by the very high χN-value. Reducing the molecular weight could bring the system into a more suitable temperature range. At Risø, such a polymer system is now available with a T_{ODT} =160°C and χN(25°C)$\sim$24. Spin casting the films below the glass transition temperature will cause the films to be "frozen" in a structure as made. Annealing the film in the range from the glass transition temperature to the order-disorder transition temperature and measure the structure by SANS would allow to determine

dynamics in the system. With the knowledge obtained from SANS measurements it should be possible to anneal a sample for a designated time, cool it to room temperature and measure the detailed structure by neutron reflectivity.

Temperature Measurements with AFM

From the AFM temperature measurements it was realized that the dewetting problem was an obstacle to overcome before further measurements could be performed. The requirement for the substrate is that it should be hydrophobic and have a relatively low roughness. The silicon substrate can be used a basis for a modified substrate in the following ways:

- Treatment of the wafers with hydrogenfluride (HF). The HF will react with the hydrophilic SiO_2 surface and leave the silicon surface hydrophobic.

$$SiO_2 + 4HF \rightarrow SiF_4 + 2H_2O$$

- Reacting the surface with a silane containing an alkane or other suitable endgroup.
- Silicon wafer sputtered with a thin gold layer. The gold layer is covered with a thiol with an alkane endgroup.

The HF treatment is not recommended, since HF is a highly reactive acid which must be handled with extreme care. Furthermore, the silicon surface is reactive and will be oxidized with the water vapor in the air within approx. half an hour.

At Risø, silanes with PDMS endgroups are available. The long PDMS endgroups are known [51] to make entanglements with PDMS in a block copolymer. This means that not only will the surface be hydrophobic, but the bottom layer will be "fixed" by the entaglements from the silane. The entanglements will only effect the bottom layer, hence it should still be possible to measure the change in lamellar period as a function of the temperature. Choosing a model system with a relatively low order-disorder transition (below 100°C) would also make it possible to study the morphology change from a phase separated state to a homogeneous state. Such systems are also available at Risø, eg. PI-PDMS which has a T_{ODT} ~100°C.

7.4 Acknowlegdements

I would like to thank my supervisor at Risø, Kell Mortensen, for guiding me through the interesting world of soft materials and especially for giving me the opportunity to participate at the conferences: "*Unifying Principles for Engineering Soft Materials*" held at Risø, and "*Ninth International Conference on Solid Films and Surfaces*" held at Ørsted Laboratory at University of Copenhagen. I would also like thank Jens Als-Nielsen for being my supervisor at University of Copenhagen.

Much of the work could not have been performed without the technical assistance from: Kim Stahl, Thomas Agertoft, Finn Saxild, Bjarne Breiting and Ove Rasmussen. I would especially like to thank Kim Stahl for assistance in the design and machining of the vacuum oven for the neutron reflectivity temperature measurements and the AFM heatstage.

The AFM measurements could not have been performed without Niels B. Larsen's introduction to the instrument and the post analysis of the images. I have also greatly benefitted from clarifying discussion with him. Finally I have also benefitted from valuable discussions with Christine Papadakis, Elisabeth Smela, Henrik Rønnow and Peter Gaarde.

Appendix A

Article Published in Applied Surface Science vol. 142 (1999), 608–613

ELSEVIER

Applied Surface Science 142 (1999) 608–613

applied surface science

The lamellar period in symmetric diblock copolymer thin films studied by neutron reflectivity and AFM

Nikolaj Gadegaard *, Kristoffer Almdal, Niels Bent Larsen, Kell Mortensen

Risø National Laboratory, DK-4000 Roskilde, Denmark

Abstract

The lamellar structure of a symmetric diblock copolymer was studied as a function of temperature. We used *d*PEP-PDMS with a molecular weight of 8.3 kg/mol as model system. The polymer was dissolved in chloroform and spin-casted on silicon wafers into thin uniform films. The degree and direction of lamellar ordering in the thin films was measured by small angle neutron scattering. Neutron reflectivity was used to measure the detailed lamellar structure in the thin films. For the temperature scans only the first order Bragg peak was measured to determine the lamellar period in the film. Our experimental results are compared to theoretical predictions on the scaling behavior of the lamella period as a function of temperature. The morphology of the surface was investigated by atomic force microscopy. Holes were found around defects in the films. The cross-section of the holes revealed the lamellar structure with a periodicity comparable to what was found by neutron reflectivity.

PACS: 61.12.Ex; 61.12.Ha; 68.55.-a

Keywords: Block copolymers; Thin films; Neutron reflectivity; AFM and SANS

1. Introduction

Block copolymers have been studied extensively during the past few decades. The incompatibility of the blocks lead to microscopic phase segregation with a wide range of morphologies. The phase behavior of a mono disperse system can be described by the following parameters: the total degree of polymerisation N, the volume fraction of one of the polymer blocks f_A and the Flory–Huggins interaction parameter $\chi(T)$. We have studied a symmetric block copolymer ($f_A = f_B$), which is known to give lamellar structures [1].

The phase behavior may be used as a surface modification technique. When mixing a homopolymer with a small amount of a block copolymer, the block with the lowest surface energy will segregate to the surface, leaving the surface with a lower surface energy.

We have studied the temperature dependence in lamellar spacing for a confined geometry in a model system of deuterated poly(ethylene-*alt*-propylene-*block*-dimethysiloxane)(*d*PEP-PDMS) with a low molecular weight (8.3 kg/mol) and a low glass transition temperature T_g^{PEP} (−56°C). This combination leads to a highly mobile system at ambient conditions.

* Corresponding author

0169-4332/99/$ - see front matter
PII: S0169-4332(98)00697-7

2. Experimental

2.1. Sample preparation

The polymer was synthesized at Risø National Laboratory with a volume fraction $f_{PEP} = 0.503$ and a total degree of polymerisation $N = 141$. The order–disorder transition temperature was measured to be 165°C by rheology.

For the thin films the polymer was dissolved in chloroform, which is a good solvent for both blocks, in concentrations of 10 and 70 mg/ml. The thin films were spin-casted on Piranha cleaned silicon. The SANS samples were spin-casted on 3×3 cm^2 pieces whereas the samples for neutron reflectivity were spin-casted on wafers 10 cm in diameter. To obtain high quality films, the surface was completely flooded followed by maximum acceleration to a speed of 4000 rpm that was maintained for 30 s.

A bulk sample for small angle neutron scattering (SANS) was made for comparison. The sample was fixed in a sandwich of aluminum foil.

We measured the prepared samples by XPS (X-ray photoelectron spectroscopy) to trace residual solvent, but no chlorine signal was detected. Annealing at elevated temperatures was not necessary as the polymer is in a highly mobile state at room temperature (low glass transition temperature). A SPECS Sage 100 was used for the XPS measurements operating with a Mg X-ray source at 100 W.

2.2. Neutron scattering

The neutron experiments were performed at the cold source from DR3 at Risø National Laboratory. The wavelengths for the SANS and reflectivity experiments were chosen to be 5.4 Å and 4.75 Å, respectively.

We used SANS to measure the lamellar spacing in bulk and the degree of ordering in the thin films. The thin film samples were aligned with the surface parallel to the incident neutron beam.

For the neutron reflectivity (NR) experiments, the large sample was mounted in a specially designed vacuum oven to prevent oxidation of the polymer at elevated temperatures. The sample was brought into the disordered state ($T = 175$°C) and then quenched to $T = -100$°C within 5 min. The first order Bragg peak at $(4\pi/\lambda)\sin\theta = q \sim 0.045^{-1}$ was measured at various temperatures up to T_{ODT}.

Due to the very time consuming nature of neutron reflectivity, full scans ($q = 0.01$–0.15 Å^{-1}) were only measured at room temperature and above T_{ODT}.

2.3. Atomic force microscopy

The surface morphology was measured using a Digital Instrument Dimension 3000 operating in tapping mode. Since PDMS is especially soft, tapping mode was chosen to prevent undesired perturbation or directly damaging the surface.

3. Results and discussion

For the bulk sample, the peak position in the SANS experiment was found at $q_{100} = 0.045$ Å^{-1} corresponding to a lamella period of 139 Å.

The thin films, for the SANS experiments, were aligned with the surface parallel to the incident beam. As can be seen in Fig. 1 the lamellae are perfectly aligned parallel to the substrate.

Fig. 2 shows the resulting neutron reflectivity curve at room temperature. The reflectivity curve above T_{ODT} only shows the smooth Fresnel curve from an isotropic polymer film.

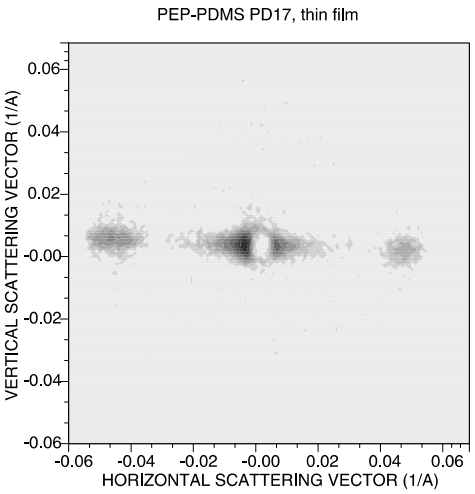

Fig. 1. SANS contour plot of the thin film, showing perfect ordering out of plane. The film was mounted vertically.

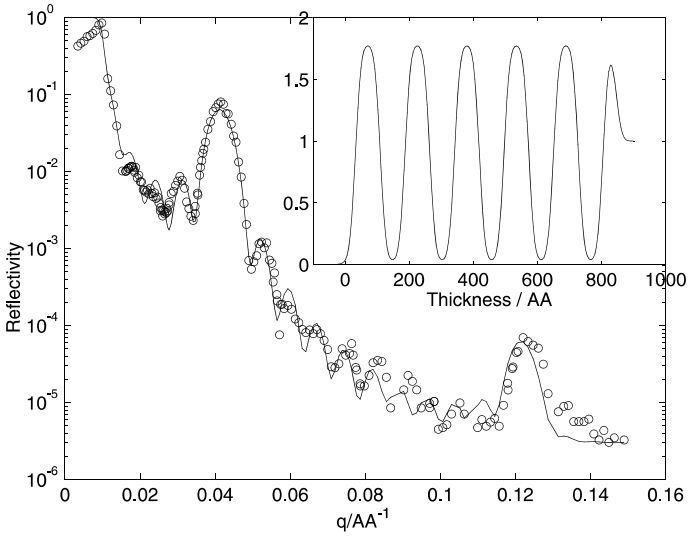

Fig. 2. Neutron reflectivity curve with the corresponding profile measured at room temperature. The scattering length in the profile is normalized to that of the substrate.

The reflectivity curve was fitted using the modified Parratt [2] formalism where the interfacial width is described by an error function. Correction for experimental resolution [3] was included in the fitting. Since PDMS has a neutron scattering length close to zero, it is difficult to determine if the top layer is PDMS or PEP by NR. The top layer is defined as the free interface. From the XPS measurement it was possible to determine the surface composition and thickness. PDMS is expected to be the top layer due to the lowest surface energy of the two blocks. The element composition would be (C:Si:O) 50%:25%:25%, where we measured 63%:18%:19%. The signal, however, decays exponentially in hydrocarbons with a characteristic length of 25 Å [4]. Combining this characteristic decay length with the measured element composition, we can conclude that the thickness of the outermost PDMS layer was calculated to be 34 Å $\pm$ 3 Å, in agreement with the expected thickness for half a layer.

In the profile reconstruction of the reflectivity curve, the information from XPS was used as a starting guess for the top layer. The thickness of the thin film is reflected in the width of the first order Bragg peak. This information was used as a starting guess for estimating the number of layers during fitting. The fitted curve with the corresponding scattering length profile is shown in Fig. 2.

It should be noted that both the top and bottom layers have approximately half the thickness of the interior layers. This can be explained by the void space left at the top and bottom interfaces. To compensate for this, the polymers collapse into Gaussian coils. The composition of the free and substrate interfaces is determined by the gain in interfacial energy. It is energetically more favorable to cover the substrate with PEP, which has a higher surface energy than PDMS, whereas PDMS is more favorable at the free surface. The length of the interior layers was found to be 77 Å $\pm$ 4 Å leading to a complete period of 154 Å $\pm$ 8 Å. This value is slightly higher than for the bulk structure, which means that the confined geometry gives rise to a slightly more stretched structure than in bulk. The interfacial width was found to be 14 Å $\pm$ 1 Å.

In each temperature measurement a Gaussian was fitted to the first order Bragg peak and the layer spacing, corresponding to the fitted peak position,

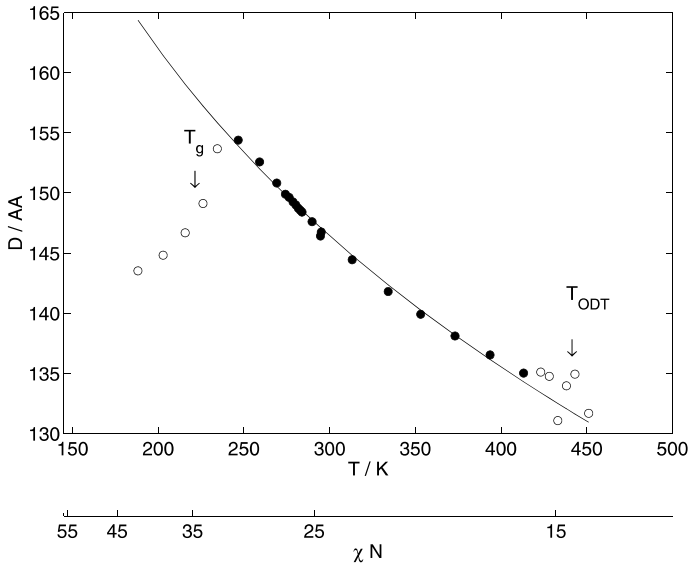

Fig. 3. First order Bragg peak position from NR plotted as a function of temperature. The scaling parameter was fitted in the range $T_g^{PEP} < T < T_{ODT}$ (closed symbols).

plotted as a function of temperature (see Fig. 3). The change in sign for the slope at ~ 250 K, above T_g, is most likely to be a melting of PDMS [5], rather than the glass transition for PEP.

Leibler [6] used a mean field approach to describe the phase behavior near the order–disorder transition (ODT). This region is often termed the weak segregation regime (WSR), due to the interface profile, which is nearly sinusoidal. He predicted the transition to occur at $\chi N = 10.5$, where the Flory–Huggins interaction parameter χ can be written as is the sum of the enthalpic and entropic energies

$$\chi = \frac{A}{T} + B \qquad (1)$$

with $A = 63.3$ K and $B = -4 \cdot 10^{-2}$. [1]

Helfand and Wasserman [7] used a narrow interface approximation to describe the strong segregation regime (SSR), $\chi N > 30$, where the profile is nearly step-like. Semenov [8] derived an analytical

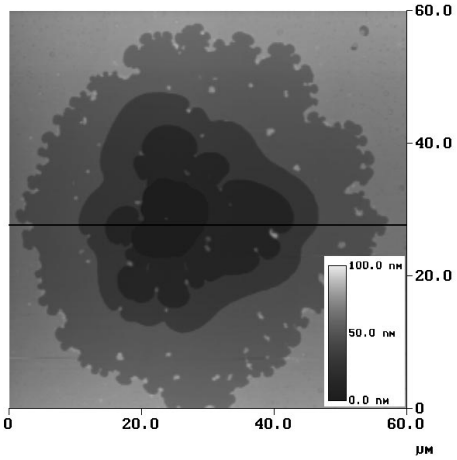

Fig. 4. AFM micrograph of the surface. The line indicates the cross-section seen in the figure below.

[1] The values were found from SANS experiments on a set of polymers with different degree of polymerisation. Unpublished.

expression for the scaling behavior of the repeat distance D in a lamellar structure. His scaling prediction in the strong segregation regime is given as

$$D \propto \chi^{1/6} \sim \chi^{0.17} \quad (2)$$

Melenkevitz and Muthukumar [9] used density functional theory and identified a change in the scaling parameter for two different regimes: $D \propto \chi^{0.22}$ for χN in the range from 15 to 95 while $D \propto \chi^{0.17}$ for $\chi N > 95$. In the SSR Melenkevitz and Muthukumar's expression reduces to Semenov's.

The measured data are shown in Fig. 3, where the data above the crystallisation temperature and below T_{ODT} has been fitted to the scaling expression $D \propto \chi^{p}$. The exponent is found to be $p = 0.21 \pm 0.01$ which is in very good agreement with Melenkevitz and Muthukumar's scaling exponent in the intermediate regime ($15 < \chi < 95$). The interfacial width found in the reflectivity analysis corresponds to an almost sinusoidal interface, which confirms this result.

The surface morphology was measured by AFM. Defects in the film, probably from the preparation process, induced holes in the film (see Fig. 4). A cross-section (Fig. 5) clearly shows the stratified structure. The periodicity (145 Å ± 10 Å) is fully comparable to what is measured by NR (154 Å ± 5 Å). As can be seen from the cross-section, the outermost layer does not show half the thickness as was measured by XPS. This can be explained by the fact, that the AFM always measures on exposed surfaces. On every plateau in the hole, the surfaces will be collapsed, hence only full periods will be measured. It should be noted that the defect did not penetrate to the substrate. Consequently the expected half layer at the bottom of the film was not observed.

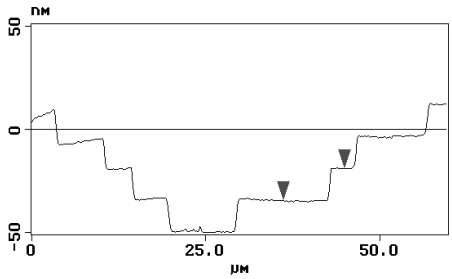

Fig. 5. Cross-section of a hole in the thin film. It clearly shows the stratified structure of the thin film.

4. Conclusions

The highly mobile system, we have investigated, has shown the induced order from the confined geometry of the system. We have shown that the top layer has half the length of the layers in the interior structure using the powerful combination of XPS and NR. Segregation to the surfaces is driven by two effects [10]. A large difference in surface energy between the two blocks will drive the low surface energy component to the surface. This is the fact for both the free and solid surface. If the blocks have similar surface energies the most flexible block will tend to segregate to the surface. PDMS has a low surface energy and is the most flexible of the two blocks (the molecular weight averaged end-to-end distance ($\langle R_0^2 \rangle / M$) is 0.924 Å^2 mol g^{-1} and 0.422 Å^2 mol g^{-1} for PEP and PDMS, respectively, at room temperature [11]).

The scaling behavior of the lamella period predicted theoretically by Semenov and Melenkevitz and Muthukumar has been confirmed for the confined geometry. The exponent was found to be in excellent agreement with the theoretical prediction in the intermediate regime.

AFM has shown to be a valuable tool in the analysis of lamellar systems where it is possible to probe the sample surface structure on a local (microscopic) scale and use small samples, whereas neutron reflectivity requires large samples and measures large areas (macroscopic), but provide information on the interior film structure.

Acknowledgements

We would like to acknowledge the technical staff at Risø for invaluable help. We would also like to acknowledge Christine Papadakis for stimulating discussions.

References

[1] F.S. Bates, Science 251 (1991) 898.
[2] L.G. Parratt, Phys. Rev. 95 (1954) 359.
[3] J.S. Pedersen, I.W. Hamley, J. Appl. Cryst. 27 (1994) 36.
[4] Handbook of X-ray Photoelectron Spectroscopy, Perkin–Elmer, 1992.
[5] M.I. Aranguren, Polymer 39 (1998) 4897.
[6] L. Leibler, Macromolecules 13 (1980) 1602.
[7] E. Helfand, Z.R. Wasserman, Macromolecules 9 (1976) 879.
[8] A.N. Semenov, Sov. Phys. JETP 61 (1985) 733.
[9] J. Melenkevitz, M. Muthukumar, Macromolecules 24 (1991) 4199.
[10] M. Sikka, N. Singh, A. Karim, F.S. Bates, S.K. Satija, C.F. Majkrzak, Phys. Rev. Lett. 70 (1993) 307.
[11] L.J. Fetters, D.J. Lohse, D. Richter, T.A. Witten, A. Zirkel, Macromolecules 27 (1994) 4639.

Appendix B

The Darwin width

The Darwin width is given by [27]

$$D = 2.12\frac{r_e N\lambda^2|F|}{\pi\sin(2\theta)}\frac{1+|\cos(2\theta)|}{2} \tag{B.1}$$

where r_e is the Thompson scattering length, N is the number of atoms per volume, F is the structure factor and θ is the scattering angle.

The wavelength of the incident beam is $\lambda = 1.5406$Å. The crystal structure of germanium is face centered cubic with unitlength $a = 5.65745$ Å. The scattering vector $q_{111} = \sqrt{3}\frac{2\pi}{a} = 1.92362$ Å^{-1} which equals a scattering angle $\theta_{111} = 13.6406^{\circ}$. The structure factor for germanium is shown in figure B ($F_{\mathrm{Ge}(111)} = \frac{1}{\sqrt{2}}f_{\mathrm{Ge}} = 19.544$). The density is $\rho = 5.323$ g/cm^3 and the atomic weight is $m = 72.59$

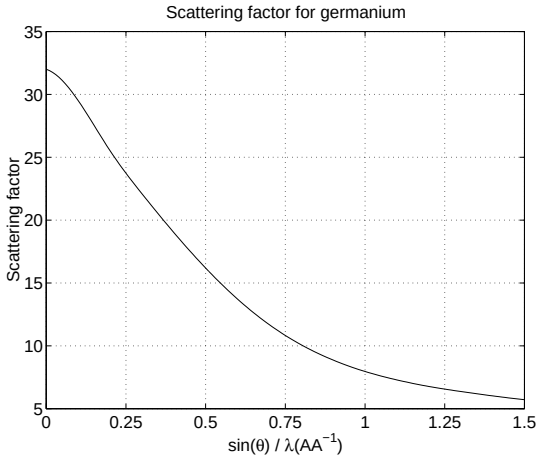

Figure B.1: Scattering factor for germanium.

g/mol giving $N = N_A\rho/m = 0.0441$ number of atoms per Å^3. Inserting the constants in equation B.1 gives a Darwin width of 4.6 mdeg or $8.03{\cdot}10^{-5}$ rad.

Appendix C

Constants

C.1 Neutrons

The scattering density for neutrons is

$$N_A \frac{b_{mon}}{M_{mon}} \rho_{mon}$$

where b_{mon} is the sum of the neutron scattering lengths of the elements in a monomeric unit.

Elements

Element	Neutron scatt. len. [Å]	Atomic weight [g/mol]	Atomic number	Density [g/cm^3]	Scatt. dens.
^{1}H	-3.71·10^{-5}	1.0078	1		
^{2}H	6.67·10^{-5}	2.0141	1		
C	6.65·10^{-5}	12.011	6	2.25	7.50·10^{-6}
O	5.80·10^{-5}	15.999	8		
Si	4.15·10^{-5}	28.086	14	2.33	2.07·10^{-6}

Polymers

Polymer	Neutron scatt. len. [Å]	Molecular weight [g/mol]	Density at 25°C[g/cm^3]	Scatt. density
PEP (H/D)	4.81·10^{-4}	75.16	0.856	3.30·10^{-6}
PDMS	1.01·10^{-5}	74.15	0.970	7.94·10^{-8}
PS	2.35·10^{-4}	104.15	1.030	1.40·10^{-6}

C.2 X-rays

The scattering density for x-rays is

$$r_0 \rho_{el}$$

where $r_0 = 2.82$ fm is the Thomson length and ρ_{el} is the electron density in the material.

Elements

Element	Scatt. dens.	Absorption length [Å^{-1}]
C	1.05·10^{-7}	1.2 ·10^{-7}
Si	1.97·10^{-6}	1.44·10^{-6}

Polymers

Element	X-ray scatt. len. [Å]	Scatt. dens.	Absorption length [$Å^{-1}$]
PEP (H/D)	$4.81 \cdot 10^{-4}$	$7.74 \cdot 10^{-6}$	$2.39 \cdot 10^{-8}$
PDMS	$1.01 \cdot 10^{-5}$	$8.89 \cdot 10^{-6}$	$7.08 \cdot 10^{-8}$
PS	$2.35 \cdot 10^{-4}$	$9.41 \cdot 10^{-6}$	$2.71 \cdot 10^{-8}$

References: [1, 28, 40].

C.3 Temperature Dependent Constants for PEP-PDMS

Segment Length

$$a_{\mathrm{PEP}}(T) = 8.2 \cdot 10^{-10}\mathrm{m} \exp(-4.458 \cdot 10^{-4}\ T)$$

$$a_{\mathrm{PDMS}}(T) = 4.7 \cdot 10^{-10}\mathrm{m} \exp(3.462 \cdot 10^{-4}\ T)$$

Density

$$\rho_{\mathrm{PEP}}(T) = 1.054\mathrm{g/cm}^3 \exp(-6.977 \cdot 10^{-4}\ T)$$

$$\rho_{\mathrm{PDMS}}(T) = 1.195\mathrm{g/cm}^3 \exp(-6.998 \cdot 10^{-4}\ T)$$

Standard Segment Volume

$$v_0(T) = 88 \cdot 10^{-30}\mathrm{m}^3 \exp(7 \cdot 10^{-4}\ T)$$

The expressions are adapted from [1].

C.4 Glass Transition Temperature

Polymer	PDMS	PEP	PS
T_g/°C	-127	-56	96

References: [1, 12].

C.5 Surface Tensions

Polymer	Surface tension γ [mN/m]	
	at 25°C	at 150°C
PDMS	20	14
PEP	39	31
PS	34	26

References: [12].

C.6 Hildebrand Parameters

Polymer	δ $[(\mathrm{MPa})^{1/2}]$	Solvent	δ $[(\mathrm{MPa})^{1/2}]$
PEP	15.8	Cyclohexane	16.8
PDMS	14.9-15.6	Chloroform	19.0
PS	17.4-21.1	Toluene	18.2
		Water	47.9

References: [12, 13].

C.7 Empirical Flory-Huggins Parameters

$$\chi(T) = \frac{A}{T} + B$$

Polymer	A [K]	B
PEP-PDMS	63.3	-0.04
PS-PDMS	68.4	0.036

References: [49].

Bibliography

[1] Martin E. Vigild. *Mesomorphic Phase Behavior of Low Molar Mass PEP-PDMS Diblock Copolymers Synthezised by Anionic Polymerization.* PhD thesis, University of Copenhagen, October 1997.

[2] Christine M. Papadakis. *Structure and Dynamics of Symmetric Diblock Copolymers.* PhD thesis, Roskilde Universitetscenter, 1996.

[3] D. Schwahn, H. Frielinghaus, K. Mortensen, and K. Almdal. Temperature and pressure dependence of the order parameter fluctuations, conformational compressibility, and the phase diagram of the pep-pdms diblock copolymer. *Phys. Rev. Lett.*, 77(15):3153–5156, 1996.

[4] M. Szwarc, M. Levy, and R. Milkovich. Polymerization initiated by electron transfer to monomer. a new method of formation of block copolymers. *J. Am. Chem. Soc.*, 78:2656–2657, 1956.

[5] Owen W. Webster. Living polymerization methods. *Science*, 251:887–893, 1991.

[6] K. Binder. Phase transitions in polymer blends and block copolymer melts: Some recent developments. *Adv. in Pol. Sci.*, 112:181–299, 1994.

[7] Frank S. Bates. Polymer-polymer phase behavior. *Science*, 251:898–905, 1991.

[8] Frank S. Bates and Glenn H. Fredrickson. Block copolymer thermodynamics: Theory and experiment. *Annu. Rev. Chem.*, 41:525–888, 1990.

[9] Inc. Encyclopædia Britannica. *Britanica Online.* 1998.

[10] Christine Flarup. Strukturel og kemisk karakterisering af ordnede molekylære overfladelag. Master's thesis, Danmarks Tekniske Universitet, November 1996.

[11] Petr Munk. *Introduction to Macromolecular Science.* John Wiley & Sons, 1989.

[12] J. Brandrup and E. H. Immergut. *Polymer Handbook.* John Wiley & Sons, 3rd edition edition, 1989.

[13] Kristoffer Almdal, Kell Mortensen, Anthony J. Ryan, and Frank S. Bates. Order, disorder, and composition fluctuation effects in low molar mass hydrocarbon-poly(dimethylsiloxane) diblock copolymers. *Macromolecules*, 29(18):5940–5947, 1996.

[14] Mohan Sikka, Navjot Singh, Alamgir Karim, Frank S. Bates, Sushil K. Satija, and Charles F. Majkrzak. Entropy-driven surface segregation in block copolymer melts. *Phys. Rev. Lett.*, 70(3): 307–310, 1993.

[15] Ludwik Leibler. Theory of microphase separation in block copolymers. *Macromolecules*, 13(6): 1602–1617, 1980.

[16] Glenn H. Fredrickson and Eugene Helfand. Fluctuation effects in the theory of microphase separation in block copolymers. *J. Chem. Phys.*, 87(1):697–705, 1987.

[17] Frank S. Bates, Jeffrey H. Rosedale, Glenn H. Fredrickson, and Charles J. Glinka. Fluctuation-induced first-order transition of an isotropic system to a periodic state. *Phys. Rev. Lett.*, 61(19): 2229–2232, 1988.

[18] Frank S. bates, Jeffrey H. Rosedale, and Glenn H. Fredrickson. Fluctuation effects in a symmetric diblock copolymer near the order-disorder transition. *J. Chem. Phys.*, 92(10):6255–6270, 1990.

[19] Eugene Helfand and Z. R. Wasserman. Block copolymer theory. 4. narrow interphase approximation. *Macromolecules*, 9(6):879–888, 1976.

[20] A. N. Semenov. Contribution to the theory of microphase layering in block-copolymer melts. *Sov. phys. JETP*, 61(4):733–742, 1985.

[21] L. J. Fetters, D. J. Lohse, D. Richter, T. A. Witten, and A. Zirkel. Connection between polymer molecular weight, density, chain dimensions, and melt viscoelastic properties. *Macromolecules*, 27 (17):4639–4647, 1994.

[22] Mark D. Foster, Mohan Sikka, Navjot Singh, Frank Bates, Sushil K. Satija, and Charled Majkrzak. Structure of symmetric polyolefin block copolymer thin films. *J. Chem. Phys.*, 96:8605–8615, 1992.

[23] J. Melenkevitz and M. Muthukumar. Density functional theory of lamellar ordering in diblock copolymers. *Macromolecules*, 24(14):4199–4205, 1991.

[24] Kenneth R. Shull. Mean-field theory of block copolymers: Bulk melts, surfaces and thin films. *Macromolecules*, 25(8):2122–2133, 1992.

[25] G. E. Bacon. *Neutron Diffraction*. Oxford University Press, 3rd edition edition, 1975.

[26] Jens Als-Nielsen. Lecture notes for experimental x-ray physics, 1997.

[27] B. E. Warren. *X-Ray Diffraction*. Dover, 1st edition edition, 1990.

[28] Varley F. Sears. Neuton scattering lengths and cross sections. *Neutron News*, 3(3):26–37, 1992.

[29] Nikolaj Gadegaard. Experimental manual for tas8. User notes, February 1998.

[30] Peter Høghøj, Nikolaj Gadegaard, Henrik Rønnow, and Kurt N. Clausen. Polarized neutron reflectivity of magnetic super mirrors. Unpublished, January 1998.

[31] J. Baruchel, J. L. Hodeau, M. S. Lehmann, J. R. Regnard, and C. Schlenker, editors. *Neutron and Synchrotron Radiation from Condensed Matter Studies*. Springer-Verlag, 1993.

[32] T. P: Russell. X-ray and neutron reflectivity for investigation of polymers. *Mat. Sci. Rep.*, 5: 171–271, 1990.

[33] L. G. Parratt. Surface studies of solids by total reflection of x-rays. *Phys. Rev.*, 95(2):359–369, 1954.

[34] Ian W. Hamley and Jan Skov Pedersen. Analysis of neutron and x-ray reflectivity data. i. theory. *J. Appl. Cryst*, 27:29–35, 1994.

[35] John Lekner. *Theory of Reflection*. Martinus Nijhoff, 1987.

[36] J. Als-Nielsen and K. Kjaer. *Phase Transitions in Soft Condensed Matter*, pages 113–138, 1989.

[37] Wim G. Bouwman and Jan Skov Pedersen. Resolution function for two-axis specular neutron reflectivity. *J. Appl. Cryst.*, 29:152–158, 1996.

[38] R. A. Cowley. Resolution function of an x-ray tripple-crystal diffractometer. *Acta. Cryst.*, A(43): 825–836, 1987.

[39] A. Weill and E. Dechenaux. The spin-coating process mechanism related to polymer solution properties. *Polym. Eng. and Sci.*, 28(15):945–948, 1988.

[40] Robert C. Weast. *Handbook of Chemistry and Physics*. CRC, 74 edition edition, 1993.

[41] A. Gibaud and G. Vignaud. The correction of geometrical factors in the analysis of x-ray reflectivity. *Acta. Cryst.*, A(49):642–648, 1993.

[42] Xiao-Lin Zhou and Sow-Hsin Chen. Theoretical foundation of x-ray and neutron reflectometry. *Physics Reports*, 257:223–348, 1995.

[43] Jan Skov Pedersen and Ian W. Hamley. Analysis of neutron and x-ray reflectivity data. ii. constrained least-squares methods. *J. Appl. Cryst*, 27:36–49, 1994.

[44] Xin Chen, Jr. Joseph A. Gardella, and Philip L. Kumler. Fourier transform infrared and electron spectroscopy for chemical analysis studies of block copolymers of styrene and dimethylsiloxane. *Macromolecules*, 25(24):6621–6630, 1992.

[45] *Handbook of X-ray Photoelectron Spectroscopy*. Perkin Elmer Corporation, 1992.

[46] J. Coutandin, D. Elich, H. Sillescu, and Chin-Hsien Wang. Morphology of block polymers near a free surface. *Macromolecules*, 18:589–590, 1985.

[47] Spiros H. Anastasiadis, Thomas Russel, Sushil K. Satija, and Charled Majkrzak. The morphology of symmetric diblock copolymers as revealed by neutron reflectivity. *J. Chem. Phys*, 92:5677–5691, 1990.

[48] Mirta I. Aranguren. Crystallization of polydimethylsiloxane. *Polymer*, 39:4897–4903, 1998.

[49] Kristoffer Almdal. Personal communication, 1998.

[50] Erik Lauridsen. X-ray scattering of modified silicon and polymer surfaces. Master's thesis, Københavns Universitet, Juli 1998.

[51] Niels Berg Madsen. Personal communication, 1998.

Bibliographic Data Sheet **Risø–R–1087(EN)**

Title and author(s)

Structural Study of Symmetric Diblock Copolymer Thin Films

Nikolaj Gadegaard

ISBN	ISSN
87–550–2478–5; 87–550–2479–3 (internet)	0106–2840

Dept. or group	Date
Condensed Matter Physics and Chemistry Department	August 2000

Groups own reg. number(s)	Project/contract No.

Pages	Tables	Illustrations	References
85	21	58	51

Abstract (Max. 2000 char.)

Thin diblock copolymer film have been investigated by x-ray and neutron reflectivity as well as small angle x-ray and neutron scattering. Two model systems have been investigated. PS-PDMS (25 kg/mol-25 kg/mol), which has a glass transition temperature of ca. 100°Cfor the PS-block. This means that the structure can be frozen below that temperature, thus the development of the lamella structure may be follow by reflectivity. It was, however, not possible to reach the expected equilibrium structure. Hence the second model system, deuterateted PEP-PDMS (4.4 kg/mol-4.4 kg/mol) was chosen for its low glass transition temperature -56°C. This means that the system spontaneously should form lammela ordered structures at room temperature. This ordering was studied by neutron reflectivity and small angle neutron scattering in the temperature range from -140°C(below PDMS' glass transition temperature, -127°C) and up to 250°C(above the order-disorder temperature, 165°C). Results were found to be in perfect agreement with theory. Surface morphology as function of temperature was also measured, and holes in the surface resembled the periodicity measured by reflectivity.

Descriptors INIS/EDB

DIBLOCK COPOLYMER; REFLECTIVITY; X-RAY; NEUTRON; THIN FILM; ATOMIC FORCE MICROSCOPY

Available on request from:
Information Service Department, Risø National Laboratory
(Afdelingen for Informationsservice, Forskningscenter Risø)
P.O. Box 49, DK–4000 Roskilde, Denmark
Phone (+45) 46 77 46 77, ext. 4004/4005 · Fax (+45) 46 77 40 13
E-mail: infserv@risoe.dk